UNIVERSITÀ DEGLI STUDI DI MILANO &
UNIVERSITÀ CATTOLICA DEL SACRO CUORE

DIPARTIMENTO DI MATEMATICA E FISICA

CORSO DI DOTTORATO DI RICERCA IN
FISICA, ASTROFISICA E FISICA APPLICATA

Ciclo XXVIII

Tracking the Interface States dynamics at Carbon-based nanostructures on Metal by Non-linear Photoemission Spectroscopy

Settore scientifico disciplinare FIS/03

Tesi di Dottorato di:
Silvia Tognolini

Coordinatore: Prof. Marco Bersanelli
Tutore: Dott.ssa Stefania Pagliara

Anno Accademico 2014-2015

Study hard what interest you the most,
in the most undisciplined, irreverent
and original manner possible.
Richard Feynman

Contents

Chapter 1

Introduction

In recent years the surface physics has shown a growing interest in the study of two-dimensional (2D) materials. Although these materials have historically been one of the most extensively studied classes, it is only recently that the great potentialities of these systems in advanced technological applications have been understood [1]. Each layered material, indeed, when reduced to atomically thin, exhibits unique electronic properties, different from its bulk counterpart [2].
Currently, 2D materials represent a promising class due to the large variety of possible applications, ranging from electronics to gas storage, catalysis, high performance sensors, support membranes and inert coatings.
A significant increase in exploring 2D materials occurred in 2004 (see Figure 1.1), when a group of researchers from Manchester University, lead by A. Geim, discovered a simple method, based on micro-mechanical exfoliation by adhesive tape of graphite, for isolating a single atomic layer of graphite, known as graphene [3–5]. Thenceforth research communities have concentrated their efforts in the investigation of this novel material and, afterwards, of 2D materials, extending their interests to a very wide variety of single-atom thin materials, such as nitrides (e.g. h-BN), dichalcogenides (e.g. MoS_2), topological insulators (e.g. Bi_2Se_3 or Bi_2Te_3) and even oxides [2].

Graphene, in addition to its characteristic two-dimensionality, exhibits a very interesting electronic structure. The π and π^* bands touch each other at the Fermi energy (E_F) at the $\overline{K}$ points of graphene Brillouine zone and, close to these so-called Dirac points, the bands display a linear dispersion, generating the Dirac Cones [6]. This topology of the bands gives rise to exotic electronic transport properties, i.e. the charge carriers behave like relativistic massless particles, leading to various quantum Hall effects, ultra high carrier

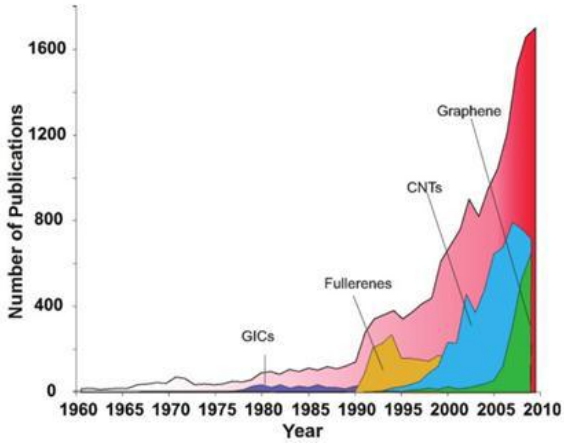

Figure 1.1: Number of publications per year (vertical axis) against the calendar year (horizontal axis). Red for carbon and its derivatives, green for graphene, light blue for carbon nanotubes, yellow for fullerenes, purple for graphite. Taken from https://scientificentrepreneur.wordpress.com/2011/04/18/what-is-graphene/.

mobility, and many other novel phenomena [6, 7]. Moreover, the stability under ambient conditions, an exceptional thermal conductivity (also greater than diamond) and amazing mechanical properties (a Young's modulus of 1 TPa and intrinsic strength of 130 GPa [8]) make graphene very attractive for numerous applications [9].

Another class of carbon-based materials extensively studied in recent decades is represented by organic-molecules, such as porphyrins or phthalocyanine. The huge variety of important biological processes in which these molecules are involved together with the outstanding chemical-physical properties, make organic-molecules of paramount interest in many chemical and physical research fields. Carbon-based molecules, indeed, represent a very promising material due to their enormous potential applications such as opto-electronic devices, solar cells, chemical and gas sensors or catalytic materials.

Despite of their potentiality, the introduction of 2D carbon-based devices in industrial applications is still beyond reach. The challenges in the realization of such electronic devices are the control of the interaction with metal contacts

and the fabrication of large carbon-based nanostrucures film with controlled properties. Nonetheless, achieving these goals is nowadays mandatory for significant progresses in the realization of advanced devices based on low-dimensional carbon nanostructures.

An excellent opportunity to probe the interaction between carbon nanostructures and the metal substrate is represented by a systematic study of the properties and the dynamics of the the Interface States. The unoccupied Image Potential States (IPS), in particular, due to their localization in a two dimensional region parallel to the surface and due to the large spatial extension of their wave functions into the vacuum are extremely sensitive to any modification at the surface [10]. Moreover, the presence of adsorbates on metal substrate can significantly alter the electronic properties and dynamics of such electronic states.

The application of femtosecond, high intensity laser pulses in the near-UV ranges to the photoemission techniques has opened the way for non-linear photoemission studies, in which multi-photons transitions induced by the high-intensity coherent pulses are possible. Non-linear photoemission spectroscopy, hence, represents an ideal tool to investigate the properties of the occupied and unoccupied electronic states at the interface and to unravel their electronic relaxation dynamics in the time domain, by means of time-resolved experiments.

1.1 Outlines of the thesis

In the present thesis, the electronic properties and dynamics of the excited states which live at the carbon nanostructures/metal interfacial region have been studied by means of Angle-Resolved and Time-Resolved two-photon photoemission spectroscopy (2PPE).
Most of the work here reported has been devoted to the investigation of the surface states at the graphene/metal interface, distinguishing by the nature of the metal substrate between weakly and strongly interacting systems. Furthermore, the dynamics of the unoccupied excited states at organic-molecules/metal systems have been studied by Time-Resolved 2PPE.
In order to have a complete understanding of the electronic interface states at carbon-based nanostructures on metal, the experimental results are often supported by theoretical calculation performed in collaboration with the group of

Dipartimento di Chimica, Università degli Studi di Milano and CNR-ISTM, led by M. I. Trioni.

The outline of the thesis is the following:

- In Chapter 2 the theoretical predictions, the general behavior and the properties of the electronic surface states on metal surfaces are presented in detail. Furthermore, a brief review of the available experimental techniques used for the surface states investigation, with particular attention to the 2PPE spectroscopy, is provided.

- In Chapter 3 recent results regarding the electronic properties and dynamics of the excited states which live at the carbon-based nanostructures/metal interfaces are reviewed, with particular attention to graphene/ metal and organic-molecules/metal systems.

- In Chapter 4 we focus on the surface states at the weakly coupled single-layer graphene/Cu(111) interface. In addition to the ultraviolet non-linear angle-resolved photoemission spectroscopy studies, 2PPE measurements by tuning the laser photon energy are reported. The experimental results achieved are completed by theoretical *ab-initio* calculations.

- In Chapter 5 the surface states at single-layer graphene/Ir(111) interface are investigated. A detailed ultraviolet 2PPE study of the electronic properties and dynamics of the $n = 1$ IPS is reported. In particular, by using circularly polarized femtosecond laser pulses, experimental evidence of a Rashba-type spin splitting in the $n = 1$ IPS is observed. Moreover, information about the depopulation time of the first image potential state has been investigated by tuning the incident photon energy and by pump-probe experiments.

- In Chapter 6 the interface states at the strongly interacting graphene/ Ni(111) system are studied. By combining non-linear photoemission experiments and density functional theory calculations we investigate the interface states with particular attention to the possibility of spin-polarized electron injection into $n = 1$ IPS.

- In Chapter 7 the relaxation processes of the first two excited molecular states at the interface between meso-tetraphenylporphyrin (TPP) and two different orientations of the silver surface, Ag(100) and Ag(111), are tracked by time-resolved non-linear photoemission measurements. Moreover possible charge transfer channels between silver substrate and molecules overlayer have been investigated.
- In Chapter 8 the conclusions are reported and the future perspectives are planned.

Chapter 2

Electronic Surface States

The presence of a surface, breaking the solid translational symmetry along one of the three dimensions of space allows the rising of some electronic states lacking in a bulk metal: the surface states. These states are spatially confined to the surface region and their associated wave function decays exponentially inside of the crystal and towards the vacuum.
At a metal surface, two kinds of electronic states can be found: the intrinsic surface states and the image potential states (IPS). They differ in their charge density localization relative to the surface: the intrinsic surface states are localized mainly at the surface atomic layer, while the image potential states, generated by a potential well, formed by the Coulomb-like attractive image potential and the repulsive surface barrier, are localized mostly in the vacuum region.
In this chapter the theoretical predictions, the general behaviors and the distinguishing properties of the electronic surface states are reviewed in detail.
Furthermore, a brief review of the available experimental techniques used for electronic surface states investigation is provided.

2.1 Theoretical considerations on Surface States

For understanding how surface states arise, let us consider a simplified model in which the crystal has a weak periodic potential (nearly-free electron approximation), while the vacuum has a constant potential equal to V_0. The surface (at $z = 0$) is thus a sharp step between the strictly periodic lattice and the vacuum, see Figure 2.1.

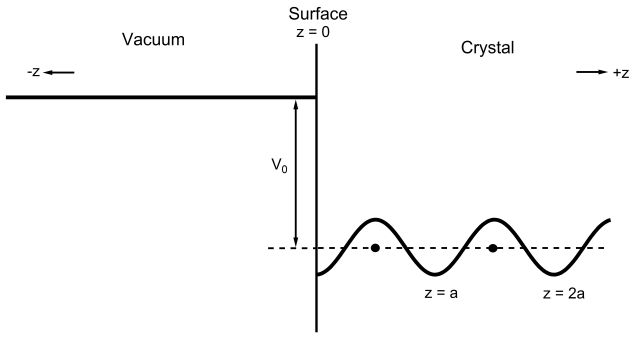

Figure 2.1: Schematic representation of a crystal surface. The crystal extends in the half-plane $z > 0$ and has a weak periodic potential (nearly free-electron approximation), with the termination at the surface achieved by a step potential. The vacuum ($z < 0$) has a constant potential, V_0.

The one-dimensional potential in the z direction (perpendicular to the surface), supposing that the semi-infinite crystal occupies the half-space with $z > 0$ and the vacuum $z < 0$, may be written as:

$$\begin{cases} V(z) = V_0 \quad \text{for} \quad z < 0 \\ V(z) = V(z + na) \quad \text{for} \quad z > 0 \end{cases} \tag{2.1}$$

where a is the lattice constant.

The Schrödinger equation for the one-dimensional problem is:

$$\frac{\hbar^2}{2m}\frac{d^2\psi(z)}{dz^2} + [E - V(z)]\psi(z) = 0. \tag{2.2}$$

As proposed in references [10,11], we first solve it separately for $z < 0$ and for $z > 0$ and then we deduce the solutions at $z = 0$ from the continuity condition of the wave function and its derivative. The wave function, solution of equation 2.2 in the vacuum region ($z < 0$), has the following form:

$$\psi(z) = Ae^{z\sqrt{\frac{2m}{\hbar^2}(V_0-E)}} \sim Ae^{zq'} \quad (z < 0), \tag{2.3}$$

where q' is real and positive.

In the half-plane $z > 0$, the periodic one-dimensional potential can be expanded into a Fourier series: $V(z) = \sum_g V_g e^{igz}$, where $g = \frac{2\pi}{a}n$ with $n = \pm 1, \pm 2...$ is the reciprocal lattice vector. For simplicity it is assumed that the potential is real and only the terms $n = \pm 1$ in g are taken into account. Within this assumptions the crystal potential may be written as:

$$V(z) = 2V \cos \frac{2\pi}{a} z \quad (z > 0). \tag{2.4}$$

As shown in Figure 2.1 the considered potential is repulsive at the ion cores and attractive between them. Moreover, the sign of V depends on the position of $z = 0$: if it has been setted between the ions, as in Figure 2.1, $V < 0$, while if $z = 0$ is at the site of ion cores, $V > 0$.

In the simple model of free electron in one-dimension the eigenstates

$$\psi_k(z) = \frac{1}{\sqrt{a}} e^{ikz} \tag{2.5}$$

with energies

$$E^{(0)} = \frac{\hbar^2 k^2}{2m} \tag{2.6}$$

are twice degenerate, for k and $-k$. Thus the wave function in the zero-order approximation may be written as a linear combination of plane waves $\psi(k, z) = \alpha\psi_k(z) + \beta\psi_{-k}(z)$. This is true for any k and in the case of a periodic perturbation has non-zero matrix elements only if the initial and final states are related by the reciprocal lattice wave-number $|\mathbf{k}| = |\mathbf{k}' + \mathbf{g}|$ [12]. Therefore the wave function may be written in the following form:

$$\psi(k, z) = e^{i(kz)}[\alpha + \beta e^{-igz}] = \alpha e^{ikz} + \beta e^{i(k-g)z} \tag{2.7}$$

where, for convenience, only the term $g = \frac{2\pi}{a}$ and $k \cong \frac{\pi}{a}$ are regarded here. In a one-dimensional model, only the z component of the vectors is considered, i.e. k_z and g_z; here, the index z is omitted, remembering, however, that all wave vectors are normal to the surface.

In the almost free electron approximation, the crystal potential $V(z)$ distorts the free-electron band and opens up gaps at the Brillouin Zone (BZ) boundaries, i.e. $k = \pm\frac{\pi}{a}$, $k = \pm\frac{2\pi}{a}$,... (Figure 2.2) , in which the electronic states with energies lying in these gaps are forbidden. For $V < 0$ (origin between atomic planes) the wave functions corresponding to the energies of the top and bottom of the gap, i.e. the lowest and upper eigenvalues, respectively, fulfill these conditions:

top	$\psi(k,z) \sim \cos\left(\frac{\pi}{a}z\right)$	s type
bottom	$\psi(k,z) \sim \sin\left(\frac{\pi}{a}z\right)$	p type.

Since in the atomic systems the s level is usually below the p level, the previous gap is called "Shockley inverted gap".

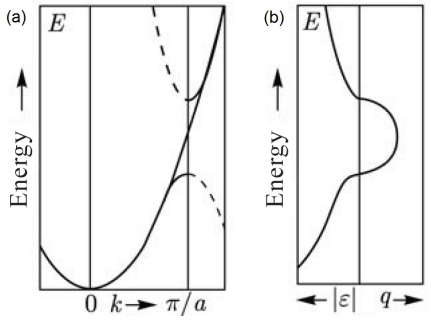

Figure 2.2: Energy bands of the electronic states in the nearly free electrons approximation for the one-dimensional periodic potential. Taken form [13].

The solutions of the Schrödinger equation can be extended into the gap by using a complex **k**-vector:

$$k_z = p \pm iq \tag{2.8}$$

with $p = \frac{\pi}{a}$ for a solution near the BZ boundary and q is real and positive. Also in this case, for simplicity, we drop the z-index.
Thus, from eq. 2.7 one finds:

$$\psi(k,z) = e^{(i(p\pm iq)z)}[\alpha + \beta e^{-igz}] = e^{\mp qz}e^{ipz}[\alpha + \beta e^{-igz}]. \tag{2.9}$$

Due to the real exponential function that diverges either for $z \to -\infty$ or for $z \to +\infty$, both the solutions are forbidden in the infinite crystal, but they are not in a semi-infinite crystal. In the chosen situation (semi-infinite crystal occupies the half-space with $z > 0$), the wave function, decaying into the crystal, may be written as:

$$\psi(k,z) = e^{-qz}e^{ipz}[\alpha + \beta e^{-igz}]. \tag{2.10}$$

Setting $\alpha = e^{i\delta}$ and $\beta = e^{-i\delta}$, after some calculation one finds:

$$\psi(k,z) = Be^{-qz}\cos\left(\frac{\pi}{a}z + \delta\right) \tag{2.11}$$

where, for the chosen case ($V < 0$), $\delta = 0$ for the wave function at the top of the gap and $\delta = -\frac{\pi}{2}$ at the bottom.

The two coefficients A and B of equations 2.3 and 2.11, respectively, are derived by imposing the continuity of the wave function and its derivative at $z = 0$.
A careful analysis reveals that the wave functions outside and inside the crystal can be matched, in principle, only for $V < 0$, while for $V > 0$ a matching of the wave functions is impossible. The derivatives at the origin $z = 0$ for the wave functions decaying into the vacuum and into the crystal, from eq.2.3 and eq.2.11, respectively, are:

$$\left.\frac{d\psi}{dz}\right|_{z=0} = Aq'e^{q'z}|_{z=0} = Aq' > 0 \tag{2.12}$$

and

$$\left.\frac{d\psi}{dz}\right|_{z=0} = \left\{Bpe^{-qz}[-\sin(pz+\delta)] - qe^{-qz}\cos(pz+\delta)\right\}\Big|_{z=0} =$$

$$= B[p(-\sin\delta) - q\cos\delta] < 0 \tag{2.13}$$

for $p > 0$ ($p = \pi/a$ near the Brillouin Zone boundary) and $0 < \delta < \pi/2$. Within these conditions a matching of the wave functions at the surface is impossible (see Figure2.3a), while for $V < 0$ the matching of the wave functions inside and outside the crystal is in principle feasible. Figure 2.3b shows the wave functions decaying into the crystal at the bottom and at the top of the gap, i.e. $\delta = -\pi/2$ and $\delta = 0$, respectively. The matching of the wave functions at the surface for these edge cases is not possible; however for $0 < \delta < \pi/2$ there is a region where matching the slopes of the wave functions is possible and a surface state can exist. The matching condition in the logarithmic derivative $[(d\phi/dz)/\phi]$ can be simply written as:

$$\left.\frac{d\psi/dz}{\psi}\right|_{vacuum} = \left.\frac{d\psi/dz}{\psi}\right|_{crystal} \tag{2.14}$$

and thus

$$q' = -q - p\tan\delta. \tag{2.15}$$

Thus, let us summarize the results obtained above: in an infinite crystal the solutions of the Schrödinger equation have a real wave vector **k**. The periodic crystal potential modifies the free-electron states opening gaps at the Brillouin zones (Figure 2.2). In these energy gaps, electronic states are forbidden, however, if one assumes a complex wave vector **k**, electronic states can lie in the gap and the associated wave functions, containing a real exponential function (see eq. 2.11), exponentially decay inside the crystal, i.e. for $z \to +\infty$. The energies corresponding to these electronic states are in the energy gap between the bands (Figure 2.2b). One of the solutions in the crystal can be connected with the solution in the vacuum region; this is the case in which the electron is localized in a narrow region close to the surface and it leads to states confined to the surface, i.e. *the Surface States*.

Surface states can be divided in two categories: those mainly localized in the first atomic layer, the intrinsic surface states, and those mostly in the vacuum region, the image potential states. As regards the former category, it is customary to distinguish between *Tamm* [14] and *Shockley* [15] surface states. The Tamm surface states, that owe their name to the Soviet physicist I.E. Tamm, who was the first in 1932 to predict the formation of this kind of surface states, arise from a splitting of unperturbed bulk bands (i.e. d and f valence band states) in the crystal due to the potential change at the surface. In the

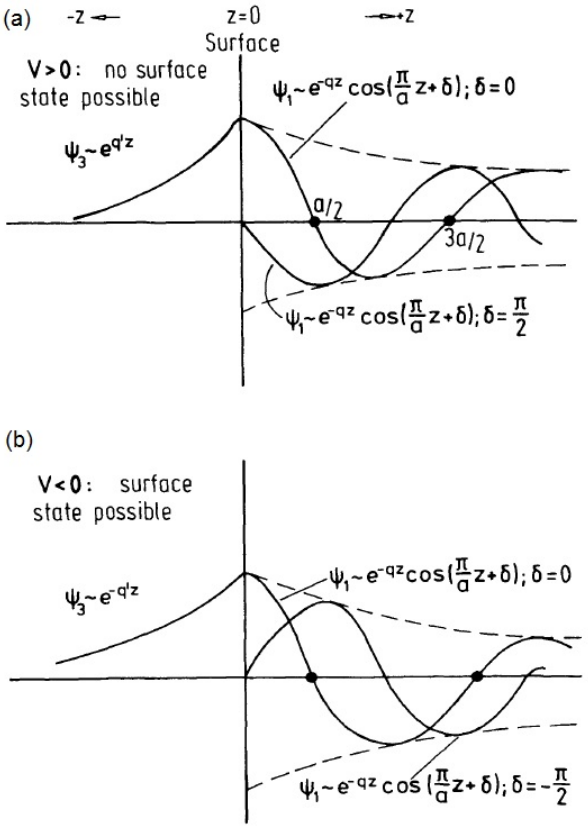

Figure 2.3: Matching conditions of the wave functions at the top and at the bottom of the gap with the wave function outside the crystal, for $V > 0$ (a) and $V < 0$ (b). Only for $V < 0$ a surface state can exist somewhere near the bottom of the gap. Adapted from [10].

simple case shown in Figure 2.4a, the Tamm state derives from a shift of the localized (i.e. nearly dispersionless) d band, due to the fact that the d band states close to the surface experience a weaker crystal potential than the bulk d states. The Shockley surface states, discovered by William Shockley in 1939, instead, arise at the surface due to the boundary conditions introduced for a semi-infinite crystal. While Tamm states decay slowly into the crystal and may

overlap energetically the bulk states, the Shockley surface states have a short penetration into the solid and they are characterized by energy eigenvalues that lies in a forbidden band gap (i.e. E_g in Figure 2.4b). Their localization into the gap can be understood if one accepts an imaginary part in the z-component of the crystal momentum **k**, as shown previously.

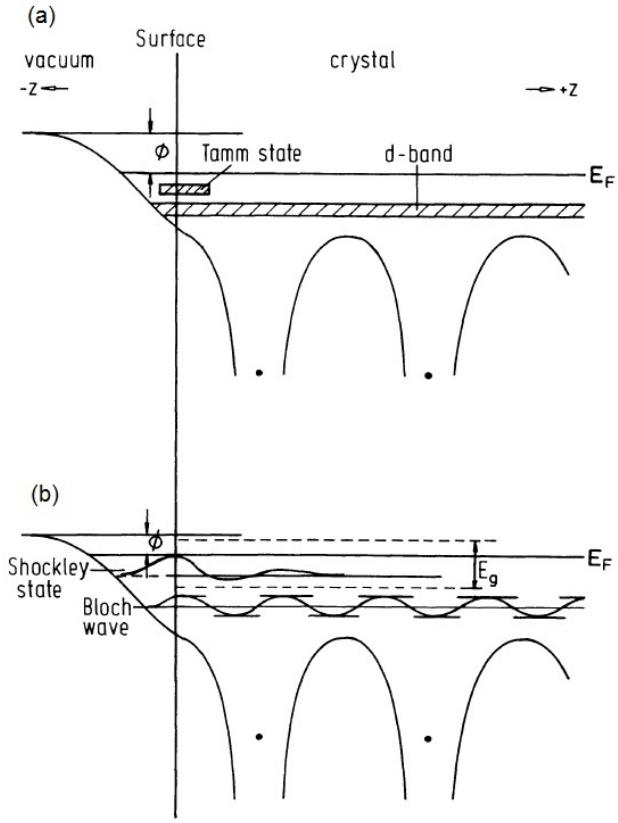

Figure 2.4: (a) Tamm state. It arises from a split-off from the d band, due to the potential change at the surface. (b) Shockley state. It is created in a gap (E_g) of the bulk-band structure due to the termination of the crystal by the surface. Adapted from [10].

The second category of surface states, the Image Potential States, are detailed in the next section.

2.2 The phase shift model

Another way for describing the origin of the surface states has been proposed by Echenique and Pendry [16] in 1978 and then widely developed by Smith [17]. They described a surface state as a wave trapped between the bulk crystal, due to the presence of a forbidden band gap, and the surface barrier potential. The model distinguishes an electron outside the crystal that moves towards the crystal (ψ_+) or away from the surface (ψ_-), as shown in Figure 2.5. Such electron wave function is reflected back and forth, between the crystal surface and the barrier potential.

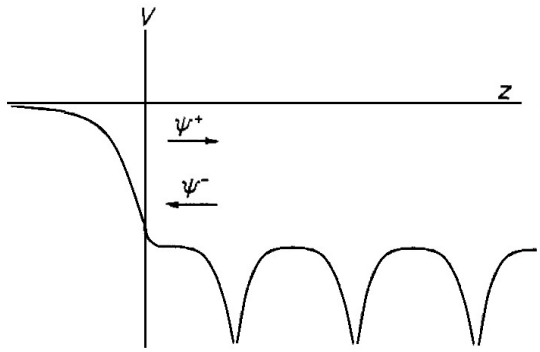

Figure 2.5: Schematic representation of the potential of the bulk solid lattice ($z > 0$) and the surface potential outside the crystal surface ($z < 0$) in the Echenique-Pendry model. Taken from [16].

If a wave ψ_+ moves towards the crystal, a portion will be reflected at the surface and the reflected beam ψ_-can be written as:

$$\psi_- = r_C e^{i\phi_C} \psi_+ \tag{2.16}$$

In turn ψ_- will impinge on the vacuum potential barrier and the reflected beam will be:

$$\psi_+ = r_B e^{i\phi_B} r_C e^{i\phi_C} \psi_+ \tag{2.17}$$

where r_B and r_C are the real parts of the reflection coefficients, while ϕ_B and ϕ_C are the phase changes occurring upon reflection at the barrier and at the crystal surface, respectively.
Summing an infinite number of reflections you get that the total amplitude ψ_+^{TOT} can be written in the form:

$$\psi_+^{TOT} = \psi_+ + r_B r_C e^{i(\phi_B+\phi_C)}\psi_+ + r_B^2 r_C^2 e^{2i(\phi_B+\phi_C)}\psi_+ + ... =$$

$$= \psi_+ \Big[1 - r_B r_C e^{i(\phi_B+\phi_C)}\Big]^{-1}. \tag{2.18}$$

The presence of a surface state requires that all the intensity of ψ_+ must be stacked at the surface and, therefore, the total intensity of eq. 2.18 must be infinite. This is possible if the following conditions are satisfied:

$$r_B r_C = 1 \quad \text{and} \quad \phi_C + \phi_B = n2\pi \quad \text{with } n \text{ integer.} \tag{2.19}$$

Since $r_B, r_C \leq 1$, the first condition is true only if $r_B = r_C = 1$.

This means that the electron is completely reflected at the potential barrier ($r_B = 1$), if it has an energy $E < E_V$, and at crystal surface ($r_C = 1$), if its energy corresponds to an energy gap in the crystal bulk band structure. Now, let's check if this model leads to the same results obtain in section 2.1 with standard model. Applying the matching condition of the derivative, eq. 2.14, with

$$\psi_{vacuum} = e^{ikz} + e^{-ikz} e^{i\phi_C} \quad (r_C = 1), \tag{2.20}$$

it results that:

$$\left.\frac{d\psi/dz}{\psi}\right|_{vacuum} = \left.\frac{d\psi/dz}{\psi}\right|_{crystal}$$

$$k\tan(\phi_C/2) = -q - p\tan\delta, \quad k = \sqrt{\frac{2mE}{\hbar^2}}, \tag{2.21}$$

where the logarithmic derivative outside the surface (left-hand side) has been calculated from eq.2.20, and inside the crystal it is that estimated before (eq.

2.15). If we consider the lowest energy state ($n = 0$), the second condition of eq. 2.19 is

$$\phi_C + \phi_B = 0 \quad \text{for} \quad n = 0. \tag{2.22}$$

Applying the matching condition at the surface, eq. 2.14, with $\psi_{crystal} = e^{-ikz} + e^{ikz}e^{i\phi_B}$ and $\psi_{vacuum} \sim e^{q'z}$, it is found that:

$$k \tan(\phi_B/2) = -q'. \tag{2.23}$$

Since $\phi_C = -\phi_B$, if eq.2.23 is inserted in the above matching condition (eq. 2.21), it results that:

$$+k(q'/k) = -q - p\tan\delta \quad \text{and} \quad q' = -q - p\tan\delta \tag{2.24}$$

which is exactly the condition found in the standard model (eq.2.15).

2.2.1 The Image Potential States

As shown above, the phase shift model, relying on multiple reflection theory of plane wave components, is an interesting model to describe the properties of surface states. In particular, in addition to the lowest-order solution ($n = 0$), that, according to the standard model described in section 2.1, gives the Shockley state, the Echenique-Pendry model gives higher order solutions ($n = 1, 2, ...$). These additional states are called **Image Potential States**, IPSs. They may be considered as a particular case of surface states. In this case, an electron outside a metal surface can not escape into the vacuum, because its presence in front of the surface repels electrons in the solid, creating a positive image charge inside the metal (Figure 2.6a) [16, 18–20]. Thus the electron in front of the surface neither can fall into the bulk, for the presence of a forbidden bulk band gap at its energy, nor can escape into the vacuum, due to the potential barrier created by the image charge inside the solid. This potential well leads to a series of discrete hydrogen-like electronic states that extend into the vacuum for several Å (see Figure 2.6b).

Far from the image plane, i.e. $z >> z = 0$, the potential is well approximated by a one-dimensional Coulomb potential:

$$V(z) \approx \frac{1}{4z} \quad \text{for} \quad z >> 0. \tag{2.25}$$

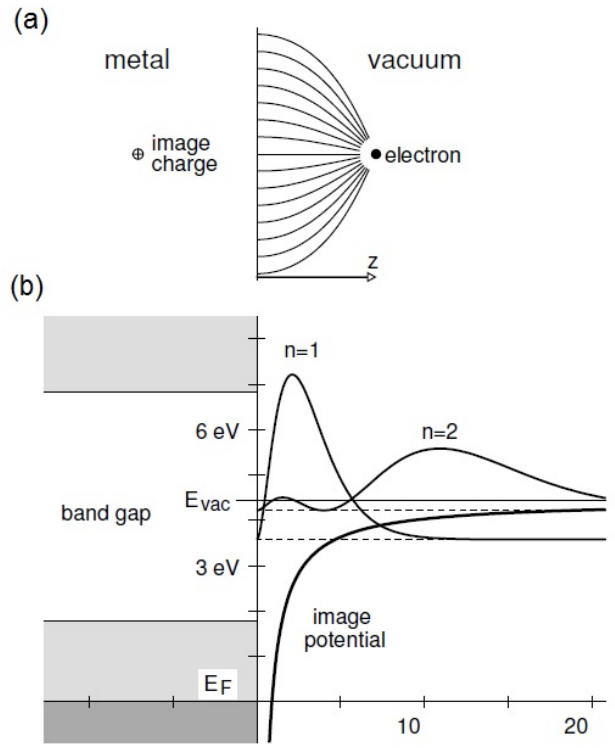

Figure 2.6: (a) Sketch of the electric field lines for an electron at a distance z in front of a metal surface. In an idealized picture this field can be explained by assuming the existence of a positive image charge inside the solid at z. The image plane is at z=0. (b) Sketch of the potential well formed by the band gap (unshaded area in the metal) and the Coulomb potential. The squares of the wave functions associated to the first three terms of a series of discrete hydrogen-like electronic states are also shown. Adapted from [21].

When a wave function is reflected by the potential in eq. 2.25, its phase shift ϕ_B is modified according to the following equation [17, 20]:

$$\phi_B = \pi \left(\sqrt{\frac{3.4\text{eV}}{\epsilon}} - 1 \right). \tag{2.26}$$

Imposing the stationarity condition $\phi_C + \phi_B = 2\pi n$ ($n \in \aleph$) we obtain:

$$\begin{aligned} \pi \left(\sqrt{\frac{3.4\text{eV}}{\epsilon}} - 1 \right) + \phi_C &= 2\pi n \\ \sqrt{\frac{3.4\text{eV}}{\epsilon_n}} &= 2n + 1 - \frac{\phi_C}{\pi} \\ \sqrt{\epsilon_n} &= \frac{\sqrt{3.4\text{eV}}}{2n + 1 - \phi_C/\pi}. \end{aligned} \tag{2.27}$$

Defined the quantum defect parameter a as:

$$a = \frac{1}{2} \left(1 - \frac{\phi_C}{\pi} \right) \tag{2.28}$$

where, since in a Shockley inverted gap ϕ_C continuously varies from π in the upper edge to 0 in the lower edge, a ranges from 0 at the top to 1/2 at the bottom of the gap, finally, we find a Rydberg series of hydrogen-like states labeled by the quantum number n, whose binding energies are:

$$\epsilon_n = \frac{3.4\text{eV}}{(2n + 1 - \phi_C/\pi)^2} = \frac{3.4\text{eV}}{4[n + (1 - \phi_C/\pi)/2]^2} = \frac{0.85\text{eV}}{(n + a)^2}. \tag{2.29}$$

As expected for a Rydberg sequence, between the vacuum energy E_V and ϵ_1 there are an infinite number of states with energies difference between two neighbor states that vanishes approaching E_V as n increases to infinity. Since the image potential state can be described as a 2D free electron gas trapped in front of a solid surface, the energy dependence on $\mathbf{k}_{||}$ is expected to show a free electron parabolic dispersion, yielding to the following expression for the total energy:

$$E(k_{||}) = \epsilon_n + \frac{\hbar^2 k_{||}^2}{2m^*} \tag{2.30}$$

where m^*/m_e is the effective mass.

As stressed above, IPS are unoccupied surface states which are energetically located close to the vacuum level. Thus, an electron in a IPS has a certain

probability of decaying into an empty bulk state, within a certain decay time. The classical solution for the round-trip period of the electron reflected back and forth in the potential well between the surface and the image potential is [22]:

$$T = \sqrt{\frac{m}{2}} \frac{e^2}{16\epsilon_0} |E|^{-3/2}. \tag{2.31}$$

If the quantum-mechanical expression for the IPS eigenvalues at $\mathbf{k}_{||} = 0$ is inserted in eq. 2.31, the round-trip period for the n-th state can be written as:

$$T_n = \frac{8h}{R_y}(n+a)^3 \tag{2.32}$$

where $R_y = 13.6$ eV is the Rydberg constant. Thus, a longer lifetime is expected for the IPS with greater quantum numbers n due to the localization of their wave functions mainly in the vacuum, which results in a smaller overlap with the solid with respect to the IPS wave functions with smaller n.

2.3 Experimental investigation of Surface States

In this section the most used experimental techniques for the study of the electronic surface states, both intrinsic surface states and image potential states, are briefly reviewed.

2.3.1 Photoemission Spectroscopy

An excellent tool to investigate the electronic states in solids and at solid surfaces is represented by PhotoEmission Spectroscopy (PES). PES is a surface sensitive technique and it allows to characterize the electronic properties of the topmost surface layers [10]. The conventional photoemission process is sketched in Figure 2.7a: if the solid surface is irradiated with a photon energy $h\nu$ exceeding the work function Φ, the absorption of a photon can excite an electron below the Fermi level E_i into a state which is energetically above the vacuum level , E_{vac}. The photoelectron in a free-electron state ($E_{kin} = \frac{p^2}{2m_e}$) is detected by an analyzer which determines its kinetic energy E_{kin}. From the conservation of the energy the binding energy of the initial state E_i relative to the Fermi

level E_F can be derived from the following expression [21, 23]:

$$E_i = h\nu - E_{kin} - \Phi \tag{2.33}$$

where $\Phi = E_{vac} - E_F$.

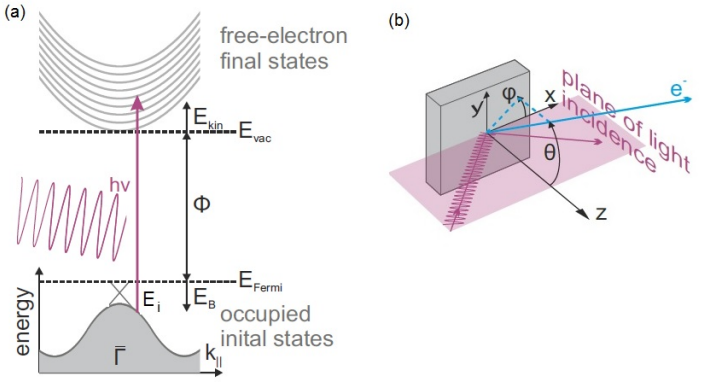

Figure 2.7: (a) Schematic representation of the photoemission process. The kinetic energy E_{kin} of the electron leaving the surface is measured relative to the vacuum energy E_{vac}. (b) Photoemission geometry: the electron is photoemitted with an angle θ with respect to the normal at the surface z and detected by an analyzer. Taken from [24].

For the studied systems, the crystalline translation symmetry in the bulk is broken at the surface and the conservation of the total momentum can not be assumed; in particular, considering the total momentum as the sum of two components, the parallel $\mathbf{k}_{||}$ and perpendicular momentum $\mathbf{k}_{\perp}$, since the symmetry is broken along the z direction only $\mathbf{k}_{||}$ is conserved at the surface, i.e. $\mathbf{k}_{||}^{crystal} = \mathbf{k}_{||}^{vacuum}$.
The momentum of the photons in the UV region, characteristic spectral range for photoemission from the valence band, is of about 10^{-3}Å^{-1}; thus it is negligible compared to the experimental resolution.
The conservation of the parallel momentum of the photoemitted electron and of its energy (eq. 2.33) allow us to uniquely determine the dispersion band of

the crystal in the direction parallel to the surface plane ($E(\mathbf{k}_{||})$), by measuring the energy and the angle of the electrons photoemitted from crystal (Angle-Resolved PES). Thus the modulus of $\mathbf{k}_{||}$, with respect to the reference frame of Figure 2.7b is:

$$k_{||} = \frac{p \sin\theta}{\hbar^2} = \sqrt{\frac{2m_e}{\hbar^2} E_{kin}} \sin\theta. \tag{2.34}$$

The reconstruction of the bulk band structure $E(\mathbf{k}_{||}; \mathbf{k}_{\perp})$ is more difficult, since $\mathbf{k}_{\perp}$ is not conserved, but for studying the electronic states at surface, scope of the present work, the knowledge of the momentum perpendicular to the surface is not necessary.

Although PES represents a powerful tool to investigate the electronic structure at the surfaces, it is limited to initial states below the Fermi level (E_F) and to final state above the vacuum level (E_{vac}). In order to investigate the unoccupied states in the range between E_F and E_{vac} other investigation methods are necessary.
From 1980s Inverse Photoemission (IPES) was widely used in order to investigate unoccupied surface states, such as Image Potential States [25–27]. The Inverse Photoemission process is simply the photoemission process performed in a reversed mode: electrons of varying energy are sent onto a sample and the photons produced are then detected. The common measuring mode, known as Bremsstrahlung Isochromat Spectroscopy (BIS), consists of a monochromatic electron beam impinging on the material surface; these electrons have a finite probability of decaying from the free-electron state into an empty state of the crystal causing the emission of a photon (see Figure 2.8). In this mode the photon detection energy is kept fixed while the energy of the incoming electrons is changed [10]. As shown in Figure 2.8, PES and IPES are complementary techniques in the investigation of surface states: the former allows the study of the energy levels below E_F, while the second of the empty states between the vacuum level E_{vac} and E_F, but each of the techniques has an energy range which is inaccessible (shaded regions of Figure 2.8). Moreover, while in PES the energy resolution is generally limited by the energy analyzer, in IPES the energy distribution of the incoming electrons (typically several hundred of meV) limits the energy resolution, which results has been at best about 0.26 eV, inferior to photoemission by more than an order of magnitude [21].

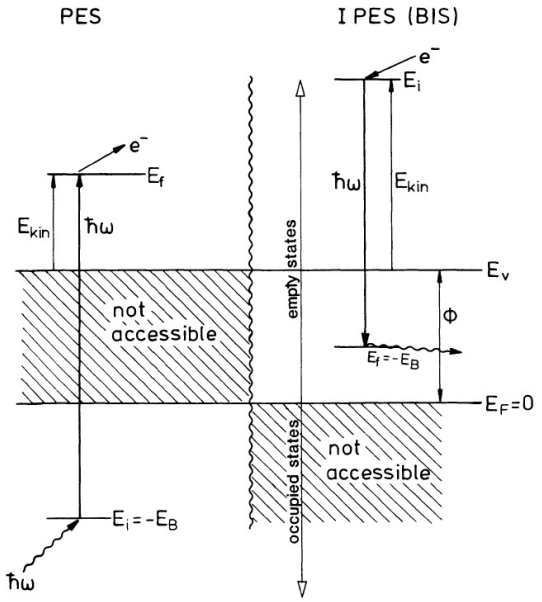

Figure 2.8: Schematic energy diagrams for PhotoEmission Spectroscopy PES (on the left-hand scheme) and Inverse PhotoEmission Spectroscopy IPES (on the right-hand scheme). In PES the energy range between the Fermi energy and the vacuum level is not accessible, while in IPES the unaccessible range is that below E_F. Taken from [10].

2.3.2 Two-Photon Photoemission Spectroscopy

An excellent alternative to achieve at the same time high resolution and accessibility on both the range between E_F and E_{vac} and the energy region below E_F is represented by Two-Photon PhotoEmission (2PPE) spectroscopy (also named Non-Linear PhotoEmission Spectroscopy, NL-PES). Since the crystal surface is irradiated with a photon of energy lower than the work function Φ (in general the incident photons are in the near-UV or visible range), direct photoemission from occupied states does not occur, but, due to the high intensity of the ultrashort laser pulses employed in this technique multi-photons transitions are possible. The 2PPE transition scheme is shown in Figure 2.9a: the first photon ($h\nu_{pump}$) excites an electron from an initial state E_i, which can

be both a discrete surface state or a continuum, to an intermediate empty state E_{im}, then a second photon ($h\nu_{probe}$), of the same energy (i.e. monochromatic 2PPE) or different energy from the first one (i.e. bichromatic 2PPE), brings the electron into the final state E_f above E_{vac}. The intermediate state can be real, such as the IPS, or virtual. In the former case the E_{im} can be populated by photon excitation only if $h\nu_{pump} \geq E_{im} - E_F$ and if the lifetime of the electron in E_{im} is sufficiently long to absorb a second photon, in the second case, instead, the final state is achieved through a direct two-photons ionization process from an occupied state E_i.
A characteristic 2PPE spectrum, representing the energy distribution curve of the photoelectrons whose number is measured as a function of their kinetic energy, is shown in Figure 2.9b. The spectrum, acquired with a photon of energy $h\nu = 4.10$ eV on Ag(100) surface presents the $n = 1$ IPS at a kinetic energy of ~ 3.5 eV and a large features at lower energies. The low-energy cutoff corresponds to electrons leaving the solid surface with negligible kinetic energy.

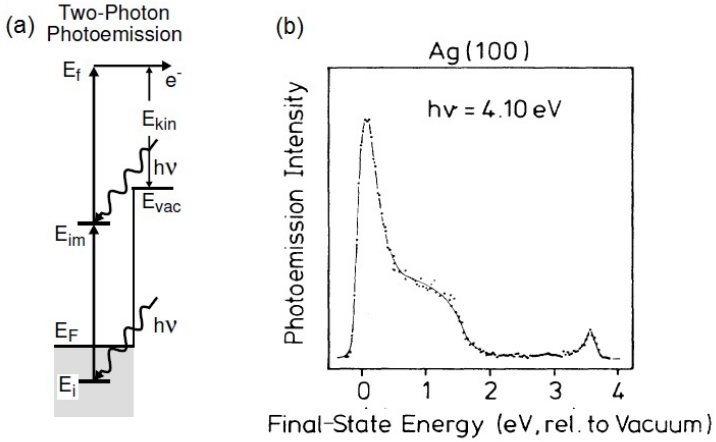

Figure 2.9: (a)Schematic representation of two-photon photoemission process: an electron in E_i is excited in an intermediate empty state E_{im} and then photoemitted by a second photon. Taken from [21] (b) 2PPE spectrum acquired on Ag(100) surface at $k_{||} = 0$ with a photon of energy 4.10 eV. Adapted from [28].

In the second-order perturbation theory for the simplest case of two-photon absorption in a continuous wave light field and for the more general case of bichromatic 2PPE ($h\nu_{pump} \neq h\nu_{probe}$), the transition matrix element is [24, 29]:

$$\begin{aligned} M_{i,f} &= \left\langle \psi_f | \tilde{V}^*(\mathbf{A}_{pump}, \mathbf{A}_{probe}) | \psi_i \right\rangle \\ &+ \sum_{im} \left[\frac{\left\langle \psi_f | \tilde{V}(\mathbf{A}_{probe}) | \psi_{im} \right\rangle \left\langle \psi_{im} | \tilde{V}(\mathbf{A}_{pump}) | \psi_i \right\rangle}{(E_{im} - E_i - h\nu_{pump})} \right. \\ &+ \left. \frac{\left\langle \psi_f | \tilde{V}(\mathbf{A}_{pump}) | \psi_{im} \right\rangle \left\langle \psi_{im} | \tilde{V}(\mathbf{A}_{probe}) | \psi_i \right\rangle}{(E_{im} - E_i - h\nu_{probe})} \right] \end{aligned} \tag{2.35}$$

where ψ_i, ψ_{im} and ψ_f are the initial, intermediate and final states, corresponding to the energy eigenvalues E_i, E_{im} and E_f, respectively. The light field is assumed as a plane wave of the form $\mathbf{A} = \mathbf{A}_0 e^{i(\mathbf{qr})}$. The direction of A_0 gives the polarization of light, since $\mathbf{E} = -\frac{\partial \mathbf{A}}{\partial t}$.
According to the Fermi golden rule, the probability of the photoemission process $P_{i,f}$ is proportional to $|M_{i,f}|^2 \delta(E_f - E_i - h(\nu_{pump} + \nu_{probe}))$. The two terms in the square brackets take into account that in the bichromatic case two processes take place simultaneously: a pump photon $h\nu_{pump}$ may excite an electron in an intermediate state and then the probe photon $h\nu_{probe}$ photoemits it or vice versa. Only in the monochromatic case the two terms are identical.

The selection rules can be derived considering the individual step of a photoemission process from an intermediate state, i.e. IPS. In this case the transition matrix element is simply $M_{i,f} = \left\langle \psi_f | \tilde{V}(\mathbf{A}) | \psi_i \right\rangle$. $\tilde{V}$ is found by substituting $\mathbf{p} \to \mathbf{p} - e\mathbf{A}$ in the Hamiltonian V and neglecting the quadratic term in the vector potential $\mathbf{A}$:

$$V = \frac{1}{2m}(-e\mathbf{Ap} - e\mathbf{pA} + e^2\mathbf{A}^2) = \frac{1}{2m}(-2e\mathbf{Ap} + ei\hbar(\nabla \mathbf{A}) + e^2\mathbf{A}^2) \approx -\frac{e}{m}\mathbf{Ap}. \tag{2.36}$$

Considering an IPS as the initial state $|\psi_i\rangle = |n, \mathbf{k}_{||}\rangle$ and a free electron state as final state $|\psi_f\rangle = |\mathbf{k}'\rangle = (2\pi)^{-3/2} e^{i\mathbf{k}'\mathbf{r}}$, the momentum operator $\mathbf{p}$ acts in the following way on the two states:

$$\mathbf{p}|n,\mathbf{k}_{||}\rangle = -\hbar\mathbf{k}_{||}|n,\mathbf{k}_{||}\rangle - i\frac{\partial}{\partial z}|n,\mathbf{k}_{||}\rangle \tag{2.37}$$

$$\mathbf{p}|\mathbf{k}'\rangle = \hbar\mathbf{k}'|\mathbf{k}'\rangle. \tag{2.38}$$

Considering the components parallel and perpendicular to the surface for the polarization vector A_0 and for the final state momentum $\mathbf{k}'$, the transition matrix element may be written as:

$$M_{i,f} = \hbar\mathbf{A}_{0,||}\cdot(\mathbf{k}'_{||}-\mathbf{k}_{||})\langle\mathbf{k}'|e^{i\mathbf{q}\cdot\mathbf{r}}|n,\mathbf{k}_{||}\rangle + \tag{2.39}$$

$$+\hbar\mathbf{A}_{0,z}\left[k'_z\langle\mathbf{k}'|e^{i\mathbf{q}\cdot\mathbf{r}}|n,\mathbf{k}_{||}\rangle - \langle\mathbf{k}'|e^{i\mathbf{q}\cdot\mathbf{r}}i\frac{\partial}{\partial z}|n,\mathbf{k}_{||}\rangle\right]. \tag{2.40}$$

The first term in eq. 2.40, considering the 2D free-electron character of the IPS, can be written as:

$$\langle\mathbf{k}'|e^{i\mathbf{q}\cdot\mathbf{r}}|n,\mathbf{k}_{||}\rangle = \delta(\mathbf{k}_{||}-\mathbf{k}'_{||}-\mathbf{q}_{||})\frac{1}{2\pi}\int dz u_n(z)e^i(k'_z-q_z)z \tag{2.41}$$

where, for the conservation of the parallel momentum $\mathbf{k}'_{||}-\mathbf{k}_{||}-\mathbf{q}_{||}=0$ and, since the parallel component of the photon $\mathbf{q}_{||}$ is negligible at normal incidence, $\mathbf{k}'_{||}-\mathbf{k}_{||}=0$. Thus, for photoemission processes from the IPS, the first matrix element of eq. 2.40 vanishes. This means that the light component parallel to the surface $\mathbf{A}_{0,||}$ does not contribute to the photoemission from an image potential state, but that the transition process from IPS to final state can be excited only from the light component perpendicular to the surface [30].

Moreover, it should be pointed that, if the energetic separation of the intermediate and the initial state is exactly the pump photon energy, the denominator of eq. 2.35 decreases and the intensity in photoemission process increases. In this condition optical transitions between ψ_i and ψ_{im} is possible and a resonance occurs [31]. Figure 2.10 shows the 2PPE spectra collected on Cu(111) surface by slightly detuning the photon energy around the resonance photon energy, i.e. $h\nu_{res} = E_{im} - E_i$. Off resonance, in addition to a significant decreasing of the peak intensity, two distinct peaks, corresponding to the initial and to the intermediate state, respectively, are observed. These peaks can be easily assigned to an initial occupied state or intermediate empty state, depending on the energy shift of the 2PPE structure relative to the exciting photon energy.

The photoelectron kinetic energy in the final state E_f of an occupied state below E_F photoemitted by a coherent two-photon excitation is given by [32]:

$$E_f = h\nu_{pump} + h\nu_{probe} + E_i, \tag{2.42}$$

while the photoelectron energy E_f of an intermediate state E_{im} populated by $h\nu_{pump}$ and subsequently excitated above E_{vac} by $h\nu_{probe}$ varies as:

$$E_f = h\nu_{probe} + E_{im}. \tag{2.43}$$

Thus in the case of monochromatic 2PPE ($h\nu_{pump} = h\nu_{probe} = h\nu$) the energy position of an occupied state shifts as twice the photon energy ($2\Delta h\nu$), while that of an unoccupied state as the laser photon energy ($1\Delta h\nu$), see Figure 2.10b.

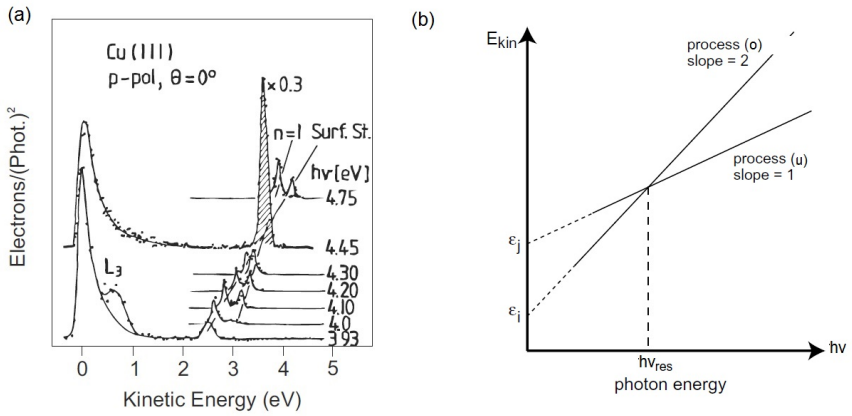

Figure 2.10: (a)Two-photon photoemission spectra collected on Cu(111) surface by changing the pump photon energy. The two peaks from their photon-energy dependence can be distinguished in initial-state (Surf. St.) and intermediate-state ($n = 1$). When the two peaks coincide, the photoemission intensity is intensified due to resonance effects. Taken from [33].(b) Photoelectron kinetic energy versus photon energy $h\nu$. Process (o) represents coherent excitation from an occupied state, process (u) the 2PPE process from an unoccupied intermediate state. The energy of the resonat excitation is $h\nu_{res} = E_{im} - E_i$. Adapted from [32].

Furthermore the structures in 2PPE spectra can change also with the angle of emission (**Angle-Resolved 2PPE**). By measuring the energy of the electrons

photoemitted at different angles between the electron spectrometer and the normal to the surface, thus different parallel momentum vectors $\mathbf{k}_{||}$, we are able to determine the dispersion band in the plane parallel to the surface ($E(\mathbf{k}_{||})$).

In addition to the mapping of the unoccupied surface band structure, 2PPE from an ultrafast laser source enables time-resolved experiments. In particular, **Time-Resolved 2PPE** spectroscopy is a suitable technique to directly measure the lifetime of an intermediate state, such as IPS. In a pump-probe configuration: the probe pulse which ionizes the intermediate state is temporally delayed with respect to the pump pulse which populates it. The resulting time-resolved spectra show a decreasing of the signal with increasing of the pump-probe delay time. The measure of the dependence of the intermediate peak intensity from the time-delay enables a direct estimation of the intermediate state depopulation time. An explanatory TR-2PPE experiment, performed on Cu(100) surface [22], is shown in Figure 2.11a. The photoemission intensities of the $n = 1, 2, 3$ IPS are plotted versus the pump-probe time-delay. The exponential decaying tails, i.e. the straight lines for the logarithmic scale, give directly the lifetimes of the three image potential states (Figure 2.11b).
The limit of this technique is the available laser-pulse width; in fact, it is possible to directly measure the intermediate state lifetime only if it is not much shorter than the temporal pulse length.

A comprehensive study of the intermediate states dynamics takes into account the evolution of the transient population as well as the dephasing of the excited electronic states. An electron in an intermediate real state (an IPS for example) experiences inelastic scattering processes that cause the decay of the population of the excited electronic state, but also quasi-elastic scattering events (so-called pure dephasing) due to scattering by phonons or defects, that cause phase change in the time evolution of electron wave function [22, 34, 35]. The latter process does not change the population in the intermediate state and, thus, it can not be detected with usual TR-2PPE measurements. However, the phase change in the scattering events, as the depopulation in the inelastic scattering processes, contributes to define the line-width Γ_n of the Lorentzian curve related to the n-th intermediate state in the 2PPE spectrum, in the following way:

$$\Gamma_n = \hbar \left(\frac{1}{\tau_n} + \frac{2}{T_n^*} \right), \tag{2.44}$$

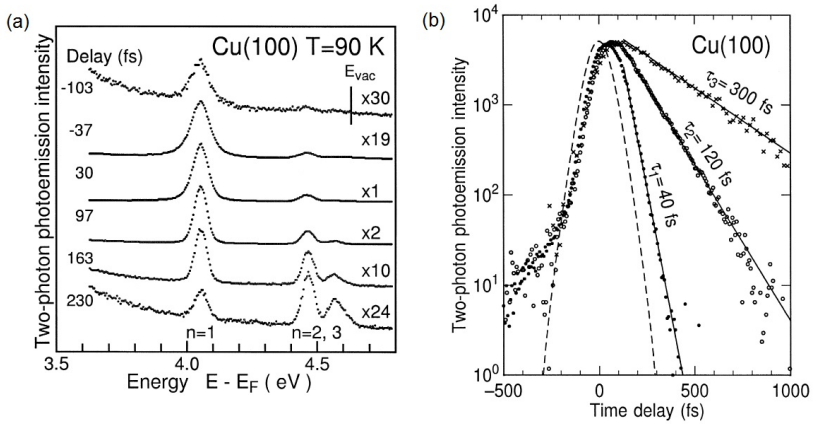

Figure 2.11: (a) 2PPE spectra acquired on Cu(100) surface at different delays between pump and probe pulse. (b) 2PPE intensity of the $n = 1, 2, 3$ IPS versus the time-delay between pump and probe pulse. The dashed line represents the pump-probe cross-correlation trace. Adapted from [22].

where τ_n is the energy relaxation time and T_n^* the pure dephasing time. Therefore, the combination of energy- and time-domain 2PPE experiments represents an excellent approach to investigate both energetic relaxation and dephasing of the excited electronic states.
This point, however, will be discussed in detail and applied to our experimental results in Chapters 4 and 5.

Experimental setup for 2PPE measurements

The basic components required for two-photon photoemission measurements consist of a laser system as light source, a UHV sample chamber and an electron energy analyzer. A schematic drawing of the experimental setup used in our experiments and available in the ELPHOS laboratory at the Università Cattolica is shown in Figure 2.12. As light source a Ti:Sapphire laser system delivering 0.8 mJ, 150 fs pulses at a wavelength of 790 nm and 1 kHz repetition rate is employed. To perform 2PPE measurements photons in the near-UV range are necessary; thus the output beam of our laser system (at $h\nu \sim$1.55 eV) undergoes one of the following pathways:

- it is focused onto beta-barium-borate (β-BBO) crystals to produce second (λ = 395 nm, $h\nu$ = 3.14 eV) and third (λ = 263 nm, $h\nu$ = 4.71 eV) harmonic of the fundamental wavelength;

- it pumps a traveling wave Optical Parametric Amplifier (OPA) covering an energy range from 0.80 to 1.07 eV. By quadrupling the output of the parametric amplifier, the photon energy could be continuously tuned from 3.20 to 4.28 eV.

Moreover, in order to investigate the occupied states below E_F, conventional PES can be easily performed using the fourth harmonic of the fundamental beam ($h\nu$ =6.28 eV) by frequency-doubling the 3.14 eV light for Second Harmonic Generation (SHG) at the surface of a BBO crystal.

The near-UV pulses are focused on the sample, kept in an UHV chamber at a residual pressure $\leq 2 \times 10^{-10}$ mbar and the photoelectrons are detected by means of a custom-made time of flight (ToF) electron spectrometer with an angular acceptance of $\pm 0.85°$ and an overall energy resolution of $\sim$ 35 meV at an electron kinetic energy of 2.0 eV.

Angle-Resolved 2PPE is performed by rotating the sample with respect to the analyzer. Varying the emission angle θ between the sample normal and the analyzer axis, the parallel crystal momenta in a range of ± 0.3 Å^{-1} around $k_{\parallel} = 0$ (normal emission) are investigated. Rotating the sample around its normal (azimuthal angle ϕ) we can chose the direction along which to perform the measurements. Moreover, for Time-Resolved 2PPE a pump-probe setup is used. The laser beam is split into two lines by a (T=70% R=30%) beam

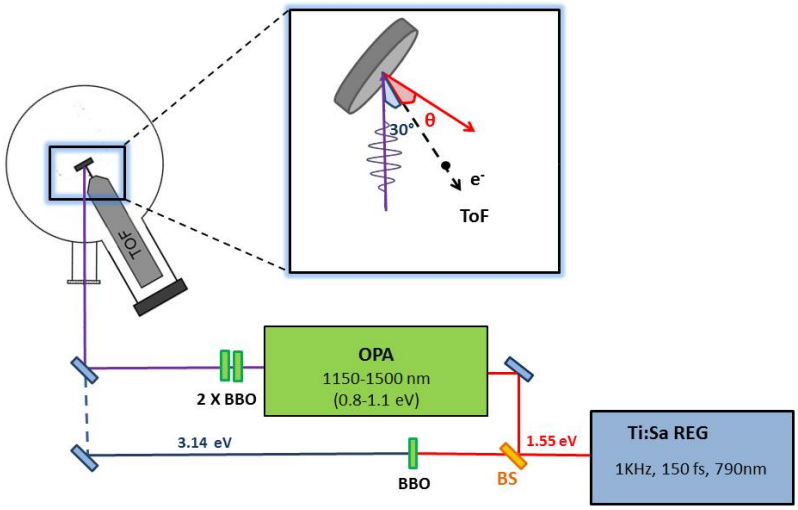

Figure 2.12: Schematic representation of the experimental setup for 2PPE measurements. The geometry configuration of the photoemission setup is shown in the zoom. The angle between the incident photon and the trajectory of analyzed electrons is fixed to 30°, whereas the angle between the surface normal and the position of the analyzer can be varied to perform angle resolved photoemission.

splitter. The probe beam is temporal delayed with respect to the pump using a delay line formed by a pair of mirrors placed on a μm sledge.

Chapter 3

Electronic dynamics of the interface states

Electronic excitations in metal systems play a key role in several physical and chemical phenomena, such as energy transfer in photochemical processes [36] or catalytic reactions. Moreover they are essential for the desorption mediated by excitations, for the oxidation of molecules at the surface [37], and also for the localization of the electrons at the interfaces [38].
Electronic surface states due to their charge density localization at the surface region are extremely sensitive to any modification or any defect at the surface. The presence of adsorbates, in particular, is very efficient in altering the dynamics of the excited states localized at the metal surface acting as a scatter for the excited electrons traveling on the surface (e.g. image potential states or intrinsic surface states) or supporting itself localized transient excited states, which represent efficient channels of charge transfer between the metal substrate and the overlayer [39]. In this chapter the electronic properties and dynamics of the excited states which live in the interfacial region are reviewed, with particular attention to the interface states at carbon-based nanostructures on metal, specifically, at graphene/metal and at organic-molecules/metal systems.

3.1 Electronic Surface States at the interfaces

The properties of the intrinsic surface states and the image potential states discussed in the preceding chapter concern the electronic states on clean metal surfaces. Henceforth, we focus on the behavior of such states when the metal surface topography is modified by the presence of adsorbates or metal (insulator) overlayers. In particular, it is expected that the image potential states, due to their charge density localization mainly into the vacuum and due to their 2D free-electron character in the surface plane, are extremely sensitive to surface modifications. Thus, information regarding the changes induced by the presence of any kind of overlayer may be inferred by changes in the electronic properties or dynamics (i.e. effective mass, binding energy,relaxation time) of IPS.
Since we deal with electronic states localized at the interfaces, hereinafter we will talk more generally about **Interface States**.
In addition to the electronic states described in the previous chapter, a particularly interesting group of surface states which occur at the interface are the so-called **Quantum Well States**, QWS. They arise from an electron traveling perpendicular to the surface within the overlayer. If the thickness of the layer is comparable to the wavelength, it is possible that standing waves in the overlayer are originated [10]. Thus, in the simplest approximation, the two interfaces, i.e. overlayer-vacuum and overlayer-substrate interfaces, might be described as potential barriers and the overlayer/substrate system might be seen as a square potential well. Therefore, in this simple framework, the Echenique-Pendry model [16], already used in previous chapter to describe the Image Potential States, can be applied for investigating the properties of such states.

As discussed above (see section 2.2), the IPS occurs if the following phase relation is satisfied $\phi_C + \phi_B = 2\pi n$, where ϕ_C is the phase shift at the crystal surface and ϕ_B the phase shift at the potential barrier in vacuum. For a quantum well state, an additional term in the phase relation has to be introduced in order to take into account the presence of an overlayer of thickness $d = ma$, where a is the lattice constant perpendicular to the surface. If the phase shift associated with the overlayer is mka, the phase relation which must be fulfilled is the following:

$$\phi_B + \phi_C + 2mka = 2\pi n. \tag{3.1}$$

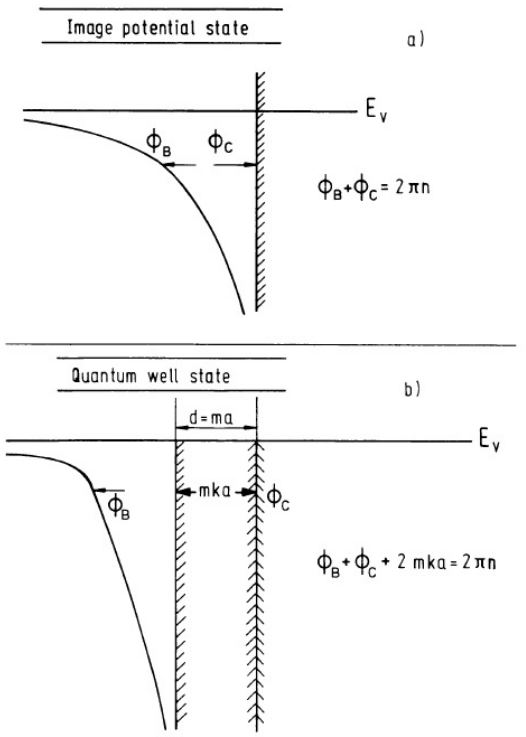

Figure 3.1: Schematic representation of the Echenique-Pendry model applied to image potential state (a) and adapted to quantum well state (b). Taken from [10].

As shown in equation 2.26, according to [17, 20], the phase shift ϕ_B at the barrier is modified as:

$$\phi_B = \pi \left(\sqrt{\frac{3.4\text{eV}}{E_V - E}} - 1 \right), \tag{3.2}$$

while ϕ_C changes following the empirical formula:

$$\phi_C = 2 \arcsin \sqrt{\frac{E - E_L}{E_U - E_L}} - \pi, \tag{3.3}$$

where E_L and E_U are the energies at the lower and at the upper band edge, respectively.

In addition to the electronic states introduced previously, it is common to find, especially in adsorbate/metal systems, new interface states, arising from the mixing of the electronic states of each system taken separately that hybridize when interacting at the interface [40,41] or related to the abrupt change of symmetry at the interface. The latter can lead to new solutions of the Schrödinger equation with a large amplitude in the interfacial region and a charge density probability that exponentially decays in both materials [42,43].

3.2 Interface states at carbon-based nanostructures on metal

Much of the research efforts in nanotechnology are currently centered around the investigation of low-dimensional carbon nanostructures. Indeed, they represent one of the most promising classes of materials, due to the huge variety of potential applications in which they are involved from optoelectronics and photonics to energy generation and storage and solar cells. However, the introduction of carbon-based devices in industrial applications is still beyond reach due to the difficulties in the production of nanostructured carbon materials with controlled properties and in the tracking of the interaction of such materials with the substrates. Nonetheless, overcoming these hurdles is nowadays mandatory for significant progresses in the realization of advanced devices based on low-dimensional carbon nanostructures.

Here we focus on two different kinds of carbon nanostructures/metal interfaces: graphene/metal systems and organic-molecules on metallic substrates.

3.2.1 Graphene/Metal interfaces

The electronic and structural properties of the interfaces between graphene and metals have been widely studied recently [6,44,45]; the possibility to synthesize high-quality graphene single layers with large area extension on metals by chemical vapor deposition (CVD), indeed, is of paramount importance in view of future technological applications where graphene is always at least partly

supported by a substrate [46, 47].
From a structural point of view, the interfaces between graphene and various metallic substrates differ in two main aspects: (i) the lattice mismatch, and (ii) the metal-graphene interaction. In terms of lattice mismatch only the Ni(111) and, possibly, the Co(0001) surfaces show a good lattice match with graphene compared to all other transition metals. This enables the formation of 1×1 structure of graphene within very large domains on these surfaces. On all the other metals, instead, the incommensurability of graphene and substrate lattices leads to a periodic lattice matching condition and to the occurrence of a moiré superstructure [45].
As regards the second point (ii), it is customary to classify the graphene/metal interfaces on the interaction between the graphene and the metal substrate; a possible assessment of the interaction strength is represented by the evaluation of graphene-metal separation. As shown in Figure 3.2 for metals strongly interacting the graphene-metal separation is around 2.1 Å while, weakly interacting metals have a separation of about 3.3 Å which is close to the distance between graphene planes in graphite. The transition from strongly to weakly interacting systems can be associated can be associated to the transition metals *d*-band center, as shown in Figure 3.2, where the plot of the graphene-metal separation versus the metal *d*-band center suggests that the transition from weakly to strongly interacting metals occurs at a *d*-band center of $\sim$2 eV.

Thus, the strong interaction of the metal with graphene leads to an important modification of graphene π bands, which hybridizing with the electronic bands of substrate close to the Fermi level, shift to $\sim$ 2 eV, opening a gap at $\bar{K}$ point of BZ and modifying the characteristic Dirac cones [44, 48]. Typical examples of strongly interacting systems are the graphene/Ni(111) [49–51] and graphene/Co(0001) [52] interfaces. On the other hand, in weakly interacting systems, the graphene sheet is only physisorbed by van der Waals forces on the substrate underneath and, thus, the linear dispersion of the graphene π bands is mostly conserved [44]. Graphene/Ir(111) [53, 54] and graphene/Cu(111) [55] are, for example, classified as weakly interacting systems, although at graphene/Ir(111) interface a small hybridization of C $2p_z$ orbitals with Ir ($d_{3z^2-r^2}$) orbitals has been observed [56].
Moreover, in addition to the different nature of the metal support, also the intercalation of foreign metals or molecules between the underlying substrate

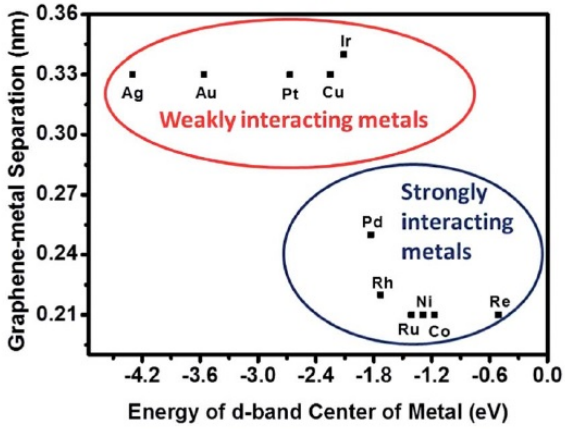

Figure 3.2: Schematic subdivision of the interactions between transition metals and graphene. The graphene-metal separation is correlated with the *d*-band center of the metal. A transition from weakly to strongly interacting metals occurs when the *d*-band center is at about 2 eV below the Fermi level. Taken from [45].

and the graphene layer can varied the strength of the graphene-metal interaction [53, 57]. The intercalation of a monolayer of gold between the graphene and the Ni(111) surface, for example, induces the shift of π bands closer to the Fermi level and the electronic decoupling of the graphene from the substrate [50]. Among molecules, oxygen intercalation has been proven to be an efficient experimental approach to decouple chemical vapor deposition grown graphene from metal substrate [58].

Independently of the kind of interaction, an interface charge transfer is observed when free-standing graphene is connected to a metallic substrate, due to work functions difference. For a perfect free-standing graphene sheet, the Fermi energy lies at the Dirac point, but its adsorption on metallic substrates can cause a shift of the Fermi energy away from the conical points in graphene, with its consequent doping. A shift upwards (downwards) means that electrons (holes) are donated by the metal to graphene overlayer which shows n-type (p-type) doping [59]. Several theoretical models were proposed to quantify this energy shift [60, 61]. Giovannetti *et al.* [62, 63], for example, developed a phe-

nomenological model, treating the graphene-metal interface as a capacitor (see Figure 3.3a). The electron transfer at the interface, in fact, steers to the charge redistribution and to the formation of a dipole layer.

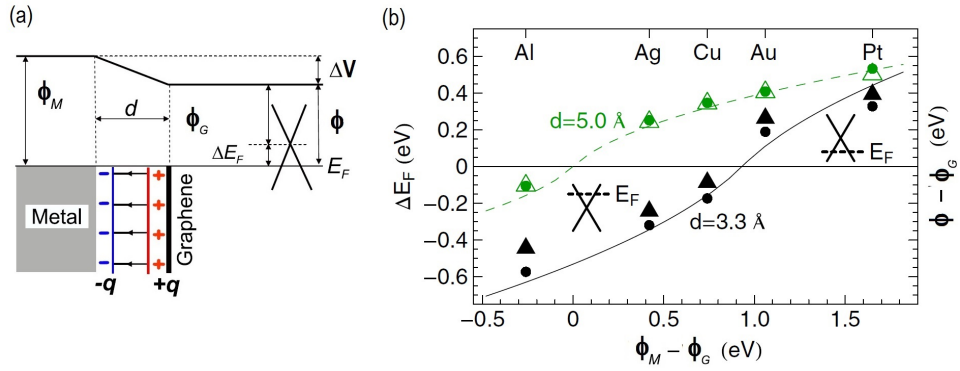

Figure 3.3: (a) Schematic illustration of the model used for the interface dipole in the case of electron transfer from graphene to metal. (b) Calculated Fermi energy shift with respect to graphene conical point, ΔE_F (dots), and change in the work function $\Phi - \Phi_G$(triangles) as a function of the difference between bare metal and graphene work function $\Phi_M - \Phi_G$. The shift ΔE_F has been calculated both at the equilibrium separation of graphene layer from metal surface, i.e. 3.3 Å (black) and at larger distance, i.e. 5 Å (in green). Adapted from [62].

The work function of the graphene/metal interface is given by $\Phi(d) = \Phi_M - \Delta V(D)$, where the potential step ΔV is modeling in order to take into account both the electron transfer contribution Δ_{tr}, associated to the work functions difference, and the contribution Δ_c resulting from a metal-graphene chemical interaction (i.e. $\Delta V = \Delta_{tr}(d) + \Delta_c(d)$). In this approximation the change of the Fermi energy ΔE_F associated to the work function difference between the metal and the graphene overlayer is:

$$\Delta E_F(d) = \pm \frac{\sqrt{1 + 2\alpha D_0(d - d_0)|\Phi_M - \Phi_G - \Delta_c(d)|}}{\alpha D_0(d - d_0)} - 1, \qquad (3.4)$$

where the sign of ΔE_F is given by the term $|\Phi_M - \Phi_G - \Delta_c(d)|$, $(d - d_0 = Z_d)$ is the effective distance between the charge sheets on graphene and on metal

and the parameter αD_0 includes the properties of graphene (i.e. $\alpha = e^2/\epsilon_0 A$, with A=5.18 (Å)^2 the area of the graphene unit cell, and $D(E) = D_0|E|$, with $D_0 = 0.09$ per eV^2 unit cell). The calculated Fermi level shifts, ΔE_F, with respect to the graphene conical points at the equilibrium ($d \sim 3.3$ Å) and at larger graphene-metal separation ($d \sim 5$ Å) for different metal substrates are shown in Figure 3.3b. The solid and dashed lines, deriving from the model of eq. 3.4, interpolate well the DFT results, confirming the accuracy of the model.

Interface states at graphene/metal interface

Interface electronic states at graphene on a variety of metal surfaces have been extensevely studied in last years both theoretically [64,65] and experimentally [48, 57, 66]. Due to the two-dimensional (2D) character of free-standing graphene the occurrence of IPS series on both sides of the layer at the center of the Brillouin Zone was predicted by ab-initio band structure calculations, using a hybrid potential, i.e. local density (LDA) calculation for the description of the short-range properties and an image potential tail for the description of the long-range properties [67]. This theoretical model hypothesizes that the wave functions associated to each of the two IPS series have opposite parity with respect to the reflection plane of graphene sheet. The states with a symmetric wave function, n^+, show a lower energy and they are bound more strongly because of their localization closer to the graphene layer compared with the antisymmetric states, n^-. When graphene is deposited onto a substrate, the mirror symmetry with respect to the graphene sheet is broken and the double-series of IPS evolve into a single series of mixed states. Therefore it is more appropriate a classification of hybridized graphene/metal states into states preferentially located between the graphene layer and the substrate or at graphene/vacuum interface [59]. Several different model potentials have been developed for the description of graphene/metal systems. The most widely used combine a realistic description of the projected metal band gap (e.g. the well-established 1D analytical potential introduced by Chulkov *et al.* [68]), the image-potential of the metal, and the potential of the graphene layer for an arbitrary graphene-metal distance [65]. Frequentely the potential due to the graphene layer is modeled by the hybrid potential "LDA+image tail" developed by Silkin *et al.* [67] for the description of freestanding graphene or by a potential barrier (δ-function) in correspondence with the graphene plane, plus two potential wells on both

sides of the graphene [69].

In addition to the theoretical calculations, several two-photon photoemission studies have been carried out at graphene on various metal surfaces both weakly and strongly interacting [48, 57, 66]. The best-investigated interface for the weakly interacting systems is represented by Graphene/Ir(111) interface. In fact, it is known that graphene overlayer forms almost defect-free single-crystal domains [46, 70] with a long-range ordered moiré with a corrugation of only ∼0.37 Å [71], while graphene grown on other weakly interacting metals, e.g. Pt(111) or Cu(111), shows a great variety of rotated domains.
Results of angle-resolved and time-resolved two-photon photoemission experiments on graphene/Ir(111) for the observed unoccupied interface states are shown in Figure 3.4 [66]. Three unoccupied states with effective masses close to the free-electron mass and with binding energies of 0.83 eV, 0.19 eV and 0.09 eV with respect to the vacuum level at the $\bar{\Gamma}$ point have been observed. Moreover, from the time-resolved measurements, lifetimes of tens to hundreds of femtoseconds are obtained. Thus, from these observations, Niesner *et al.* ascribed such states to the series of image potential states which occur in front of metallic surfaces, i.e. Ir(111) specifically. The almost identical binding energies of the IPS after the graphene growth may be due to the presence of an image-charge screened mainly within the graphene layer, confirming that the substrate is not significantly affected by the presence of graphene in a weakly coupled system. The only effect was a slight upshift of Ir(111) surface state of ∼0.2 eV, according with a charge transfer process between the substrate and the graphene overlayer [54]. Similarly, a small energy shift of the substrate surface states, at the weakly counpled interfaces, were also observed for graphene/Au/Ni(111), graphene/Au/Ir(111) and graphene/Pt(111) [57].

In contrast, at strongly interacting systems, where graphitic adlayer is chemisorbed on metal surface, such as graphene/Ni(111), the interface states are significantly shifted in energy.
A particular case worthy of attention is represented by graphene on ruthenium due to the presence of areas of both strongly and weakly interacting graphene in a periodic array. Due to the relatively strong geometrical corrugation of the graphene sheet, in fact, the C-Ru distance varies significantly from valleys (low areas, L), where has a minimum binding distance of 2.1 Å and hills (high areas, H) where the distance reaches a maximum of more than 3.5 Å [72, 73].

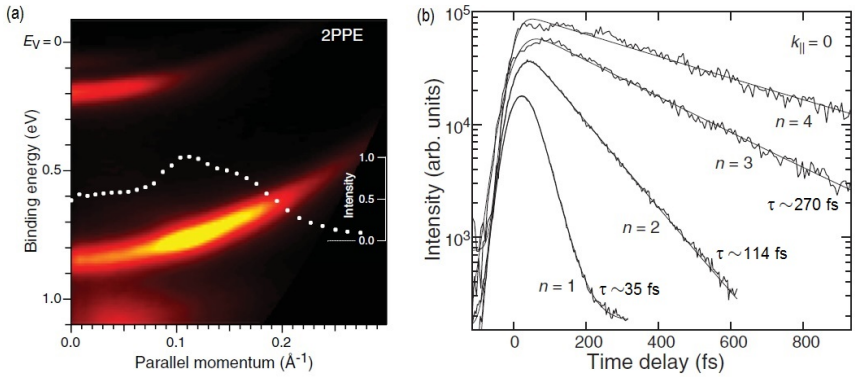

Figure 3.4: (a) Angle-resolved 2PPE measurements recorded with photon energy $h\nu$ = 1.59 eV for 1-ML graphene on Ir(111). Points represent the intensity of the lowest $n = 1$ band. (b) Time-Resolved 2PPE spectra of the IPS at $k_{||} = 0$ and corresponding lifetimes. Adapted from [66].

Graphene/Ru(0001) interface has been studied both by means of scanning-tunnelling spectroscopy (STS) [64, 69] and of 2PPE [48]. 2PPE experiments performed at graphene/Ru(0001) by Armbrust *et al.* prove the existence of five dispersing unoccupied states with lifetimes ranging from 10 up to 85 fs. Two of these states (S and S' at about 2.58 eV and 0.91 eV above the Fermi energy, respectively) arise from surface resonance of bare Ru(0001), which, depending on the graphene-Ru distance, experience distinct energy upshifts: in the H areas S', due to the larger graphene to Ru distance, is subject to a much weaker upshift than S in the L areas. The other three states close to the vacuum level have been identified as image potential-derived states. Due to their coupling to the metal substrate in the perpendicular direction, as well as their mobility in the plane parallel to the surface, IPS are strongly affected by the corrugated graphene layer [59]. The first IPS, indeed, in the high areas ($n = 1'$) shows an almost flat dispersion and it is energetically localized at about 3.44 eV above Fermi energy, while in the low areas the $n = 1$ at 3.59 eV is more delocalized with an effective mass of $\sim$0.8 m_e, as shown in the graph of energy versus parallel momentum of Figure 3.5. The energetic splitting of $n = 2$ states, instead,

is too smaller to be experimentally detected.

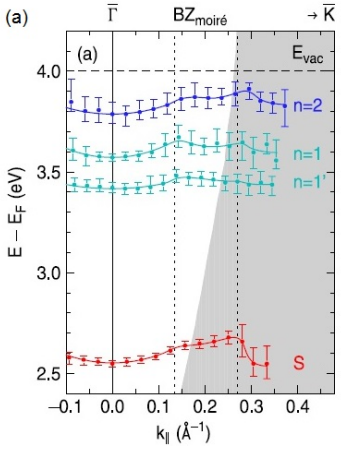

(b)

State	$E - E_F$ (eV)	τ (fs)	m_{eff}	Area
$n = 2$	3.82 ± 0.07	85 ± 13	1.2 ± 0.6	
$n = 1$	3.59 ± 0.05	16 ± 5	0.8 ± 0.3	*L*
$n = 1'$	3.44 ± 0.05	11 ± 8	2.1 ± 0.8	*H*
S	2.58 ± 0.04	10 ± 12	1.0 ± 0.2	*L*
S'	0.91 ± 0.06	22 ± 5		*H*

Figure 3.5: (a) Energy position vs parallel momentum ($k_{||}$) for the interface states at graphene/Ru(0001), distinguished between the areas of the valleys (L) and of the hills (H). (b) Table summarizing the energies $E - E_F$, lifetimes τ and effective masses m_{eff} of image potential states $n = 1; n = 1'; n = 2$ and surface states S and S' of graphene/Ru(0001) interface. Taken from [48].

3.2.2 Organic-molecules/Metal interfaces

Photo-induced electronic excitations at organic molecules-metal interfaces are of paramount interest in many chemical and physical research fields, such as photo-catalysis [74], surface photochemistry [36,75], organic-based solar cells [76] and optoelectronic devices [77]. In order to realize these organic-molecules based devices a comprehensive understanding of the electronic dynamics which characterizes such interfaces is mandatory.

Similarly to the classification introduced for the graphene/metal interface, it is usual to distinguish the molecules-metal coupling according to the intensity of the molecule/surface bond. Physisorption of molecules on metal substrate occurs via van der Waals forces and the molecular orbitals hybridize only slightly with the metal. In contrast, we talk about chemisorption when adsorbates interact significantly with substrate and the molecules-metal bond involves significant sharing of electrons [78]. In particular, according to the Newns-Anderson model [79], if the molecule-metal interaction energy is smaller than the width of the metal band, i.e. weak chemisorption with *sp*-band metal, the adsorbate level is broadened into a resonance centered around the original energy of the molecular orbital (Lorentzian curve centered around ϵ_a in Figure 3.6(a)). On the contrary, in the case of strong chemisorption, i.e. the molecule-metal interaction energy is larger than the metal bandwidth (e.g. *d*-band in transition and noble metals), the molecular state splits into a bonding and an antibonding state (Figure 3.6(b)).

Until now we have discussed the interaction of molecules with metal substrates in the absence of a radiation field, but in order to investigate photo-induced electronic processes at the interface it is necessary taken into account the interaction of the system with the light. A simple illustration of a generic molecules/metal interface, interacting among light, is shown is Figure 3.7. Under the influence of a radiation beam, the molecular electronic levels ($|1\rangle$ and $|2\rangle$ in Figure 3.7) may interact with the continuum of states ($|k\rangle$) in the metal [80].

The physics involved in such an interface is quite complicate and it can be summarized from the following Hamiltonian [80]:

$$H = H_0 + V = (H_M + H_S + H_R) + (V_{ET} + V_{DC} + V_{PM} + V_{PS} + V_{PMS}) \quad (3.5)$$

where the term H_0 takes into account the contributes from the Hamiltonians of the isolated molecule (H_M), metal substrate (H_S) and radiation field (H_R).

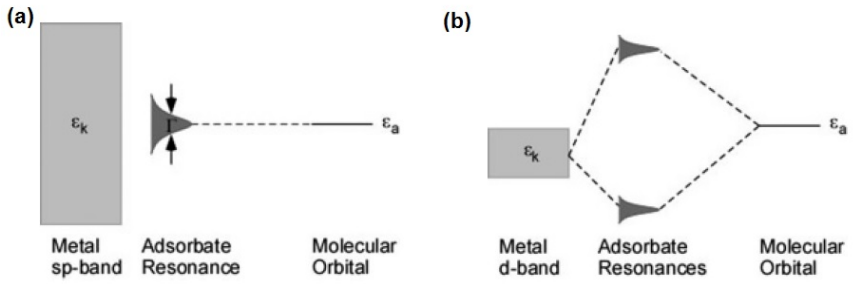

Figure 3.6: (a) Schematic representation of weak chemisorption between a molecular orbital ϵ_a and *sp*-band metal. The adsorbate level, resulting from the projected density of mixed states onto the original level, has a Lorentzian shape. (b) Schematic representation of strong chemisorption between a molecular orbital ϵ_a and *d*-band metal. The adsorbate level is splitted into a bonding and an antibonding molecular state.

V is the coupling term and contains all the interactions which characterize the interface: the electron-transfer coupling V_{ET} between the discrete molecular states and the metal continuum of states, the dipole/induced-dipole coupling V_{DC}, the molecule-radiation V_{PM} and metal-radiation V_{PS} interactions and the molecule-substrate-radiation field coupling (V_{PMS}), that is the photo-excited direct transition between the electronic continuum of the metal and a discrete molecule state.
Recently several two-photon photoemission experiments at different molecule-metal interfaces have been carried out in order to shed light on the dominant mechanisms in photo-induced electron transfer and on the possible establishment of new metal/molecule hybrid states, representing potential new channels of charge transfer at the interface [43, 81–83]. Such experimental studies allow to probe the photo-induced electron transfer at molecule-metal junction V_{PMS} and the rate of electron transfer between a photo-excited substrate and the molecule (or vice versa) V_{ET} . However, despite the large number of works available and the consolidated theory, the specific evaluation of photo-induced charge transfer at individual systems finds two large obstacles: the extended nature and reduced symmetry at the molecule-metal and the difficulty in dealing with excited electronic states [80].

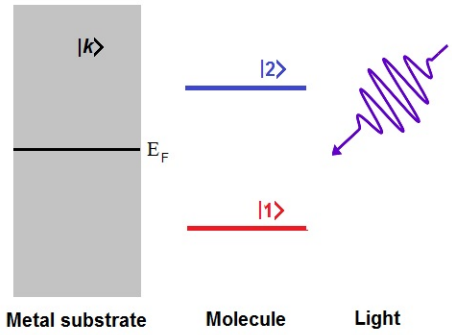

Figure 3.7: Schematic illustration of a generic molecules/metal interface interacting among light.

In order to understand the photo-induced charge transfer processes at the interface, it is customary to distinguish in direct and indirect mechanisms. In a direct process an electron from the continuum of state or from a discrete surface state is directly photo-excited in an unoccupied molecular state, e.g. the LUMO orbital (as shown in Figure 3.8). Such direct processes can be described using the matrix elements of V_{PMS}.

The rate of electron injection from the metal state $|k\rangle$ to the molecular orbital $|2\rangle$ (R_{k2}) can be written as:

$$R_{k2} \propto |\langle 2|\vec{\mu}|k\rangle \cdot \vec{E}|^2 \delta(E_2 - E_k - h\nu) = |M_{k2}|^2 \delta(E_2 - E_k - h\nu) \tag{3.6}$$

where μ is the transition dipole operator and **E** is the electric field vector. Equation 3.6 can be easily generalized to the case of bulk metal states, i.e. multiple initial states non-interacting:

$$T_2 = \sum_k R_{k2} = \sum_k \left[|M_{k2}|^2 \delta(E_2 - E_k - h\nu)\right] \tag{3.7}$$

where T_2 is the total injection rate into state $|2\rangle$. Although until now we have discussed only the case of metal-to-molecule electron transfer, the considerations above can be extended to photo-induced molecule-to-metal electron transfer, considering the transitions between an initial occupied molecule state,

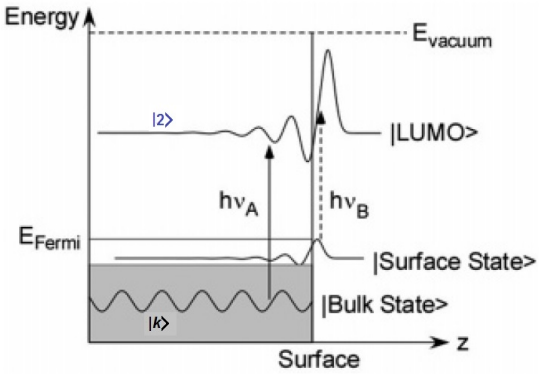

Figure 3.8: Schematic illustration of a direct excitation process from bulk states or from surface states to an unoccupied molecular orbital, e.g. LUMO. A third transfer channel from an occupied molecular orbital is possible, but it does not represent charge transfer from substrate. Taken from [80].

e.g. HOMO, and unoccupied metal states.
The second possible mechanism in photo-induced interfacial charge transfer is represented by indirect ET process. This mechanism is characterized by two independent steps: an initial photoexcitation of the molecule or of the substrate and the proper charge transfer at the interface. If the initial excitation is in the molecule (V_{PM}), the excited electron in the unoccupied molecular orbital $|2\rangle$ can rapidly decay into one of the unoccupied states of the substrate, while, if the excitation occurs in the metal (V_{PS}), most of the time, the charge transfer is mediated through the so-called hot electrons. As shown in Figure 3.9, the absorption of a laser pulse by the metal substrate generates hot electrons distribution in the bulk. These electrons can travel to the surface and scatter into an adsorbate empty state/resonance. In the same way, a hot hole in the substrate can attach to an occupied molecular state/resonance [80].

Another probable indirect process for populating excited states at the molecule-metal interface involves the excitation of an electron into a higher excited state or one of the same energy, followed by scattering into the unoccupied state of interest. Both intraband scattering in molecular states and interband decay processes from higher-lying to lower-lying molecular states have been observed

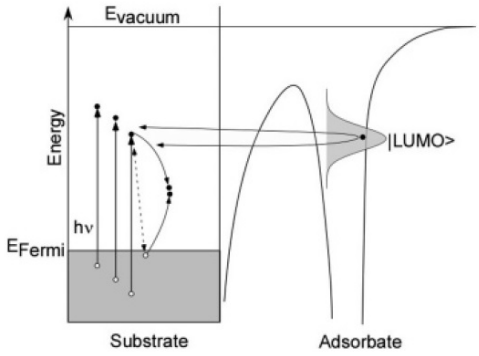

Figure 3.9: Schematic illustration of an indirect excitation process represented by an hot electrons transfer into an unoccupied molecular resonance at the surface, e.g. LUMO. Taken from [80].

by means of angle- and time-resolved 2PPE [84]. Finally, Rous *et al.* [85] first proved the possibility of image potential state assisted tunneling of hot electrons from the bulk to an excited molecular state.

Chapter 4

Interface states at the single-layer Graphene/Cu systems

Single-layer graphene supported on a metal surface has shown remarkable properties relevant for novel electronic and optoelectronic devices. However, the nature of the electronic states derived from unoccupied surface states and quantum well states, lying in the real-space gap between the graphene and the solid surface, has not been explored and exploited yet. In this chapter, we report the ultraviolet non-linear angle-resolved photoemission spectroscopy studies performed to unveil the coexistence at the graphene/Cu(111) interface of a highest occupied Shockley surface state (HOSS) and the two lowest unoccupied surface states (LUSS). Moreover, by tuning the laser photon energy, two resonances, corresponding with direct optical transitions between HOSS and the two unoccupied states have been detected. The experimental results and the electronic structure calculations, based on one-dimensional model potential, indicate that the two unoccupied states originate from the hybridization of the $n = 1$ image potential state with a quantum well state. The hybridized nature of these unoccupied states is benchmarked by a similar experiment done on single-layer graphene grown on copper polycrystalline foil where only the image state survives being the quantum well state at this interface inhibited.

4.1 Introduction

Graphene/metal interfaces have been the subject of extensive studies to understand the substrate-induced perturbation on the graphene electronic structure, in particular in the vicinity of the Dirac cone. As shown in the previous chapter, when graphene weakly interacts with a crystalline metal support, e.g. Ir and Cu, the π band is almost unperturbed and the Dirac cone located at K-point is still well defined, while a small doping effect slightly shifts the Fermi level. Recently many studies regarding a comprehensive understanding of the nature and the character of the occupied states at the weakly coupled graphene/metal interfaces, have been carried out [44,53,54]. However, the unoccupied electronic states and, in particular, the nature of the image potential states (IPS) in these systems are still unclear.
Graphene/Cu(111) is a prototypical example of weakly interacting system where a single layer graphene grows forming different domains with a low corrugation and with several azimuthal orientations, nevertheless the average graphene-Cu distance is the same for all domains and comparable to the graphene distance in graphite, e.i. about 3.3 Å [44]. Therefore, similarly to graphene/Ir(111) [66], a single series of IPS, unmodified by the presence of graphene, is expected.

In this chapter the non-linear photoemission measurements performed at the single-layer graphene/Cu(111) interface and at single-layer graphene grown on polycrystalline copper (graphene/Cu-poly) are reported. In addition to the angle-resolved experiments carried out in order to unveil the nature of the surface states observed at these interfaces, 2PPE measurements by tuning the laser photon energy have been performed, in order to explore possible resonances. On (111) oriented surfaces of noble metals, indeed, both an occupied surface state, just below to the Fermi level, and unoccupied IPS, few hundreds of meV below the vacuum level, exist at the center of the Brillouin zone. Thus, it is reasonable to assume a direct population of the unoccupied states from SS.
The achieved results at graphene/Cu(111) interface are strengthened by *ab-initio* electronic structure calculations.

4.2 Samples preparation and characterization

Graphene was grown on a Cu(111) single crystal (MaTeck GmbH) that was previously Ar-sputtered (1 keV) and annealed (650 K) in ultrahigh vacuum. The crystal was then transferred (through air) into a vacuum furnace (base pressure 10^{-5} mbar), where it was reduced in a mixture of 0.5 mbar of hydrogen (Messer, purity 5.0) and 0.1 mbar of argon (Linde, purity 5.0) for 4 h at a temperature of 1250 K for 2 h before graphene was grown by exposure to a mixture of argon (0.1 mbar), hydrogen (0.5 mbar), and methane (0.5 mbar, Messer, purity 4.0) for 2 min while the substrate was kept at 1250 K. Graphene was subsequently cooled to room temperature in an argon flow (0.09 mbar) at a rate of 15 K/min. The Cu foil (thickness 25 μm, 99.999 % purity, ESPI Metals) was pre-etched in a 0.25 M solution of H_2SO_4 in water for 5 min, rinsed in water and ethanol, dried in an argon flow and transferred to the vacuum furnace. The foil was then reduced in H_2 and Ar for 1 h at the same temperature and pressure employed for Cu(111), while the growth of graphene followed the same protocol described above for the growth on Cu(111).

To characterize the graphene layer, Raman measurements were carried out with a Renishaw inVia μ-Raman, equipped with a 633 nm He-Ne CW laser. The resulting spectrum is shown in Figure 4.1a, together with a spectrum acquired on HOPG for comparison.
We identified three main peaks at 1336, 1586, and 2670 cm^{-1}, labeled D, G, and G$'$, respectively. The G and G$'$ peaks are characteristic of a graphitic layer [86]. The G$'$ could be fitted with a single Lorentzian peak (width = 49 ± 7 cm^{-1}), indicating that a single layer of graphene is grown on the copper surface [87]. Collecting maps of 40×40 μm^2, no evidence of domains with two or more or without graphene layers emerges from the μ-Raman spectra of graphene/Cu(111). The presence of a D peak with an intensity comparable to the G peak suggests the presence of grain boundaries and defects in the layer [88]. Moreover,the Raman energy shift of the G mode, benchmarked with free standing graphene, suggests that the graphene layer is n-doped with the Fermi level downward shifted of about 200 meV, in agreement with a single-layer graphene-Cu(111) distance of $\sim$3.2 Å [62, 89].

A low-energy electron diffraction pattern (Figure 4.1b) collected on graphene/Cu(111) shows the hexagonal first-order spots of Cu(111) (surface lattice

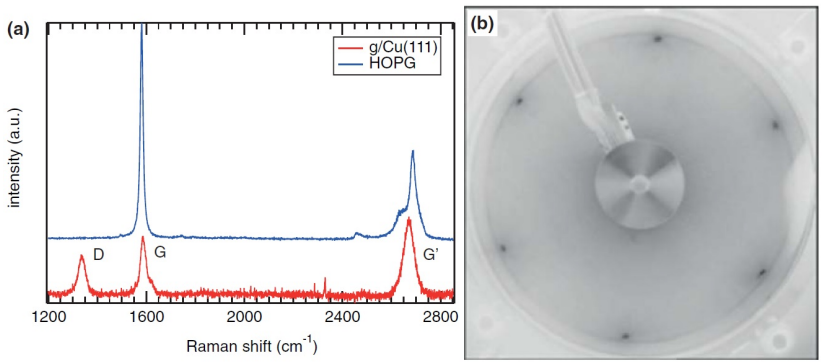

Figure 4.1: (a) Representative Raman spectrum of graphene/Cu(111) and of HOPG. The relevant peaks of the graphene spectrum are marked. The excitation wavelength employed was $\lambda = 633$ nm. (b) Low-energy electron diffraction pattern of graphene/Cu(111) collected with a primary beam energy of 80 eV.

parameter 2.55 Å) and a ring pattern, for which the corresponding lattice parameter matches that of graphene (2.46 Å). Therefore the graphene crystalline domains do not exhibit any preferential orientation.

The crystalline orientation of the copper foil substrate was checked by electron-back-scattering diffraction. Crystalline domains with sizes ranging from 100 to 1000 μm with a dominant crystalline orientation close to (001) were observed (see Figure 4.2).

4.3 Experimental results

4.3.1 Graphene/Cu(111) interface

The 2PPE spectrum of the single-layer graphene/Cu(111), acquired with p-polarized light and with photon energy $h\nu = 4.10$ eV, is shown in Figure 4.3b. The laser photon energy has been tuned to select $h\nu = 4.10$ eV and to unambiguously reveal the emissions originating from the occupied and unoccupied states in the energy region around the Fermi energy, E_F (Figure 4.3). The d-band of Cu(111) was identified at about $E - E_{\mathrm{F}} = 6$ eV and the work function

Figure 4.2: (a) Electron back scattering diffraction map acquired on a graphene grown on Cu foil sample. (b) Orientation distribution of the image reported in (a). The dominant crystalline orientation is (001).

results 4.1±0.1 eV. Moreover, three features were observed and labeled as lowest unoccupied surface states, LUSS1 (7.3 eV) and LUSS2 (7.7 eV), and highest occupied surface state, HOSS (8.0 eV). Notably, these emissions are quenched when the laser beam was *s*-polarized (see Figure 4.3c). This finding is consistent with the electric dipole selection rules for surface states [30, 90].

Figure 4.4a shows the linear emission from the surface occupied states as measured with a photon energy of 6.28 eV. As expected, only the Cu(111) occupied Shockley surface state was observed as a distinct peak at $\sim$ 0.2 eV just below the Fermi level. This spectral feature is helpful to unambiguously identify the HOSS emission, detected in the 2PPE spectrum (see Figure 4.3), as the Cu(111) Shockley surface state. The shift of the HOSS binding energy with respect to clean Cu(111) is consistent with that measured in conventional angle-resolved photoemission experiments [91–93] and is assigned to a charge-transfer process induced by the different work functions between the graphene layer and the metal surface. This assignment matches also with previous results reported for graphene/Ir(111) [57,66], where an unquenched Shockley state was observed due to the large adsorption distance ($\sim$ 3.4 Å) between metal and graphene. The energy dispersion $E(k_{\parallel})$ for the HOSS state, measured in linear ARPES is reported in Figure 4.4b. The HOSS effective mass derived from the

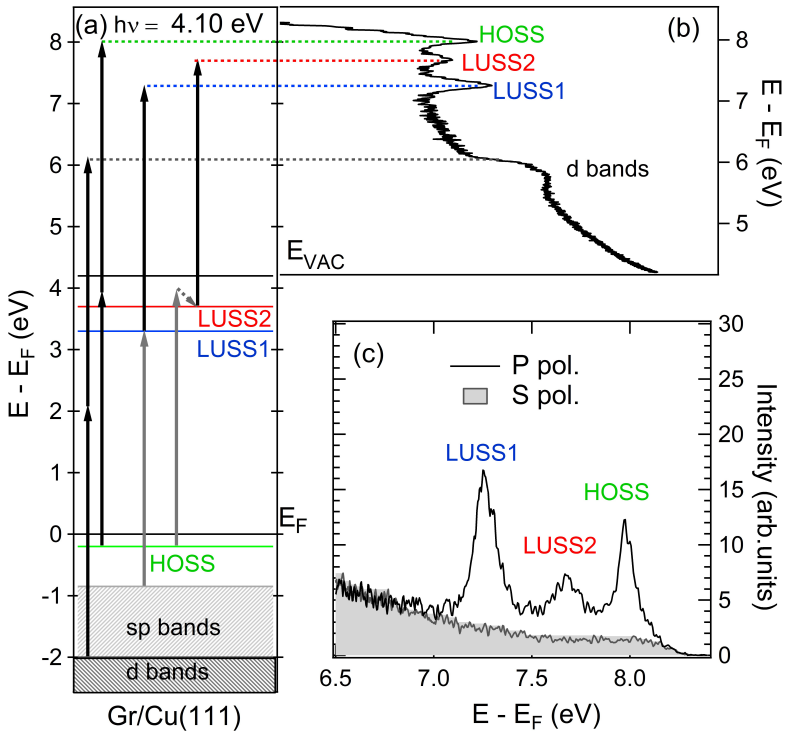

Figure 4.3: (a) Photoemission processes (arrows) from the Cu $d-$band and from the surface states (HOSS, LUSS1, LUSS2, see text) at the single-layer graphene/Cu(111) interface. (b) Non-linear photoemission spectrum acquired at normal emission ($k_{\|} = 0$) and with a photon energy of 4.10 eV. (c) The HOSS, LUSS1, and LUSS2 emissions, observed with p-polarized light, are completely quenched in the spectrum acquired with s-polarized light (light grey spectrum).

fitting of the $E(k_{\|})$ data with a parabolic function, was found to be $m^* = 0.45 \pm 0.05\ m_e$, being m_e the free electron mass. This value is consistent with the value of $0.47 \pm 0.04\ m_e$ measured for the Shockley surface state on clean Cu(111) [86, 94, 95].

Moreover, the intrinsic line-width at $k_{\|} = 0$ (70 ± 5 meV), obtained by fitting

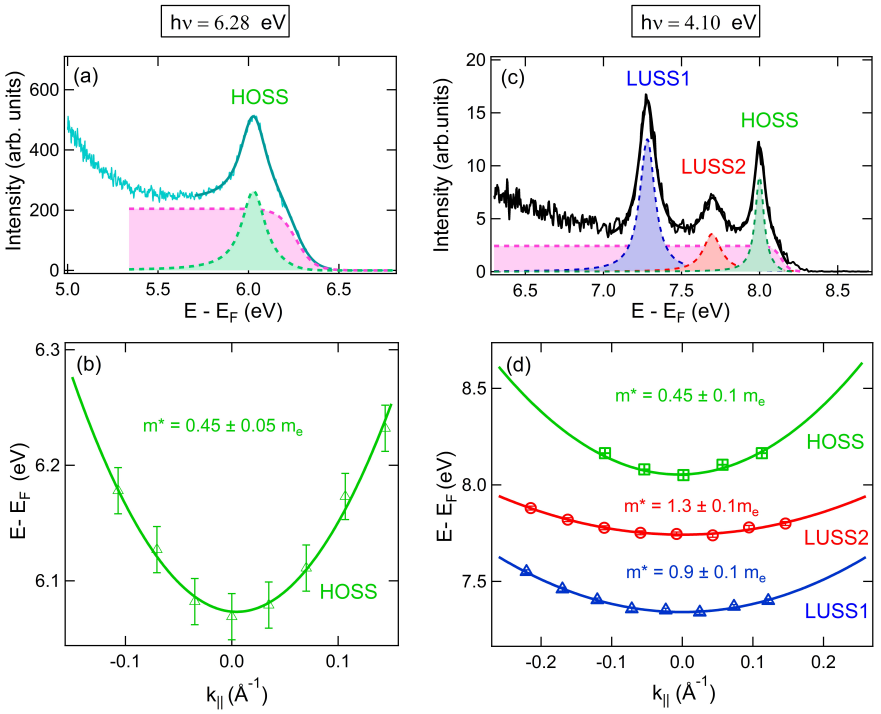

Figure 4.4: (a) Linear photoemission spectrum collected at normal emission ($k_{\|} = 0$) with a photon energy of 6.28 eV and p-polarized light at the single-layer graphene/Cu(111) interface. (b) Energy position versus $k_{\|}$-momentum for the Shockley surface state collected at $h\nu = 6.28$ eV. A parabolic fit (line) gives an effective mass of 0.45 ± 0.05 m_e. (c) Single-layer graphene/Cu(111) non-linear photoemission spectra collected at normal emission ($k_{\|} = 0$) in p- polarization and with a photon energy of 4.1 eV. The three structures observed are well interpolated by three Lorentzian curves and a Fermi-Dirac function (pink dashed line) convoluted with a Gaussian broadening accounting for the experimental resolution (35 meV). (d) Energy position versus $k_{\|}$-momentum for the Shockley surface state (HOSS) and for LUSS1 and LUSS2 interface states collected at $h\nu = 4.10$ eV. The parabolic fit (line) of the data gives the effective masses reported in the figure for each state.

the HOSS with a Lorentzian function convoluted with a Gaussian, accounting for the experimental resolution (35 meV), was found to be consistent with the value measured on the clean metal (60 ± 10 meV) [90, 91].
Considering the linear photoemission spectrum reported in Figure 4.4a, we tentatively assign the LUSS1 and LUSS2 emissions in Figure 4.4c to the unoccupied states of the single-layer graphene/Cu(111). The binding energies (with respect to the vacuum level) of LUSS1 and LUSS2 are 0.90 ± 0.05 eV and 0.50 ± 0.05 eV, respectively, while their intrinsic line-widths at $k_{\parallel} = 0$ are 115 ± 5 meV and 140 ± 5 meV, respectively. The multi-photonic order (MPO) measured from the non-linear photoemission spectra collected at $h\nu = 4.10$ eV and $k_{\parallel} = 0$, is MPO=2. This is the value expected for a second order non-linear photoemission process where the first photon transiently populates the LUSS1 and LUSS2 states, while a second photon is providing the energy for the electron emission. The effective masses of LUSS1 and LUSS2, evaluated from non-linear ARPES at $h\nu = 4.10$ eV, were found to be $m^*_{\mathrm{LUSS1}} = 0.9 \pm 0.1\ m_{\mathrm{e}}$ and $m^*_{\mathrm{LUSS2}} = 1.3 \pm 0.1\ m_{\mathrm{e}}$ (see Figure 4.4d). Instead, the HOSS effective mass measured at $h\nu = 4.10$ eV matches the value obtained by linear ARPES reported in Figure 4.4b.

In addition to angle-resolved 2PPE, we performed also non-linear photoemission at different energies by tuning the incident photon energy across the HOSS $\rightarrow$ LUSS1, HOSS $\rightarrow$ LUSS2 transitions, i.e. from 3.2 eV to 4.1 eV. As shown in Figure 4.5a, a strong increase of the photoemission intensity of the LUSS1 feature (about fifty times) is observed when the photon energy is resonant with the HOSS $\rightarrow$ LUSS1 optical transition at ≈ 3.5 eV. This value is confirmed by the shift of the HOSS and LUSS1 energy positions using different photon energies as reported in Figure 4.5b. In the case of coherent 2PPE from an occupied state, the energy shifts twice as much as the change of photon energy ($\Delta E = 2\Delta h\nu$), while, in the case of one-photon photoemission from a state transiently populated, the dependence of the binding energy of the LUSS1 versus $h\nu$ is linear ($\Delta E = \Delta h\nu$). The crossing point on the graph corresponds to the energy of the HOSS $\rightarrow$ LUSS1 optical transition. A second resonance, less intense, appears at 3.85 eV, when the photon energy is resonating with the HOSS $\rightarrow$ LUSS2 optical transition. This result suggests that a weak dipole optical transition is allowed between these two states.

Figure 4.5c shows the LUSS1 photoemission intensity as a function of the photon energy. The shape of the resonance is symmetric and it is well fitted by a

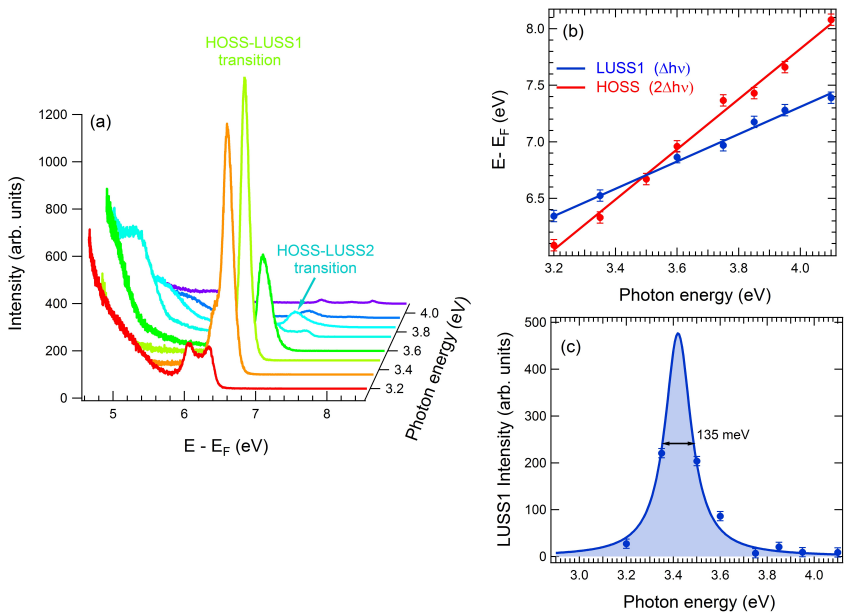

Figure 4.5: (a) 2PPE spectra measured at the graphene/Cu(111) interface by tuning the photon energy across the HOSS → LUSS1 transition, i.e. from 3.2 eV to 4.1 eV, at normal emission ($k_{||} = 0$) and with p-polarized light. (b) Energy position of the LUSS1 and HOSS emissions versus the incident photon energy. The crossing point (∼3.5 eV) corresponds to the HOSS → LUSS1 optical transition energy. (c) LUSS1 photoemission intensity versus the photon energy. The shape of the resonance results well fitted by a symmetric Lorentzian curve.

Lorentzian function, i.e. with a Fano function with a very large asymmetry parameter (q-value) [96–99]. A symmetric Lorentzian lineshape is one of the most ubiquitous spectral features and it is the typical signature of an exponentially decaying state with a finite lifetime. Whereas, an asymmetric Fano function emerges when discrete excited states are coupled to a continuum of states. In

his original paper, Fano [97] introduced the asymmetry parameter, q, as the ratio of the transition probabilities to the discrete state and to the continuum. When the transition to the continuum is weak, q becomes large, and the absorption process is entirely dominated by the transition between discrete states and the process becomes dominantly Lorentzian. In our experiment, the HOSS $\rightarrow$ LUSS1 lineshape resonance appears as a symmetric Lorentzian profile. This result is in principle not obvious because both LUSS1 and HOSS wave functions penetrate into the bulk metal, favouring elastic and inelastic scattering processes between electrons in LUSS1 and in the continuum of the bulk states [35]. In this framework, the symmetric character of the resonance measured in our experiment is indicative of a weak interaction between the surface states and the continuum of states of the metal [98, 99].
In order to shed light on the nature of the unoccupied states observed at graphene/Cu(111), 2PPE measurements have been performed on single-layer graphene grown on copper polycrystalline foil together with an electronic structure calculations.

4.3.2 Graphene/polycrystalline-Cu interface

Figure 4.6 shows non-linear photoemission spectra (hν=4.10 eV) measured on the single-layer graphene on the Cu foil and on clean Cu foil. On the clean Cu foil we detected only the emission originating from the Cu *d* band along with a clear Fermi edge. The presence of a continuum of states at the Fermi level without any energy gap in the integrated projected band structure of the Cu foil hinders, as expected, the formation of image states. Conversely, on single-layer graphene/Cu-poly, beside the *d* band and the Fermi edge, an additional feature is clearly detected. This state exhibits a surface-state symmetry, vanishing with *s*-polarized light and an effective mass consistent with the free-electron mass as shown in the inset of Figure 4.6.

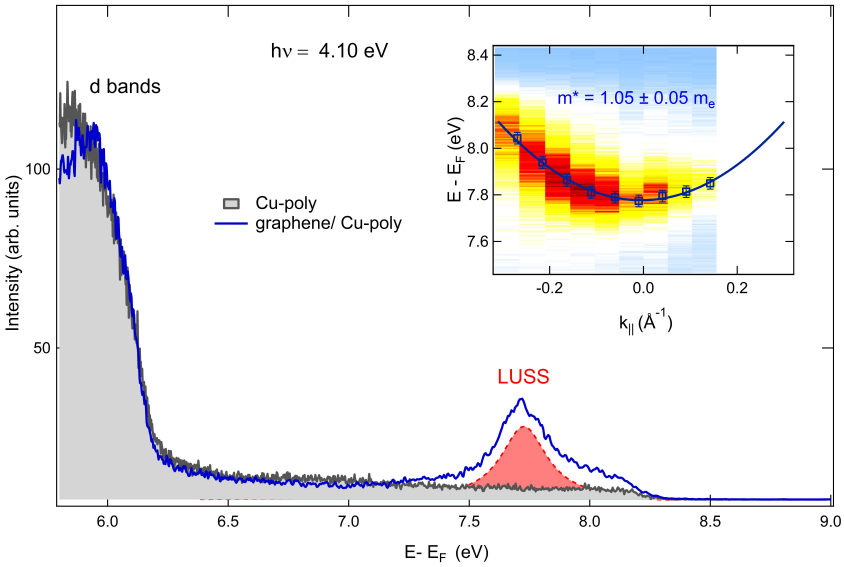

Figure 4.6: Comparison between non-linear photoemission spectra measured at $k_{\|} = 0$ using p-polarized laser pulses at hν=4.10 eV on graphene grown on polycrystalline Cu foil and on clean Cu foil. The emission measured from the single-layer graphene on the Cu foil detected in the 7.0 eV- 8.5 eV $E-E_F$ energy region is well fitted by a single Lorentzian and a Fermi-Dirac function. The inset shows the single-layer graphene/Cu-poly foil LUSS band dispersion. The effective mass for this state is deduced from the parabolic fit (solid line) of the ARPES data.

4.4 Discussion and theoretical calculations

Concerning the results obtained on graphene/Cu(111), LUSS1 can be identified to the n=1 IPS of Cu(111), being its binding energy and effective mass comparable to those of a typical first image state in front of a metal surface. Differently, the behavior of LUSS2 is unknown in literature. In principle, we can speculate that LUSS2 was the $n = 1$ state of a second series of IPS. However, this interpretation has to be excluded.
Two series of image potential states have been recently observed on the strongly interacting graphene/Ru interface [48]. In this system, however, the morpho-

logy of the graphene layer is completely different. The strong corrugation (about 1.5 Å) of the graphene layer originates two different regions (H and L region) responsible for the presence of two $n = 1$ IPS that differ in binding energy of about 150 meV. As often emphasized in literature, graphene/Cu(111) is a prototypical example of weakly interacting system where a single layer graphene grows forming different domains with several azimuthal orientations as confirmed by Raman and Low Energy Electron Diffraction measurements collected on our sample (Figure 4.1). The average graphene-Cu distance is about 3.2 Å for all domains and the maximum corrugation of a single domain is 0.35 Å [94]. The presence of two $n = 1$ image states that differ in binding energy by about 400 meV could be justified in graphene/Cu only by an important variation of the graphene-Cu distance and consequently of the local work function. From *ab-initio* calculations within the density functional theory (DFT) as implemented in the SIESTA package, we estimate that a variation of the local work function of 400 meV can be only justified by a distance variation of 1 Å, suggesting that domains with a graphene-Cu distance of about 2 Å should exist and they must be quite extended.

Two series of IPS could be originated also by a change of the charge transfer sign, from n to p [95] between the substrate and graphene. However, a significant change in charge transfer must necessarily affect the binding energy of the occupied surface state (HOSS) that in our experiment appears evermore shifted of $\sim$ 200 meV with respect to the Fermi level. This observation is based on micro-ARPES experiments performed with a lateral resolution of $\sim$1 μm [100]. These measurements have shown that the binding energy of HOSS does not change significantly on the whole graphene/Cu(111) surface invalidating this interpretation of the present data.

Hence, having excluded that LUSS2 was a second IPS, to clarify the nature of the LUSS1 and LUSS2 states, we performed electronic structure calculations using the one-dimensional model potential reported in Figure 4.7a. The Cu(111) surface is described by a phenomenological modulated potential, as proposed by Chulkov *et al.* [68], which is able to reproduce main surface features of the metal surface such as the experimental work function, the surface-projected energy gap, and the energy position of surface and image states.

To model the potential due to the graphene layer, we used a potential barrier in correspondence with the graphene plane, at 3.2 Å from the Cu(111) surface,

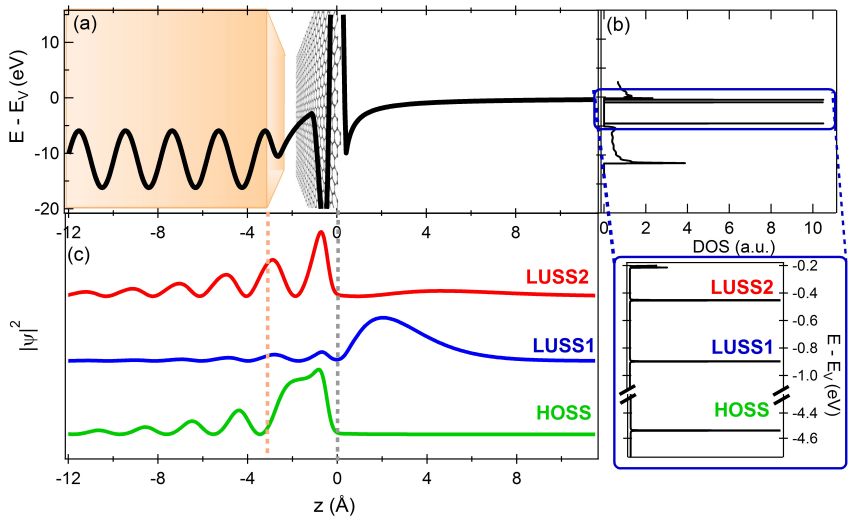

Figure 4.7: (a) One-dimensional potential used to simulate the graphene/Cu(111) interface. (b) The calculated density of states (DOS) points out the presence of three states whose binding energies are comparable with the HOSS, LUSS1, and LUSS2 binding energies measured in the two-photon photoemission spectrum of Figure 4.3. In (c) the probability amplitude of HOSS, LUSS1, and LUSS2 states is plotted.

plus two potential wells on both sides of the graphene. A similar potential has been already adopted in the literature to simulate graphene [69] because it accounts for the transmission and reflection of electronic wave functions impinging on the carbon layer. In addition our potential considers the effective barrier on the bulk side, generated by the presence of the energy L gap.

The shape of this additional potential can be chosen in different ways and for sake of computational simplicity we considered two cosine-like attractive well and a cosine-like barrier. Its analytic form in atomic units is:

$$v_{Gr}(z) = \begin{cases} A_1\{\cos[2\pi(z+\lambda_T)/\lambda_1] - 1\} & \text{for } -\lambda_T < z < -\lambda_2/2 \\ A_2\{\cos[2\pi z/\lambda_2] + 1\} - 2A_1 & \text{for } -\lambda_2/2 < z < 0.75 \end{cases} \tag{4.1}$$

where λ_1 and λ_2 are fixed to 2.25 and 2 Bohr, respectively, and $2\lambda_T$ is their

sum. A_1 and A_2 are equal to 0.43 and 1.7 Hartree, respectively.

The parameters for the graphene barrier were chosen in order to reproduce the energy levels measured by linear and non-linear photoemission. This procedure does not uniquely fix the parameters, but we found that different combinations that gave the same energy values resulted in almost equivalent surface wave functions.

The electronic structure calculations were performed using the embedding approach that allows to describe semi-infinite substrate [101,102]. The density of states reported in Figure 4.7b displays the continuous bulk states of Cu projected along the (111) direction and an energy gap; in this gap we find three states, with binding energies equal to -4.55 eV, -0.9 eV, and -0.45 eV with respect to the vacuum level, which can be identified as HOSS, LUSS1, and LUSS2, respectively (see Figure 4.7b). The probability amplitude of these states is reported in Figure 4.7c. The HOSS is mainly localized in front of the Cu(111) surface, as expected for a Shockley state. Differently, LUSS1 and LUSS2 present the character of interface states being spatially localized at the graphene/vacuum and the graphene/Cu(111) interfaces. Their proximity in energy suggests that they can be ascribed to the hybridization of two nearly degenerate levels lying in the two potential wells formed by the graphene potential barrier with the surface energy gap and the image potential, respectively. Although LUSS1 and LUSS2 display the same physical nature, the experiments revealed distinct effective masses. The difference between the value of $m^*_{\mathrm{LUSS1}} = 0.9 \pm 0.1\ m_{\mathrm{e}}$ and $m^*_{\mathrm{LUSS2}} = 1.3 \pm 0.1\ m_{\mathrm{e}}$ can be explained by the different energy positions of these states with respect to the bulk band edge. When the binding energy of an unoccupied state is close to the upper edge of the energy gap, the effective mass is affected by the deviation of the band dispersion from the free electron behavior. As explained by the multiple reflection theory approach [17], when moving along $k_{\parallel}$, this results in a different phase shift of the wave functions reflected by the barrier, represented by the energy gap. Consequently the effective height of the quantum well in which electrons are trapped changes with $k_{\parallel}$. In graphene/Cu(111), LUSS1 is sufficiently distant in energy from the band edge to account for a nearly free electron dispersion. Differently, LUSS2 is found at ~ 0.2 eV below the band edge, and this energy proximity explains the value of the effective mass $\sim 1.3\ m_{\mathrm{e}}$ within the energy gap. This value is similar to what is observed for the first IPS of the clean Cu(111) which is found close to the

bulk band edge because of the higher work function of the clean surface with respect to single-layer graphene/Cu(111) [90, 91].

This scenario is confirmed by the presence of a single image-like state (LUSS) detected on graphene/Cu-poly, while it does not appear in the Cu foil (see Figure 4.6). As previously remarked, the presence of a continuum of states at the Fermi level of the Cu foil without any energy gap in the integrated projected band structure hinders the formation of an image state in the spectrum collected on the Cu foil and similarly prevents the generation of the QWS in the real space between the foil and graphene. At the same time, graphene grown on a foil originates a potential barrier that, conversely to the case of polished Cu foil, blocks the photoemitted electrons back into the metal allowing the formation of the only image state.

4.5 Conclusions

This chapter presents a combined experimental and theoretical investigation of the occupied and unoccupied electronic surface states of a single-layer graphene on Cu(111) and on Cu-poly surfaces. At the graphene/Cu(111) interface we unveil the coexistence of a highest occupied Shockley surface state (HOSS) and two lowest unoccupied surface states (LUSS). The experimental results, obtained by ultraviolet non-linear angle-resolved photoemission spectroscopy and the electronic structure calculations, based on a one-dimensional model potential, clearly suggest that the two unoccupied states originate from the hybridization of the $n = 1$ single-layer graphene/Cu(111) image potential state with a quantum well state. This interpretation is confirmed by a similar experiment done on single-layer graphene grown on copper polycrystalline foil where only the image potential state survives being the quantum well state at this interface inhibited. Moreover, our thesis is supported also by the resonances observed tuning the incident photon energies: a strong resonant emission, i.e. about fifty times more intense than the out-of resonance emission, is detected for the HOSS $\rightarrow$ LUSS1 transition, providing a direct evidence of the high value of the matrix element integral governing this transition. The second resonance, weak but not negligible, between the Shockely state and the LUSS2 reveals the significant degree of hybridization of this state with the IPS confirming the previous theoretical predictions.

By adding important information to the present knowledge on the character of the surface states of these interfaces, we also unlock the gate for considering graphene/Cu interfaces and probably other similar systems as basic three-level devices suitable for active and passive optical processes.

Chapter 5

Surface states at the single-layer Graphene/Ir(111) interface

Single-layer graphene grown on Ir(111) surface appears as an almost free-standing ordered sheet, due to its weak interaction with the metallic substrate. As a consequence, it is expected that the characteristic Dirac cones of the graphene overlayer as well as the Rashba-type spin-polarized electronic states of Ir(111) remain mainly unchanged. Moreover, epitaxial graphene decreases the large work function of Ir(111) allowing us to efficiently populate, with photons of energies in the near ultraviolet region, the $n = 1$ image potential state.
In this chapter we report a detailed ultraviolet 2PPE study of the electronic properties and dynamics of the $n = 1$ IPS. By using circularly polarized femtosecond laser pulses we show experimental evidence of a Rashba-type spin splitting of the $n = 1$ IPS, while the lifetime of the first image potential state has been investigated by time-resolved photoemission measurements. Moreover, by tuning the pump photon energy, we compare the depopulation time of the $n = 1$ IPS populated in- and out-of-resonance from the surface state. The measured depopulation time and the IPS intrinsic line-width are discussed and successfully modeled employing the optical Bloch equations for a two levels system.

Due to the great variety of the reported results and topics, the chapter has been divided into two sections. The former is focused on the investigation of the Rashba splitting of $n = 1$ IPS, ***Rashba Spin-Orbit Coupling in Image Potential States*** *while the latter concerns the study of the electronic dynamics of the $n = 1$ IPS for two different population mechanisms,* ***on- and off-resonant measurements of the IPS lifetime****.*

5.1 Rashba Spin-Orbit Coupling in Image Potential States

5.1.1 Introduction

The Rashba effect, extensively studied in these last years for the potential impact on spintronics and magnetoelectrics, is one of the most important consequences of spin-orbit interaction. The standard model for the Rashba effect relies on an isotropic two-dimensional electron gas (2DEG) that under broken inversion symmetry along the direction perpendicular to the 2DEG plane splits its spin-degenerate parabolic band into oppositely spin-polarized sub-bands displaced in opposite directions in momentum space [103–105]. Spin-polarized electronic states have been measured in a semiconductor heterostructure where a two-dimensional electron gas (2DEG) is confined in the band-bending region that behaves as a potential gradient perpendicular to the interface plane [106]. A much larger Rashba effect is known to exist at several heavy metal surfaces where the 2DEG is replaced by surface states and the potential gradient is given by the surface potential barrier. In this context, the surface state (SS) at the L gap of Au(111) represents the prototype of a Rashba-split state [107, 108], even if a giant Rashba effect has been measured also on the Ir(111) surface state [109]. In addition to the occupied surface states, all the (111) surfaces of noble metals support unoccupied image potential states, which, in principle, may exhibit a Rashba splitting as already theoretically predicted [110]. Nonetheless, no experimental evidence of a Rashba effect in IPS has been reported in the literature. Indeed, the discovery of this coupling on IPS could be exploited in the photoinduced charge transfer processes at the interface to inject spin-polarized electrons through the image potential state, opening new ways in the field of the femtosecond switching of magnetism [111, 112].

In this section the angle-resolved non-linear photoemission measurements performed at graphene/Ir(111) interface by using circularly polarized laser pulses are shown. The achieved results are confirmed by theoretical *ab-initio* calculations performed in Density Functional Theory (DFT).

5.1.2 Sample preparation and characterization

The graphene monolayer was grown on a clean Ir(111) surface in the LOTUS laboratory at the Sapienza University in Rome. The Ir(111) surface was cleaned by several cycles of sputtering by Ar^+ ions (2.0 keV) and annealing up to 1400 K, repeated until very sharp low-energy electron-diffraction (LEED) spots were observed. The sample temperature was measured with an infrared pyrometer pointed on the sample surface, and the heating was performed by electron bombardment from the crystal backside. The graphene monolayer was grown through the well stablished exposure to hydrocarbon molecules at high temperature [70], with a temperature-programmed growth (TPG) technique. The clean Ir(111) was exposed at room temperature to ethene (C_2H_4) for 120 seconds at the pressure of 5×10^{-8} mbar and then heated up to 1400 K for at least 60 seconds. After seven exposure-annealing cycles a very high-quality graphene monolayer on Ir(111) has been obtained, as verified by LEED and high-resolution Angular-Resolved Photoemission Spectroscopy (ARPES). The LEED pattern reported in Figure 5.1 shows a sharp superstructure associated to the long-range ordered moiré superlattice, due to the graphene and Ir(111) surface lattice constants mismatch, revealed by the smaller hexagonal pattern in the reciprocal space with sharp defined spots. Graphene grown with this

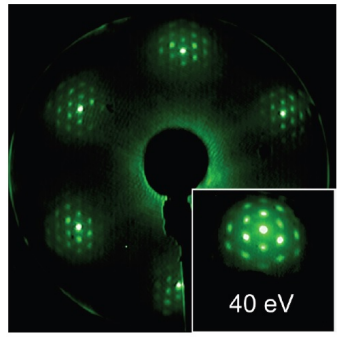

Figure 5.1: LEED pattern of graphene/Ir(111), measured at 80 K and with 140 eV electron energy. In the inset a zoom of the (0,0) spot of LEED pattern taken at 40 eV, measured by sligthly tilting the sample angle with respect to the normal direction, showing the moiré zero-order diffraction details.

method is a single monolayer, since this technique is self-limiting. The Ir(111) surface has a catalytic role in the ethene adsorption on the clean surface, that is suppressed wherever the surface is already covered by graphene, so that multiple layer regions can be avoided [70].

The high quality of graphene can also be demonstrated by ARPES. In fact, the formation of multi-layer graphene sheets has been clearly followed in the literature, by observing the emerging of one Dirac cone for each sheet [113]. Moreover, due the moiré superstructure resulting from the lattice mismatch between graphene and Ir(111), a corresponding superperiodic potential gives rise to the opening of moiré-induced minigaps in the band structure [53].
The ARPES data taken on the graphene monolayer grown on Ir(111), along the $\overline{\Gamma K}$ direction of the Brillouin Zone (BZ), are shown in Figure 5.2. The electronic band structure is characterized by the graphene Dirac cone at the $\overline{K}$ point of the reciprocal space, which exhibits the expected linear behavior, while the expected minigaps at the Dirac cones are not clearly visible. In the band map, also the Ir-related electronic bands are visible, among which the Rashba splitted orbitals close to the $\overline{\Gamma}$ point, basically unaffected by the up-lying graphene layer. Finally, the absence of any splitting or rounding of the Dirac cone constitutes definite evidence of the only-one-layer and quasi-free standing nature of the graphene monolayer.

5.1.3 Results and discussion

In order to verify the giant Rashba effect on the occupied surface state (SS) at the single-layer graphene/Ir(111) interface, we have performed linear angle-resolved 2PPE measurements (Figure 5.3b). To discriminate the occupied from the unoccupied surface states, the spectra have been acquired with two different photon energies, the first larger (hν=6.24 eV, Figure 5.3b) and the second smaller (hν=3.12 eV, Figure 5.3a) than the sample work function (ϕ= 4.45 $\pm$ 0.05 eV). The occupied Rashba-type SS appears at $E - E_{\mathrm{F}} \sim 6$ eV (Figure 5.3b), while the feature at $E - E_{\mathrm{F}} \sim 7$ eV (Figure 5.3a) is due to the first unoccupied image potential state (IPS1). The resulting binding energy at the $\overline{\Gamma}$ point is 0.58 ± 0.02 eV for IPS1 respect to the vacuum level and 0.26 ± 0.05 eV for the SS (0.195 ± 0.05 eV considering the minimum distance, out of the $\overline{\Gamma}$ point), with respect to the Fermi level. In agreement with Refs. [109, 114] the

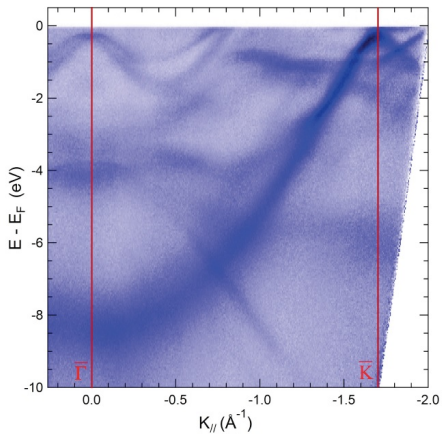

Figure 5.2: High Resolution ARPES band-mapping along the $\overline{\Gamma K}$ region of the BZ performed with a photon of energy hν=40.814 eV (He II_α) and with the sample kept at low temperature (80 K).

SS binding energy results shifted by about 150 meV with respect to the pristine Ir(111) surface state.

The $E(k_\parallel)$ dispersion of SS and IPS1 sampled by the spectra angular dispersion is displayed in Figure 5.3c. The IPS1 $k_\parallel$-dispersion fits well with a parabolic function with an effective mass close to the free-electron mass, $m^* = 1.04 \pm 0.06\ m_e$. The occupied surface state appears as two identical parabolic downward-dispersing structures resembling the dispersion of a Rashba-type spin-split surface state [103]. The two $E_\pm(k_\parallel)$ parabolas result well interpolated by [57, 66, 109, 114]:

$$E_\pm(k_\parallel) = E_0 + \frac{\hbar^2 {k_\parallel}^2}{2m^*} \pm \alpha_R |k_\parallel|, \tag{5.1}$$

where the two parabolas are shifted relative to the $k_\parallel = 0$ ($\overline{\Gamma}$ point) by $\Delta k_\parallel = (m^* \alpha_R)/\hbar^2$. The splitting relative to the $\overline{\Gamma}$ point amounts to $\Delta k_\parallel = 0.0377 \pm 0.0026$ Å^{-1}, resulting in the giant Rashba effect with $\alpha_R = (1.64 \pm 0.18) \times 10^{-10}$ eV·m in agreement with the values reported in literature [109].

In agreement with the weak interaction between graphene and Ir(111), the presence of graphene does not influence either the dispersion of the surface

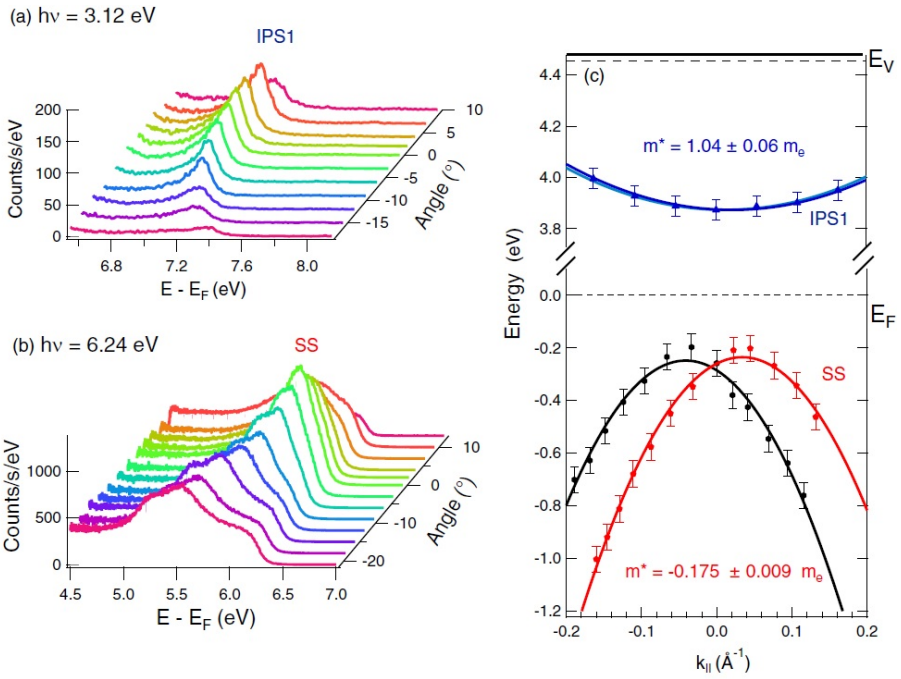

Figure 5.3: (a) Angle-resolved non-linear photoemission spectra collected with a photon energy of 3.12 eV and p-polarized light at the graphene/Ir(111) interface. (b) Angle-resolved linear photoemission spectra collected with a photon energy of 6.24 eV and p-polarized light at the graphene/Ir(111) interface. (c) Energy position versus $k_{\parallel}$-momentum for the first image potential state IPS1 and the surface states SS. The parabolic fits (lines) of the data give the effective masses reported in the figure.

state or the Rashba splitting, preserving the giant size of the Ir(111) surface state splitting.

When the Rashba effect is sufficiently large as for the Ir(111) SS, the spin-orbit splitting ΔE_{SO} is easily detectable as soon as we move away from the $\overline{\Gamma}$ point. Conversely, as recently reported for the surface states of topological insulators [115, 116], when the Rashba effect is not so large, circularly polarized laser pulses or a spin resolved detector are necessary. For this reason, in order to find a trace of a possible Rashba effect on the IPS1, we have irra-

diated the graphene/Ir(111) interface with circularly polarized laser pulses at $h\nu = 4.64$ eV. This pump photon energy has been suitably chosen to better highlight this effect. Being the SS-IPS1 energy difference at the $\overline{\Gamma}$ point ≈ 4 eV, the $h\nu = 4.64$ eV photon energy allows to populate, absorbing one-photon, IPS1 in a quasi-resonant way from SS at $k_{\|} \neq 0$. Since the work function of graphene/Ir(111) interface ($\Phi = 4.45 \pm 0.05$ eV) is smaller than the chosen $h\nu = 4.64$ eV photon energy, a potential difference of $\Delta V = +0.7$ V has been applied to the sample to remove the linear photoemission contribution (1PPE of Figure 5.4) in the spectrum. The two structures present in the two-photon photoemission spectrum collected at $k_{\|} = 0$ in p-polarization (Figure 5.4) represent the IPS1 and the $n = 2$ image state (IPS2), as also confirmed by the $k_{\|}$-dispersion collected in these experimental conditions (inset of Figure 5.4).

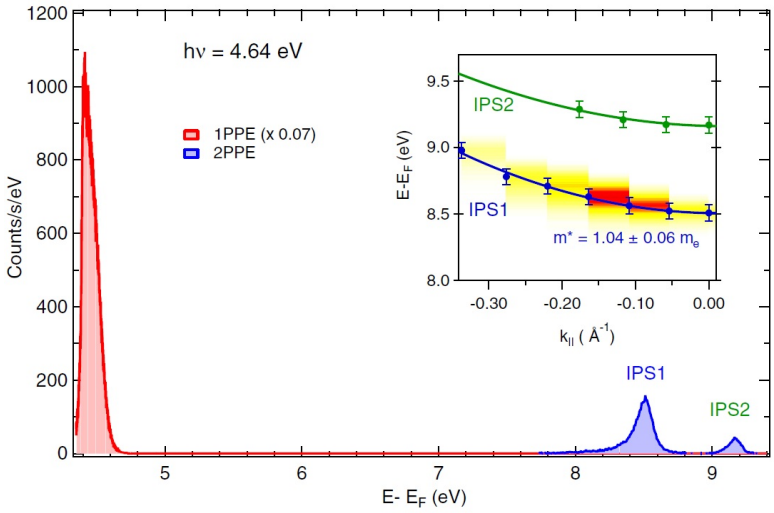

Figure 5.4: Comparison between non-linear photoemission (blue) and linear photoemission (red) spectra collected at a photon energy of 4.64 eV at $k_{\|}$=0 and p-polarized light. Being that the work function ($\Phi = 4.45 \pm 0.05$ eV) is smaller than the laser photon energy, in order to measure the non-linear contribution in the photoemission spectrum, a positive potential of +0.7 V was applied to the sample. In the inset we report the angular dispersion of the photoemission spectra collected at a photon energy of 4.64 eV.

Non-linear photoemission measurements with circularly polarized laser pulses have been performed by using two different photon energies. The $h\nu = 4.64$ eV is able to populate in a quasi-resonant way the IPS1 from the SS in particular at $k_{\|} \neq 0$. At this photon energy the IPS1 signal is more intense, however the population mechanism from the SS could affect the possible dichroism effect on the IPS1. At $h\nu = 3.12$ eV, instead, the IPS1 is populated by absorbing two photons from states deeper in energy than the SS and then it is one-photon photoemitted. This is confirmed by the multi-photonic orders (MPO) measured at hν=3.12 eV as a logarithmic slope of the electron emission versus the laser fluence (Figure 5.5b-c). In particular, MPO = 2 for the occupied Surface State indicates that it is photoemitted involving two photons. MPO = 3 for IPS1 proves that it is a third order photoemission process. A characteristic 2PPE spectrum collected with 3.12 eV photon energy at $k_{\|} = 0$ is shown in Figure 5.5a. The structure at $E - E_{\mathrm{F}} \sim 6$ eV represents the Surface State while the peak at $E - E_{\mathrm{F}} \sim 7$ eV is ascribed to the IPS1.

Figure 5.6 reports the left and right-hand circularly polarized two-photon photoemitted IPS1 structures, collected at emission angles corresponding to the electron wave vectors $k_{\|} = \pm 0.16$ Å^{-1} and $k_{\|} = 0$. While the IPS1 features at $k_{\|} = 0$ with left and right circular polarization well overlap, a dichroic signal is visible at $k_{\|} \neq 0$. The comparable dichroic signal, measured with the two photon energies, nullifies the doubt that initial state effect can be at the origin of the dichroism observed on IPS1. To better highlight this effect, we calculated the difference between the best fits of the IPS1 features collected with the two circular polarizations. The estimated spin orbit splitting results $\Delta E_{\mathrm{SO}} = 11.5 \pm 2.0$ meV at $k_{\|} = \pm 0.16$ Å^{-1}. Comparing this value with the spin-orbit splitting measured on the SS ($\Delta E_{\mathrm{SO}} = 525$ meV) at the same $k_{\|}$ value, we find that on the IPS1 the effect is forty-five times smaller than on the SS. Estimating a $k_{\|}$ splitting relative to the $\overline{\Gamma}$ point of $\Delta k_{\|} = 0.005 \pm 0.001$ Å^{-1}, the Rashba effect for the IPS1 results to be $\alpha_R = (3.6 \pm 0.6) \times 10^{-12}$ eV·m. We note that, while the energy shift of the IPS1 is comparable, a difference exists in the intensity of the dichroic signal measured with $h\nu = 4.64$ eV and $h\nu = 3.12$ eV. We believe that this effect can be ascribed to the population mechanism.

The different Rashba splitting of SS and IPS1 can be explained by their different spatial localization and decay at the surface, making them differently affected by the SO coupling. In particular, this has been invoked to explain the

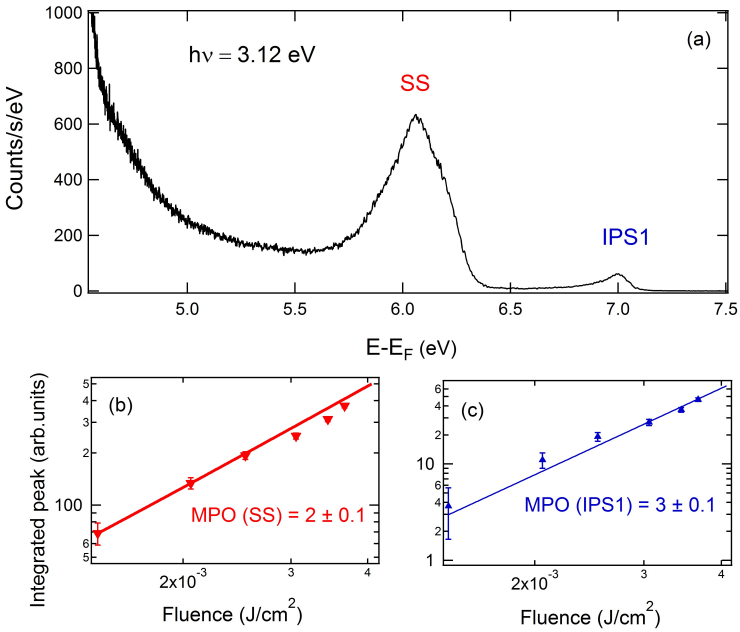

Figure 5.5: (a) Non-Linear Photoemission Spectrum collected at hν=3.12 eV at normal emission with p-polarized light. (b) Dependence on the laser fluence of the integrated area of the Surface state, SS (b) and Image Potential State, IPS1 (c). The estimated multi-photonic order (MPO) is 2 for the Surface State and MPO=3 for the Image Potential State, respectively.

larger SO splitting observed for SS of Au(111) with respect to Ag(111) [117], and the enhancement and reduction of the Rashba splitting in the surface state of Bi/Cu(111) upon Na and Xe adsorption, respectively [118]. In Ref. [110] McLaughlan *et al.*, using a relativistic multiple scattering theory, calculated the Rashba splitting of image state for Pt, Ir, and Au surfaces finding that, for $n = 1$, it is one order of magnitude smaller with respect to Au(111) SS, due to the smaller penetration of the wave function into the surface. In particular for the first image state of the clean Ir(111) surface they found $\alpha_R = 2.8 \times 10^{-12}$ eV·m.

It is in principle not obvious that a similar splitting could be found also in presence of graphene. Indeed the graphene sheet is expected to perform a

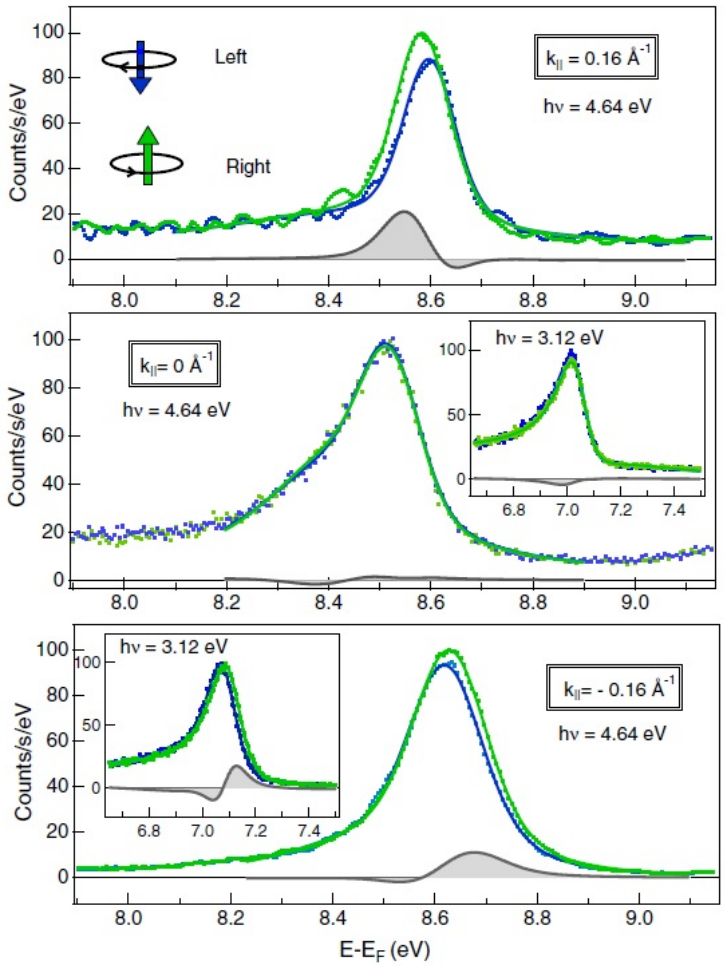

Figure 5.6: Comparison between non-linear photoemission spectra collected at a photon energy of 4.64 eV in right (green) and left (blue) circular polarization, and difference between the best-fit of the corresponding signals (gray). The measurements are acquired at $\overline{\Gamma}$ point ($\theta = 0°$) and at symmetric angles ($\theta = 9°$ and $\theta = -9°$) corresponding to $k_{||} = 0$ and $k_{||} = \pm 0.16$ Å^{-1}, respectively. In the inset, non-linear photoemission spectra collected at a different photon energy 3.12 eV by changing the circular polarization from right (green) to left (blue) at the same $k_{||}$ values ($k_{||} = 0$ and $k_{||} = -0.16$ Å^{-1}, the data at $k_{||} = +0.16$ Å^{-1} are not available due to experimental constrain). The dichroic signals measured with the two photon energies are comparable.

screening effect on external image charges, leading to a different spatial localization of the wave function at the surface. In order to investigate this aspect we have performed theoretical *ab-initio* calculations of the electronic properties of graphene/Ir(111). The calculations was performed in Density Functional Theory [119], using a pseudopotential representation of the electron-ion interaction and local orbital basis set, as implemented in the SIESTA code [120]. We use a generalized gradient approximation (GGA) for the exchange-correlation functional [121]. The plane wave cutoff has been fixed to 250 Ry and the Brillouin zone was sampled with 120 independent k-points. The Ir substrate was modeled by 20 atomic layers and the graphene sheet was placed at 3.54 Å from the surface layer. Graphene was expanded in order to match the lattice constant to that of Ir(111), for which the experimental value (3.839 Å) was taken. To obtain a good description of the electronic states outside the surface, the basis set has been improved using additional Ir localized orbitals in the region between the surface and graphene and C localized orbitals in the vacuum region, up to 5 Å outside the graphene plane. This allows to describe the pseudo image state, that lives outside the surface and is bound by the exponential potential tail in vacuum.

In Figure 5.7, we report the squared modulus of the first image state wave function along z for clean Ir(111) (red line) and graphene/Ir(111) (blue line), which is the relevant quantity to estimate the Rashba parameter. The latter can be indeed expressed as:

$$\alpha_R = 2/c^2 \int |\psi(z)|^2 \partial_z V dz, \tag{5.2}$$

where $|\psi(z)|^2$ is the charge distribution of the surface state along the surface normal and $\partial_z V$ is the derivative of the atomic potential [118, 122]. Due to the very short range nature of the last term, the integral in Eq. (5.2) has to be determined in a very small region around the atomic core. Being the gradient of the atomic potential antisymmetric in the relevant region around the nuclear position, only the asymmetric part of the surface state charge density along z, which is related to the asymmetry of the surface potential, contributes to the integral. In particular, the Rashba parameter will depend on the amplitude of the wave function at the surface and on its decay into the substrate.

From the results reported in Figure 5.7 we find that in presence of graphene,

the amplitude of IPS1 charge distribution on the first Ir layer is only 3.5 times smaller than that on clean Ir(111) while the decay factor is almost unchanged. Hence a small Rashba splitting is expected for this state. The linear screening density, due to an external charge [123] (see the inset in Figure 5.7), confirms the only partial screening of the carbon layer. In presence of graphene, the image plane does not follows rigidly the surface layer: its outward shift of 2.72 Å with respect to the clean surface is indeed smaller than the Ir-graphene distance, equal to 3.5 Å.

The comparison with the charge density distribution of the SS of Ir(111) (green line), characterized by amplitude two order of magnitude larger than IPS1 and a more marked asymmetry in the surface layer, confirms a more sizable Rashba splitting for this surface state, in agreement with the experimental measurements and the literature [110].

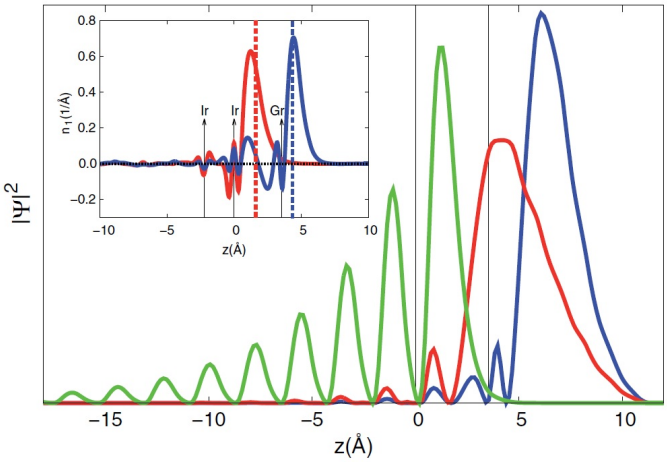

Figure 5.7: Squared amplitude of the wave functions at $\overline{\Gamma}$ of SS of Ir(111) (green), IPS1 of Ir(111) (red), and IPS1 of graphene/Ir(111) (blue). Vertical lines correspond to the Ir surface layer ($z = 0$) and graphene plane. In the inset: plot of the linear screening density n_1 of Ir(111) and graphene/Ir(111) due to the application of an external charge. The arrows mark nuclear positions while vertical dashed lines represent the image plane of the two systems.

5.1.4 Conclusions

This section presents a detail angle-resolved 2PPE study of the interface states at the single-layer graphene/Ir(111) system. In particular, by using circularly polarized femtosecond laser pulses the Rashba effect has been experimentally revealed for the first time on the $n = 1$ IPS. The value of the Rashba effect on the IPS1 results 45 times smaller than one measured on the same surface on the occupied SS. If the spin-orbit coupling is the same for both states, this difference can be ascribed both to the smaller amplitude of the IPS and to the smaller asymmetry of the image state charge density with respect to the SS around the Ir nuclear position. The presence of the graphene sheet is expected to reduce slightly this effect with respect to the clean surface case. This discovery, by exploiting the spin-split image state, could open new scenarios for the understanding and the control of the magnetism at interfaces.

5.2 On- and off-resonant measurements of the $n = 1$ IPS lifetime

5.2.1 Introduction

The investigation of image pontential states lifetimes at the graphene/metal interfaces, as recently reported in literature [48, 57, 65, 66], allows to have information about the interaction of graphene with the metallic surface and about the interfacial quality. The lifetime of the IPS can be measured by estimating the intrinsic line-width of the feature ascribed to the IPS in the non-linear photoemission spectrum as well as by time-resolved photoemission measurements. In the former, the lifetime is affected by both the depopulation time and the pure dephasing time due to elastic scattering processes that destroy the phase relation between the involved states without altering the IPS population [35, 124, 125]. Time-resolved photoemission measurement, on the contrary, is not affected by elastic scattering processes and then represents the only technique able to directly measure the depopulation time.
Despite the first measurements of the IPS lifetime date back to the late nineties, it remains unclear why, in (111) metal surfaces where an occupied surface state and IPS are observed at $\overline{\Gamma}$, the lifetime estimated by the line-width depends on the population channel of the IPS. By tuning the pump laser photon energy in the VIS-UV energy range it is possible to directly populate electrons from the SS in the IPS. When IPS is resonantly populated from the SS, its line-shape in the photoemission spectrum drastically modifies preventing the measure of the IPS lifetime. In the past, the IPS line-width change has been ascribed to the elastic scattering processes, that are complicated to theoretically simulate and to experimentally control, being strongly dependent on the surface quality.

In this section, time-resolved photoemission measurements based on the pump-probe setup are performed at different pump photon energies. The measured depopulation time of the $n = 1$ IPS, populated in- and out-of-resonance from the SS at the graphene/Ir(111) interface, is compared with the results obtained from the study of the $n = 1$ IPS line-width and successfully modeled employing the optical Bloch equations for a two levels system.

5.2.2 Results and discussion

Figure 5.8a shows the 2PPE measurements acquired at the single-layer graphene grown on Ir(111) surface by tuning the incident photon energy from 3.2 eV to 4.1 eV, at normal emission ($k_{\parallel} = 0$) and with p-polarized light. The two features related to the Rashba-type surface state (SS) and to the $n = 1$ image potential state (IPS1) are well identified in the spectra collected with photons of energy lower than 3.8 eV. In this photon energy range the IPS1, as proved by the MPO measurements shown in the previous section, is populated by absorbing two photons and then one-photon photoemitted and it appears as a small feature at higher energy with respect to the Fermi edge. When the photon energy approaches the SS $\rightarrow$ IPS1 optical transition at ≈ 4 eV (inset of Figure 5.8a), the $n = 1$ IPS is directly populated from SS and a strong increase of the photoemission intensity is observed. This value was confirmed by tracking the energy position of IPS1 and SS versus the photon energies (Figure 5.8b). As expected for an unoccupied state, the energy position of the $n = 1$ IPS shifts as the laser photon energy difference ($\Delta E = \Delta h\nu$), while the occupied SS shifts with twice the photon energy ($\Delta E = 2\Delta h\nu$). The crossing point ($h\nu$=3.95 $\pm$ 0.05 eV) corresponds to the direct SS $\rightarrow$ IPS1 optical transition energy. The IPS1 photoemission intensity versus the photon energy shows a maximum when the latter is resonant with the SS-IPS1 transition, and as discussed in literature, the line-shape of the resonance results well fitted by a Lorentzian function (Figure 5.8c).
The intrinsic line-width collected out-resonance, at 3.5 eV, results, as expected smaller than the value measured on resonance [32].

To get insight into the depopulation and the pure dephasing time of the IPS1, we have collected time-resolved 2PPE measurements at two different pump photon energies. We have excited the sample, at first, with a pump pulse photon energy of 3.5 eV where IPS1 is populated by a non-resonant two photons process and then photoemitted, and subsequently with a pump of 3.95 eV that directly excites IPS1 from SS. In both cases the probe pulse has been fixed at 1.55 eV. The spectra acquired at single-layer graphene/Ir(111) interface at different delay times between the pump and the probe in the two configurations are shown in Figure 5.9.

In Figure 5.9a, being the pump photon energy out-resonance, the SS and

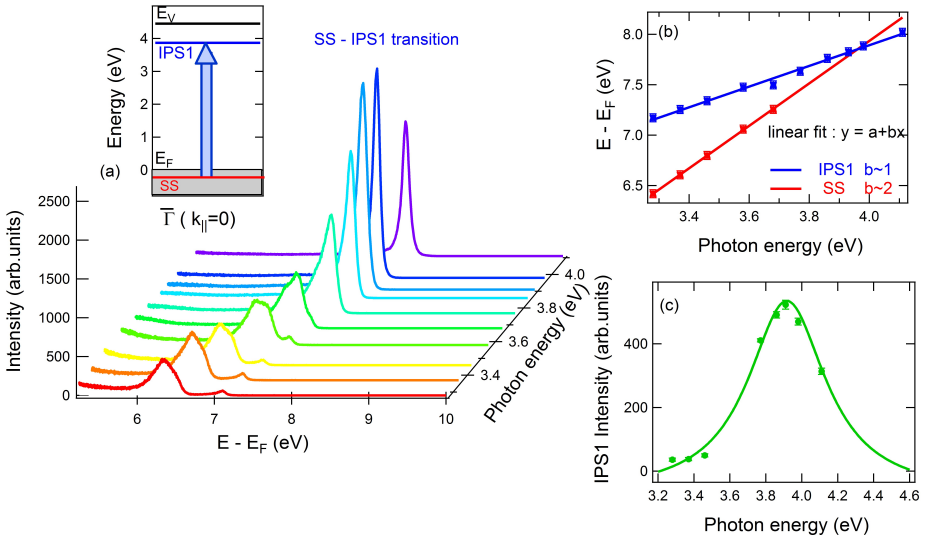

Figure 5.8: (a) 2PPE spectra measured at the single-layer graphene/Ir(111) interface by tuning the photon energy from 3.2 eV to 4.1 eV, at normal emission ($k_{\parallel} = 0$) and with p-polarized light. In inset: simple sketch of the energy levels at $\overline{\Gamma}$ point of the Brillouin Zone. (b) Energy position of the IPS1 and SS emissions versus the photon energy of the laser pulse. The crossing point corresponds to the SS $\rightarrow$ IPS1 optical transition energy (≈ 4 eV). (c) 2PPE Intensity of IPS1 versus the pump photon energy.

IPS1 structures are well distinguished. The intensity of the SS feature at 4.7 eV, as well as the IPS1, increases with the decrease of the pump-probe delay being photoemitted absorbing one photon of the pump and one of the probe. This allows, in this case, to track the pump-probe cross-correlation trace (red dashed Gaussian curve of Figure 5.10a) and then to unambiguously establish the zero time of the pump-probe delay. In Figure 5.9b, the spectra collected with

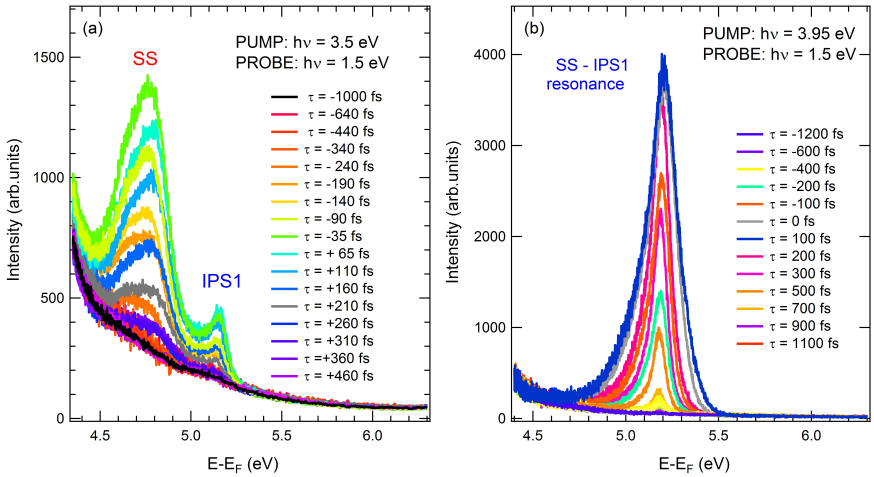

Figure 5.9: (a) Time-resolved 2PPE spectra measured at graphene/Ir(111) interface by using a hν =3.5 eV photon as the pump and hν =1.5 eV as the probe at different pump-probe delay times, at normal emission ($k_{\parallel} = 0$) and with p-polarized light. (b) Time-resolved 2PPE spectra acquired on graphene/Ir(111) interface by using a hν =3.95 eV photon as the pump and hν =1.5 eV as the probe at different pump-probe delay times, at normal emission ($k_{\parallel} = 0$) and with p-polarized light.

3.95 eV pump photon energy are dominated only by the IPS1, being resonantly populated from the SS, and then it is not possible to obtain directly from the photoemission spectra the pump-probe temporal coincidence.

Figure 5.10 shows the integrated area of the IPS1 feature versus the pump-probe delay time for the two pump photon energies. When the IPS1 is populated out-resonance (Figure 5.10a), the data of the IPS1 integrated intensity are compared with the cross-correlation trace obtained from the photoemission spectra by plotting the integrated area of the SS feature versus the pump-probe delay. The IPS1 data are well interpolated by a symmetric Gaussian with a full-width-half maximum (FWHM) comparable with the cross-correlation trace and shifted of about 20 fs with respect to $\tau = 0$ fs (Figure 5.10a). The latter, as shown in the following, is a consequence of the finite depopulation time, T_1, of the IPS1 [32, 126]. Otherwise, when the graphene/Ir(111) interface is excited

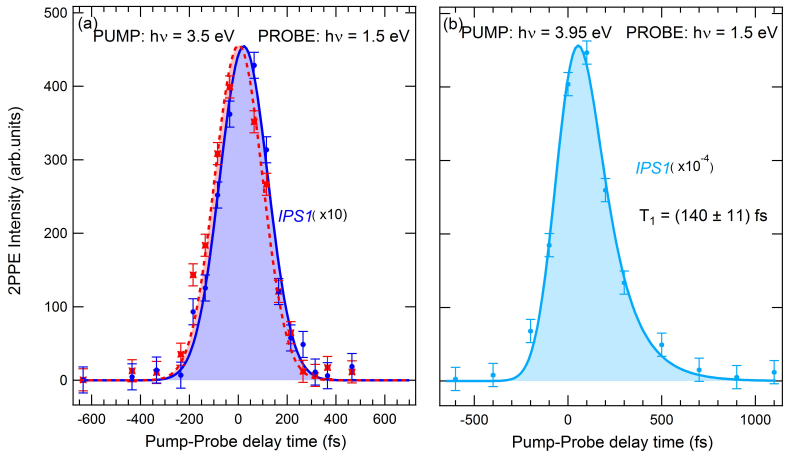

Figure 5.10: Integrated area of $n = 1$ Image Potential State at $\overline{\Gamma}$ ($k_{\parallel} = 0$) versus pump-probe delay times for two configurations: (a) hν = 3.5 eV photon energy as the pump and hν = 1.5 eV as the probe , (b) hν = 3.95 eV photon energy as the pump and hν = 1.5 eV as the probe. The red dashed Gaussian curve is the pump-probe correlation trace from the SS. The data have been fitted with a Gaussian curve (fwhm=230 fs) , convolved with a decreasing exponential. The IPS cross correlation traces were multiplied so as to be normalized to the SS cross correlation intensity.

with a photon of energy hν =3.95 eV and the IPS1 is directly populated from the SS, the IPS1 integrated data (Figure 5.10b) are no longer symmetrical and T_1 can be deduced from the exponentially decaying tail. The experimental data have been interpolated with a decreasing exponential curve convoluted with a Gaussian to take into account the laser pulse. The Gaussian FWHM is given by the laser pulse cross-correlation obtained outside to the vacuum chamber by using, as usual, a non-linear crystal. The estimated depopulation time of the IPS1 measured in resonance results $T_1 = 140 \pm 10$ fs. In this case, the temporal shift with respect to the pump-probe coincidence cannot be experimentally deduced.

For a careful interpretation of the measured dynamics, we have resorted to the Optical Bloch Equations (OBE) for a two levels system, represented by the initial state $|1\rangle$ and the intermediate state $|2\rangle$ that in our case is the IPS1

(the time response of the final state population is neglected, assuming that the coherence in the final state is immediately lost). The optical Bloch equations for the density matrix elements ρ_{ij} (i,j=1,2) of a two-level system in the dipole and rotating frame approximation are described by the following equations [127]:

$$\frac{d\rho_{22}}{dt} = -i\mu_{12}E_{pump}(t)(\rho_{12} - \rho_{21}) - \frac{1}{T_1}\rho_{22} \tag{5.3}$$

$$\frac{d\rho_{21}}{dt} = -i\mu_{12}E_{pump}(t)(\rho_{22} - \rho_{11}) - \left[i\hbar(\omega_{12} - \omega_{pump}) + \frac{1}{T_2}\right]\rho_{21} \tag{5.4}$$

$$\rho_{22}(t) + \rho_{11}(t) = 1 \qquad \rho_{21} = \rho_{12}^{*} \tag{5.5}$$

where μ_{12} is the transition dipole moment and E_{pump} is the envelope of the pump pulse. Here, T_1 is the depopulation time of the intermediate state $|2\rangle$ and T_2 is its dephasing time. As well known, T_2 is related to the intrinsic line-width Γ_2 of the photoemitted intermediate state by $\Gamma_2 = 2\hbar/T_2$ and to the relaxation time T_1 by [126]:

$$T_2 = \left(\frac{1}{2T_1} + \frac{1}{T_2^{*}}\right) \tag{5.6}$$

where T_2^{*} , the pure dephasing time, takes into account the elastic scattering processes between electrons in the intermediate state. By fitting the feature ascribed to the $n = 1$ Image Potential State in the 2PPE spectrum measured at a photon energy of 3.56 eV (light green spectrum of Figure 5.8a) with a Lorentizian convoluted with a Gaussian curve, which takes into account the experimental resolution (35 meV), we found an intrinsic line-width $\Gamma_2 = 75.5 \pm 7$ meV and, consequently, T_2 =17.5 ± 2 fs. These values, inserted in the OBE, together with the parameters of the pump pulse, allow to numerically solve the OBE and compare the population of the intermediate state ρ_{22} with the IPS1 integrated intensity reported in Figure 5.10a. In Figure 5.11a, the solution of the OBE for the population ρ_{22} of the IPS1 populated in a non-resonant way ($\Delta\hbar\omega = \hbar(\omega_{12} - \omega_{pump}) = 0.5$ eV) that best interpolates the IPS1 integrated area is shown. The depopulation time results T_1=35 ± 5 fs, comparable with the one reported in literature for the same interface [66]. The temporal shift of the ρ_{22} maximum from τ=0 is $\Delta\tau$= 16.5 ± 2.5 fs, comparable with the experimental data obtained from TR-2PPE measurements. As already discussed

in the previous section, when graphene is grown on Ir(111), the $n = 1$ IPS wave function is pushed toward the vacuum, the penetration into the substrate is reduced and then IPS1 lifetime is slightly longer than that observed on bare Ir(111).

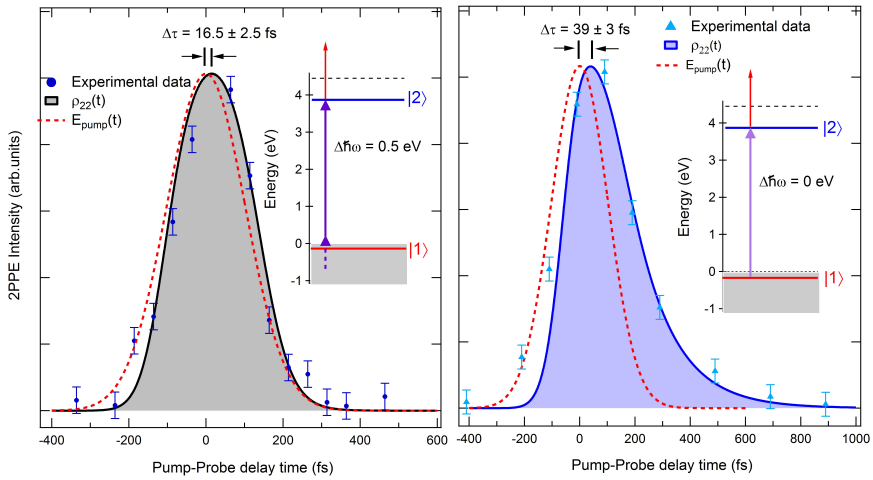

Figure 5.11: (a) Solution of the OBEs for the excited state population ρ_{22} (black line) in a non-resonant configuration $\Delta\omega$ =0.5. (b) Solution of the OBEs for the excited state population ρ_{22} (blue line) in a resonant configuration $\Delta\omega$=0. The blue and light blue dots represent the TR-2PPE data and the red dashed Gaussian curve the envelope of the pump pulse.

In Figure 5.11b, the OBE solution for the resonant case, i.e. $\Delta\omega$=0, is shown.The OBE solution that well approximate the experimental data gives a temporal shift of ρ_{22} maximum from $\tau = 0$ of $\Delta\tau = 39 \pm 3$ fs that corresponds to T_1=140 $\pm$ 5 fs. At this light, we can conclude that from these measurements an intriguing result emerges, the IPS1 depopulation time strongly depends on the population mechanism. When the $n = 1$ IPS is resonantly populated by the SS, the depopulation time results longer than the one measured out of resonance when the initial state belongs to the continuum of the bulk states of the Ir(111).

5.2.3 Conclusions

In this section, the depopulation time of the $n = 1$ Image Potential State on a single layer graphene grown on Ir(111) has been investigated by means of Time-Resolved 2PPE and modeled employing the optical Bloch equations for a two levels system. The joint effort of these two investigative methods allows us to accurately study the lifetime of the IPS1, also when it is considerably shorter than the laser pulse duration, and to estimate the time shift of the maximum of the IPS1 correlation trace with respect to the pump-probe temporal coincidence. Furthermore, we have shown that the IPS1 lifetime is strictly correlated to the population process and, in particular, that it increases significantly when IPS1 is directly populated from the surface state. In order to deeper understand this behavior further experimental measurements and theoretical calculations have been planned.

Chapter 6

Interface states at the single-layer Graphene/Ni(111) system

Single-layer graphene grown on nickel surface is a representative case of strongly interacting graphene/metal interface, as well as a special case of a lattice matched system. The close lattice match between graphene and Ni allowing the growth of commensurate epitaxial graphene on Ni(111), makes nickel a unique substrate material for graphene/metal interface. Futhermore, this interface has been predicted to act as a spin-filtering, making graphene/Ni(111) interface very promising for spintronic devices.
In this chapter by combining non-linear photoemission experiments and density functional theory calculations we investigate the electronic states at the graphene/Ni(111) interface with particular attention to the spin polarization.

6.1 Introduction

The graphene-ferromagnet interfaces have been widely studied in recent years in view of possible spintronic applications. In particular, the graphene/Ni interface represents an interesting case of ideal spin filtering [51, 128] due to the commensurate growth of graphene on Ni(111) surface and to the overlap of their electronic band structure which differs for the two spin orientation [129, 130].

For the realization of spintronic devices it is necessary that the remarkable properties of graphene and in particular its cone-like dispersion near the Fermi level are preserved [131]. While in the case of weakly interacting substrates (i.e. Cu, Ir, Pt) the Dirac cone remains almost undisturbed [44, 53], in strongly interacting systems (i.e. Ni, Co, Ru, Rh) the graphene bands result strongly modified [44,48]. In the case of Co and Ni substrates, for example, the strong hybridization between the graphene π bands and the metal d-states splits the Dirac cone in several parts, which partially retain cone-like features [129,130,132–134]. The electrons filling these states can behave as massless Dirac fermions or can acquire a small effective mass, depending on the arrangement of graphene on the underneath substrate [135].

Experimental evidence suggests that the interface between graphene and these magnetic substrates can be source of spin polarized electrons with possible application for the injection of spin polarized current [136]. Furthermore, spin current injection via optical methods would remove the need for ferromagnetic contacts, identified as a possible source of spin scattering. This technique proved to be an efficient alternative to electrical driven spin injection [137, 138].

In this chapter, we investigate the possibility to optically inject electrons into unoccupied interface states localized in a two dimensional region parallel to the surface of the graphene/Ni(111) interface, i.e. Image potential states or Quantum well states, giving rise to possible spin-polarized current. Image potential states, in particular, due to their long lifetime and to the spatial localization of their wave function outside the surface represent an efficient charge transfer channel at the interface.

It was demonstrated that optical spin injection into image potential states is possible, analogously to ferromagnetic-semiconductor heterostructure [138], both on magnetic and non-magnetic metal substrates. In the latter case multi-photon excitation is realized with circularly polarized light combining optical

transition selection rules with spin-orbit coupling of the substrate [139, 140].

Here, by a theoretical and experimental joint effort we investigate the possibility to excite spin-polarized electrons into the $n = 1$ image potential states of a single-layer graphene/Ni(111) interface.

6.2 Sample preparation and characterization

The epitaxial graphene was obtained using a Ni(111) crystal presenting carbon-contaminated subsurface, as defined in Ref. [141]. After the usual cleaning procedure in UHV (sputtering and annealing), the formation of graphene at the Ni surface is observed when the temperature reaches 500-600°C. Under these conditions, the graphene islands expand, fed by the C atoms from the subsurface reservoir, leading to a complete, mainly epitaxial, graphene overlayer [141]. Dosing C_2H_4 ($10^{-7} - 10^{-6}$ mbar), after the graphene nucleation, increases the growth rate, without affecting the final graphene morphology. In this work a carbon-contaminated subsurface Ni(111) substrate has been prepared in UHV after several cycles of Ar^+ sputtering at 2 KeV. This procedure was necessary to remove the surface contaminants and oxidation due to air exposure, but it was not strong enough to remove also the carbon reservoir. Then it was annealed at 550°C for 60 minutes, back-filling the chamber with C_2H_4 (2×10^{-6} mbar), obtaining a complete epitaxial graphene monolayer, as confirmed by LEED (Figure 6.1) and Ultraviolet Photoelectron Spectroscopy, UPS (Figure 6.2) . Figure 6.2 shows the valence band spectra of the epitaxial graphene (top) compared to the clean Ni(111) (bottom). The spectra were acquired in normal emission geometry at room temperature, using He II photons ($h\nu$ =40.21 eV), with a total energy resolution of ∼0.15 eV and analyzer acceptance angle of ∼5°. The appearance of the graphene related π band at 10 eV, the typical energy due to the graphene-Ni(111) interaction, without any other second layer related structures at lower binding energy, gives the direct evidence that a single epitaxial graphene layer is formed [142].

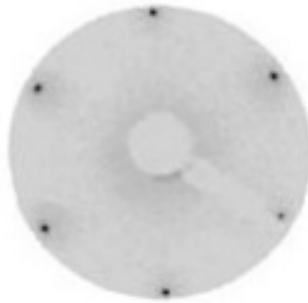

Figure 6.1: LEED pattern of epitaxial graphene grown on Ni(111), acquired at RT and with $\sim$ 70 eV electron energy.

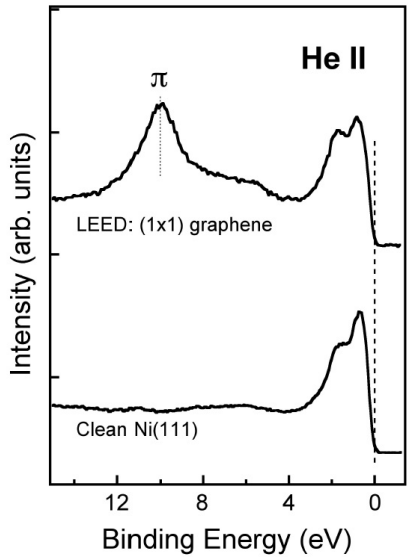

Figure 6.2: UPS spectra of clean Ni(111) surface (bottom) and of epitaxial graphene overlayer on Ni(111) (top) acquired in normal emission geometry at room temperature, using He II_α photons ($h\nu$ =40.21 eV).

6.3 Results and discussion

In the 2PPE measurements the laser photon energy has been tuned in order to unambiguously reveal the emissions originating from the occupied and unoccupied states in the energy region around the Fermi level (E_F). Figure 6.3a shows the spectrum acquired on graphene/Ni(111) with a photon energy of 3.90 eV, with p-polarized light and at normal emission ($k_{\|} = 0$). The edge at $E - E_F \sim 7.8$ eV represents the emission from E_F by two photons absorption. Three main features, labeled as Quantum Well State, QWS ($E - E_F \sim 6$ eV), Image Potential State, IPS ($E - E_F \sim 7.2$ eV), and the resonance Surface State, SS ($E - E_F \sim 7.5$ eV), are observed.
To identify the structures belonging to the occupied electronic structure, a linear photoemission measurement using a photon energy $h\nu = 6.28$ eV was recorded. The structure at $E - E_F \sim 6$ eV in Figure 6.3b has been identified as the SS state of the 2PPE spectrum, while a new wide feature labeled as SS2 at $E - E_F \sim 5.4$ eV appears.

The structures observed in the spectra have been fitted with a Lorentzian convoluted with a Gaussian function accounting for the experimental resolution (35 meV). For all the measured features, except SS, two Lorentzians are necessary to adequately fit the corresponding peak. This suggests that, conversely to SS structure, two components contribute to the IPS, QWS, and SS2 photoemission feature.

Comparing the two spectra reported in Figure 6.3a and Figure 6.3b we assess that SS and SS2 are occupied states with binding energy of 0.25 ± 0.05 eV and 0.85 ± 0.05 eV, respectively with respect to the Fermi level. Differently QWS and IPS are unoccupied states and their binding energies, referred to the vacuum level, are 2.1 ± 0.05 eV and 0.95 ± 0.05 eV, respectively. The binding energy of IPS is comparable with the 0.80 ± 0.03 eV value measured on polished Ni(111) [143] and the 0.74 ± 0.03 eV on a similar interface (graphene/Au/Ni(111)) [57].

This scenario is confirmed by collecting the 2PPE spectra by changing the laser photon energy from 3.4 eV to 3.9 eV (Figure 6.3c) and by tracking the energy position of IPS and SS versus the photon energy (Figure 6.3d). As expected, the energy position of the unoccupied QWS and IPS shifts as the laser photon energy ($1\Delta h\nu$), while the occupied SS shifts with twice the photon energy ($2\Delta h\nu$). As it can be observed in Figure 6.3c, the IPS feature can be

detected only by using photon energies larger than 3.5 eV, that corresponds to the transition from SS to IPS. Differently, when the photon energy is resonant with the SS-IPS transition, we do not observe a strong increase of the IPS photoemission intensity. The absence of a clear resonance, as conversely shown for the graphene/Cu(111) and graphene/Ir(111) in chapter 4 and chapter 5, is the first evidence of the intriguing origin of the SS peak.

In order to shed light on the nature of such occupied and unoccupied surface states, in collaboration with the theoretical group of Dipartimento di Chimica, Università degli Studi di Milano and CNR-ISTM, we performed calculations for graphene/Ni(111) in the top-fcc structure. In fact, although the coexistence of different stable chemisorbed graphene configurations on Ni(111) has been observed, i.e. top-fcc, top-hcp, and top-bridge, by comparison of experimental and simulated STM images, a general predominance of top-fcc has been proved [144]. The *ab-initio* electronic structure calculations were carried out in density functional theory [145] within the generalized gradient approximation, employing the Perdew-Burke-Ernzerhof functional [121] to handle exchange and correlation effects. According to the self-consistent method implemented in the SIESTA code [120] the core electrons were described by a separable norm conserving pseudo-potential.
The calculated density of states (DOS) and the band structure of single-layer graphene/Ni(111) are reported in Figure 6.4. The surface features in the band structure are highlighted in red, while different colors in the DOS correspond to the projection on different atoms in the system. The DOS at the $\overline{\Gamma}$ point confirms the experimental results regarding the unoccupied states, QWS and IPS, whose energies relative to E_F are 2.18 eV and 3.51 eV for majority component and 0.1 eV higher for the minority one. The comparison between the band structures of the graphene covered Ni(111) and that of the clean surface confirms the nature of the QWS that originates from the surface state of Ni(111) (near the Fermi level at $\overline{\Gamma}$) upward shifted in energy due to the interaction with the graphene layer [146]. This assignement is supported also by the projected density of states in different volumes showing that this state is spatially localized on the surface Ni layer (purple line), while the IPS is mainly localized in the vacuum region outside the surface (green line). Concerning the occupied states, the DOS and the band structure at $\overline{\Gamma}$ allow to identify SS2 with a minority spin surface state, whose calculated binding energy is 0.72 eV. The binding energy

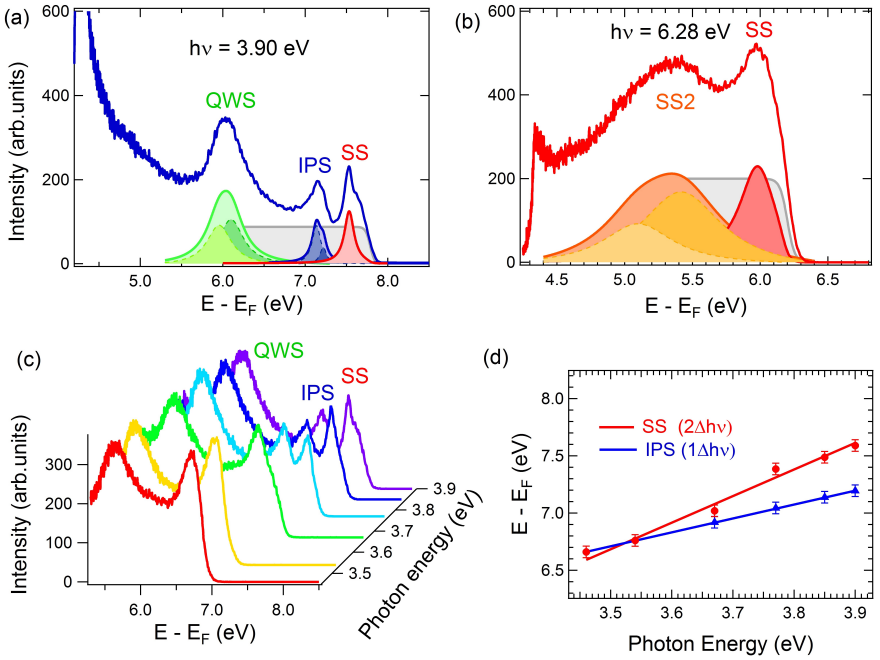

Figure 6.3: (a) The graphene/Ni(111) 2PPE spectrum, as measured with p-polarized light at a photon energy of 3.90 eV and normal emission ($k_{\|} = 0$) geometry. The shaded peaks are the sum of the Lorentzian curves used to fit each experimental feature, while the grey curve is the Fermi edge. (b) The linear photoemission spectrum collected at a photon energy of 6.28 eV at normal emission ($k_{\|} = 0$) with p-polarized light for the same interface. (c) The graphene/Ni(111) 2PPE spectra collected by tuning the photon energy across the SS-IPS transition (from 3.4 eV to 3.9 eV), at normal emission ($k_{\|} = 0$) and with p-polarized light. (d) Energy position of the IPS and SS features versus incident photon energy. The point where the two lines cross corresponds to the SS-IPS transition energy.

of majority spin component of this state (1.1 eV) reasonably agrees with that of the less intense Lorentzian used to fit the experimental data.

In order to identify the SS state we note that the sharp line-shape of the peak in the experimental spectra (see Figure 6.3a,b) suggests it to be related to an electronic state localized at the surface and with a relevant spectral weight

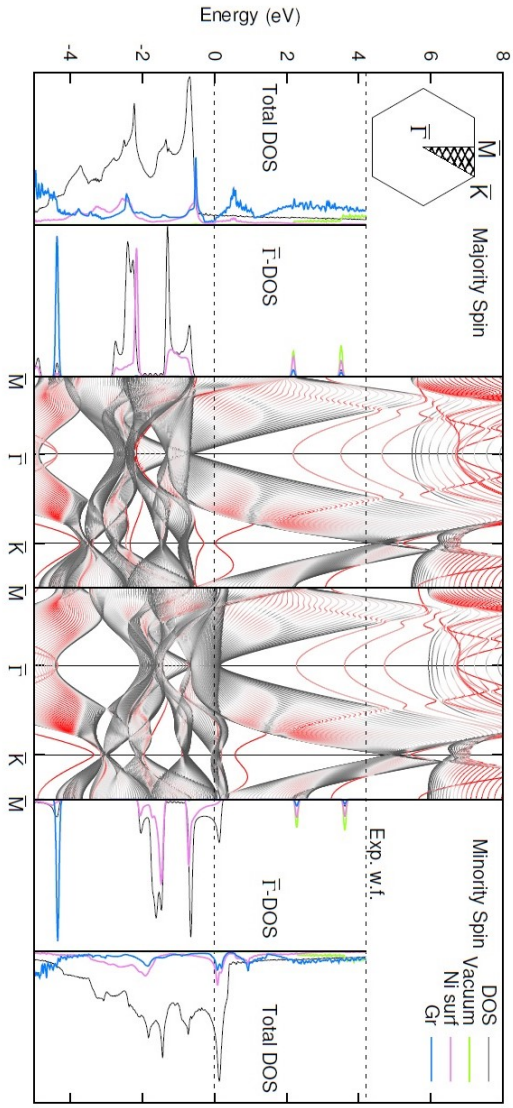

Figure 6.4: DOS and band structure of graphene/Ni(111). Red intensity in the band structures corresponds to the surface character. DOS projected on different atoms in the system are reported with different colors.

on carbon atoms, similarly to IPS and QWS. Looking at the theoretical band structure at $\overline{\Gamma}$ we cannot find any candidate because the majority component does not present any state at the corresponding energy while the minority states have no weight on graphene, as they belong to the Ni d bands.

The lack of the SS at $\overline{\Gamma}$ in the calculated electronic structure together with the absence of a resonant emission profile when the IPS should be resonantly populated from SS (see Figure 6.3c), suggest that this feature could be originated from occupied states lying at $k_{\parallel} \neq 0$. Comparing the valence band spectrum taken by using a conventional He lamp (hν=40.21 eV) and linear photoemission spectra (hν=6.28 eV), Figure 6.5, the hypothesis that the features observed in linear photoemission spectrum close to E_{F} could be electronic structures at $\overline{\Gamma}$ point different from surface states, e.g. the d bands, results unlikely. The d bands are characterized by two intense structures, at about 1 eV and 2 eV with respect to the Fermi level. In the spectrum collected with 6.28 eV only the first structure at about 1 eV is accessible from the photon energy and could contribute to the feauture at 0.8 eV. On the contrary the SS feature is completely absent from the spectrum at 40.21 eV.

A closer inspection of the band structure points out the presence of a graphene band in the majority spin component only, which gives rise to a mini-cone near E_{F} [131], around $\overline{\mathrm{K}}$, and extends itself with nearly flat dispersion toward the $\overline{\mathrm{M}}$ point.
The hypothesis that the SS state observed in the photoemission spectra derives from an indirect transition with a $k_{\parallel}$ exchange leads to consider the DOS integrated over the whole Brillouin zone. The carbon contribution (blue line) presents a structure in the majority spin component with a binding energy comparable to that of SS. This peak is hybridized with the d_{z^2} component of the Ni substrate (purple line). As reported in different works on different surfaces, i.e. Cu(111) [30] or HOPG [90, 147], the possibility of an indirect transition is likely. While in the direct excitation process the transitions between levels are settled by the electric dipole selection rules, in the case of indirect transition, i.e. $\Delta k_{\parallel} \neq 0$, these rules can be violated [30]. To better understand, we have performed two-colors photoemission measurements using as pump pulse a photon energy of $h\nu = 3.62$ eV and as a probe pulse 3.14 eV and considering both s and p polarizations. This pump photon energy enables the resonant population of the IPS from SS.

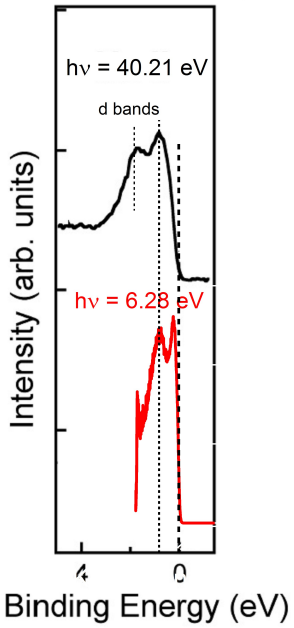

Figure 6.5: Spectrum of single-layer graphene/Ni(111) interface acquired in normal emission geometry ($k_{\parallel} = 0$) using a photon of energy 40.21 eV (black) compared to the spectrum collected using a photon of energy 6.28 eV (red).

In the spectra reported in Figure 6.6 we are mainly interested in the two structures closest to the Fermi edge. The first one is the IPS populated and photoemitted by absorbing two pump photons (long arrows). According to the electric dipole selection rules for the surface states, this feature is quenched when the laser beam is s-polarized (light blue line) [30, 148].
More intriguing is the case of the structure at $E - E_{\mathrm{F}} \sim 6.4$ eV, representing the IPS, populated from the SS with a pump photon, and photoemitted absorbing a probe photon. In this case, while the dipole selection rule is still valid for the photoemission process from the IPS, the population from SS is possible both in s and p polarizations (light blue and pink arrows, respectively), violating the dipole selection rules.

It is worth noting that, looking at the $\overline{\Gamma}$ point of the band structure, also

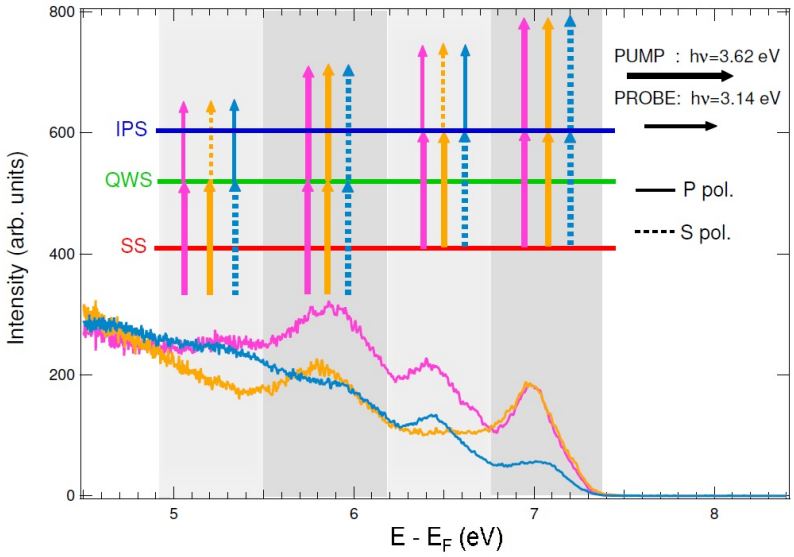

Figure 6.6: Two colors 2PPE spectra acquired at graphene/Ni(111) by changing the combination of polarization (s or p) between pump ($h\nu$ = 3.62 eV, long arrow) and probe ($h\nu$ = 3.14 eV, short arrow) pulse: pink line → pump p and probe p, yellow line → pump p and probe s, light blue line → pump s and probe p.

the minority spin d-band near the Fermi level could serve as initial states for the IPS population. Also for this transition, indeed, the dipole selection rules are not fulfilled. Therefore, although the cross section of the transition and the properties of the involved states (symmetry, spatial localization) make this process disadvantaged, we can not exclude this channel of injection of electrons in the IPS. Both the IPS population channels, from the SS involving an indirect transition or from the d-band inhibited by the dipole selection rules, involve a preferential transport of majority (or minority) spin electrons, suggesting a new pathway to control the spin polarization via photon energy. Measurements by using circularly polarized laser pulses or a spin detector could help to discriminate between the two spin-polarizations.

6.4 Conclusions

This chapter presents a detailed 2PPE study of the interface states at the single-layer graphene/Ni(111). In particular, by a theoretical and experimental joint effort we investigate the possibility to optically inject spin-polarized electrons into IPS. Due to the peculiar nature of the IPS, in fact, the possibility to populate such state with spin selected electrons is interesting for the comprehension and the control of spin-polarized transport at the interface, making graphene/Ni(111) a very promising system for spintronic devices.
However, although the violation of the dipole selection rules suggests the possibility that an indirect transition from an occupied surface resonance along the $\overline{\mathrm{KM}}$ path of the band structure to the IPS occurs, a second channel of population of IPS from the minority spin *d*-band must be taken into account. Both the indirect process from SS and the direct process from *d*-band involve a preferential transport of majority (minority) spin electrons, suggesting that is possible, in principle, to inject spin-polarized electrons in IPS.

Chapter 7

Photoinduced electron dynamics at the Porphyrin/Ag Interfaces

Photochemically activated reactions, despite being a powerful tool to covalently stabilize self-organized molecular structures on metallic surfaces, have struggled to take off due to several not yet well understood light-driven processes that can affect the final result. A thorough understanding of the photoinduced charge transfer mechanisms at the organic/metal interface would pave the way to controlling these processes and to developing on-surface photochemistry.
This chapter reports the relaxation processes of the first two excited molecular states at the interface between porphyrin, the essential chromophore in chlorophyll, and two different orientations of the silver surface, Ag(100) and Ag(111), tracked by time-resolved two-photon photoemission measurements. Moreover the possible charge transfer channels between silver substrate and molecules overlayer have been investigated.

7.1 Introduction

Light, like temperature, is able to induce chemical reactions on surfaces for creating ordered and stable covalently linked organic structures such as one- and two-dimensional surface-supported polymers [149–152]. Indeed, although heat treatments are usually employed to trigger on-surface bonding of suitable organic precursors, the light-driven on-surface molecular reactivity is not as developed as the thermally induced counterpart.
The presence of the metallic surface, in addition to the intra- and inter-molecular reactions, provides new photoexcited charge-transfer channels [153, 154], that on one hand can potentially play a key role in tailoring the formation of the long-range ordered covalent framework but on the other hand makes the photoreaction complex and, consequently, the outcomes hardly predictable.
To develop and efficiently use on-surface covalent bonding triggered by photochemical tools, preliminary experiments focused on the study of photoinduced dynamics at the adsorbate/metal interfaces are mandatory in order to understand the role of substrate-mediated indirect photoexcitations in determining the molecular reactivity.
When an organic thin film is in contact with a metal surface, the localized electron system of the organic molecule interacts with inherently delocalized metal bands at the interface. The coupling strength between the two systems governs the energy alignment of the electronic states of the organic molecule with respect to the Fermi level of the metal. Electron transfer processes, static and photoinduced, strongly depend on the energy alignment at the interface [155].

In light of this, a detailed study of the electron transfer at the molecule/metal interface requires a thorough understanding of the energy levels alignment [156–158], which can be considerably hindered by the occurrence of complex processes, including the generation of interface dipoles, static charge transfer, or interface hybridizations, which furthermore become increasingly interwined as the system complexity increases, for example, in metal-supported molecular blends [158, 159].
Photoemission (XPS and UPS) is usually employed to study the electronic structure at the molecule/metal interface, but it cannot give information on the unoccupied levels. Inverse photoemission spectroscopy is often used to obtain the energy of the LUMO, though this approach has limitations in terms of energy

resolution, sample damage, and other factors [158].

Recently, 2PPE measurements, carried out at the phthalocyanine/metal and perylene-3,4,9,10-tetracarboxylic dianhydride (PTCDA)/metal interfaces, has proven to be a powerful technique to investigate the interface states originated by image potential states and Shockley surface states [40, 42, 43, 81, 160, 161]. Moreover, time-resolved two-photon photoemission spectroscopy provides an additional excellent opportunity to investigate both the energy alignment and the ultrafast electron dynamics at the molecule/metal interface [39, 80, 162, 163]. In TR-2PPE measurements, electrons can be excited by a pump pulse from the metal substrate to an unoccupied level of the adsorbed molecules, and then photoemitted by a probe pulse.
In this framework, it is mandatory to clarify that, in systems where the excitonic effects are not negligible, two-photon photoemission has to be considered an effective tool to investigate the occupied and the *excited* rather than the *unoccupied* states. This technique, in fact, similarly to optical measurements, allows one to measure the electronic structure of a system in an out-of-equilibrium situation induced by the laser pump itself.

In this chapter, the energy levels alignment and the electronic dynamics at meso-tetraphenylporphyrin (TPP) film on Ag single crystal in (100) and (111) orientations, investigated by time-resolved non-linear photoemission, are shown. Before depositing TPP films, we have investigated by linear and non-linear photoemission spectroscopy the Ag(100) and Ag(111) substrates. Afterwards, we have tracked the energy level alignment of the HOMO and of the first two excited states with respect to the metal Fermi level by growing several monolayers (ML) thick porphyrin films on Ag(100) and Ag(111) substrates and by subsequently collecting both linear and two-photon photoemission spectra. Moreover, by time-resolved photoemission (in the pump-probe setup), we have investigated the electronic dynamics of the unoccupied excited states and the possible charge transfer processes from Ag to TPP.

7.2 Silver substrates characterization

Polished silver surfaces in (100) and (111) directions have been investigated by linear and non-linear photoemission measurements. Figure 7.1a shows the linear photoemission spectrum collected with a photon energy $h\nu = 6.25$ eV.

No occupied surface states at the $\overline{\Gamma}$ point of the Brillouin zone appears, due to the extension of the *sp*-bands until 1.8 eV above the Fermi level (E_F) [21, 143, 148, 164]. By exciting Ag(100) with a photon energy hν = 3.93 eV (Figure 7.1b) we are also able to observe a sharp feature ascribed to the $n = 1$ Image Potential State (IPS). As expected its binding energy is about 0.45 ± 0.05 eV from the vacuum level [21]. The shoulder at $E - E_F = 5$ eV corresponds to the photoemission from the unoccupied (at equilibrium) *sp*-bands above the Fermi level. The laser pump, as discussed in the following, excites a hot electron population originating the tail at 1.8 eV above the Fermi level. The surface projected electronic structure of Ag(100) at the $\overline{\Gamma}$ point is schematically summarized in the sketch of Figure 7.1c.

Differently from Ag(100), Ag(111) surface projected electronic band structure at the $\overline{\Gamma}$ point of the Brillouin zone has a large band gap of about 4 eV, which extends from a few hundreds meV below the Fermi level, where both an occupied surface state (SS) $n = 0$ and an unoccupied $n = 1$ IPS are localized. In Figure 7.2b the 2PPE spectra collected on Ag(111) by changing the photon energy from 3.63 eV to 4.05 eV are shown. The processes giving rise to the main features are identified by studying the photon energy dependence of the peak positions. By exciting the Ag(111) surface with a photon larger than 3.9 eV (violet curve), we observe a sharp peak at about $E - E_F = 8$ eV due to the photoemission from the IPS, corresponding to a binding energy of 0.6 ± 0.05 eV from the vacuum level, E_V. Moreover, a smaller structure is present, already reported in the literature on Ag(111) [165] and ascribed to an energy pooling process involving two electrons excited above the IPS. By decreasing the pump photon energy down to 3.85 eV, we observe a very intense structure due to the resonant population of the IPS from the occupied SS (light blue spectrum in Figure 7.2b). At lower pump photon energies (3.63 eV, green spectrum in Figure 7.2b), the IPS disappears because the photon is not energetic enough to directly populate the IPS from an occupied state below the E_F, and only the SS, at about 0.1 eV below the E_F, is revealed. The broad structure at about $E - E_F = 5.5$ eV, already observed in the literature [165], is due to photoemission from an unoccupied (at equilibrium) intermediate state at about 1.9 eV above the E_F. The linear photoemission spectrum in Figure 7.2a, collected by using a photon energy hν = 6.25 eV, in addition to the SS at about $E - E_F$=8 eV, shows a structure at about $E - E_F$=5 eV, ascribed to direct optical tran-

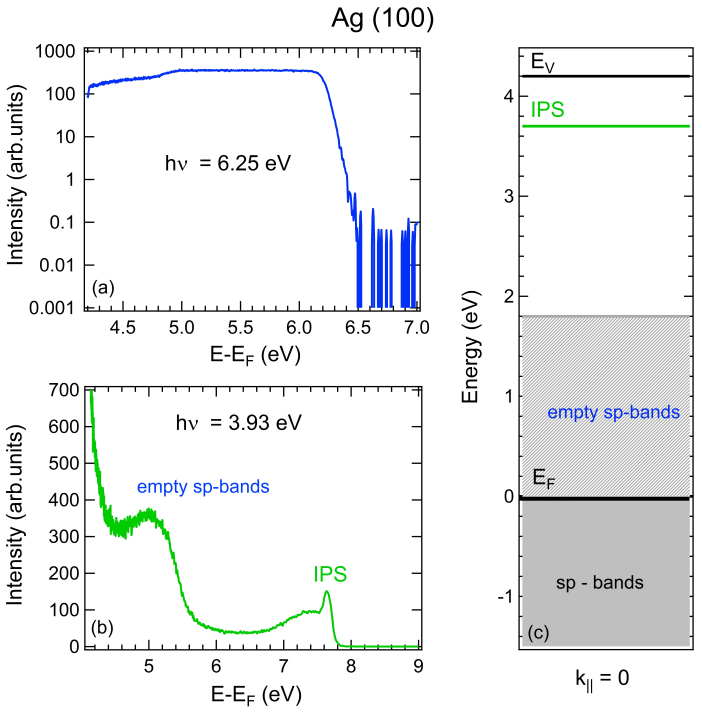

Figure 7.1: (a) Linear photoemission spectrum collected with hν=6.25 eV at normal emission ($k_{||}$=0) on Ag(100). (b) Non-linear photoemission spectrum collected with hν=3.93 eV at $k_{||}$=0 and with *p*-polarized light. (c) Sketch of the Ag(100) electronic structure at the $\overline{\Gamma}$ point of the Brillouin zone as obtained from linear and non-linear photoemission measurements.

sition from the lower to the upper *sp*-bands at $k_{||} \neq 0$. The *sp*-bands along the $\overline{\Gamma L}$ direction have an opposite dispersion leading to the widening of the gap with respect to the center of the Brillouin zone (Figure 7.2c). The surface projected electronic band structure of Ag(111) at the $\overline{\Gamma}$ point of the Brillouin zone is sketched in Figure 7.2c.

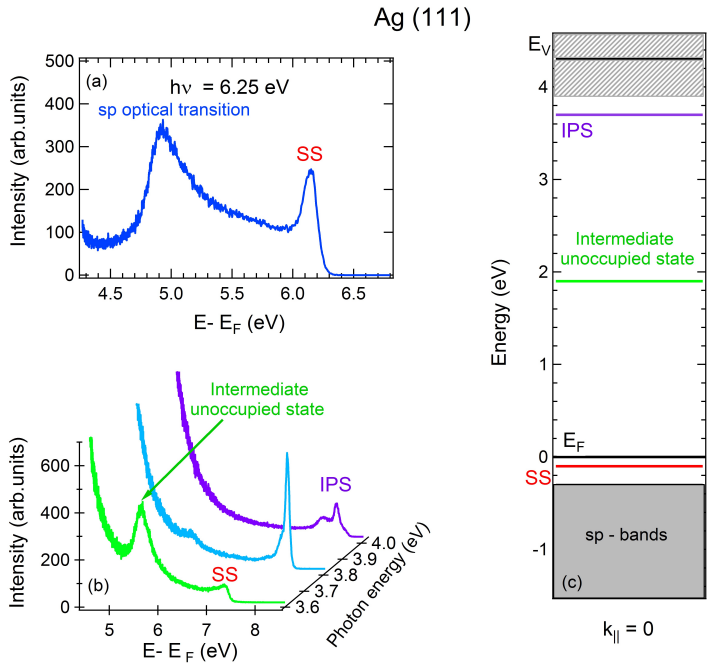

Figure 7.2: (a) Linear photoemission spectrum collected with hν=6.25 eV at normal emission ($k_{\|}$=0) on Ag(111). (b) Non-linear photoemission spectra collected by changing the photon energy from 3.63 eV to 4.05 eV at $k_{\|}$=0 and with p-polarized light. (c) Sketch of the Ag(111) electronic structure at the $\overline{\Gamma}$ point of the Brillouin zone as obtained from linear and non-linear photoemission measurements.

7.3 TPP deposition and calibration

In order to deposit the TPP film on the Ag substrates previously characterized, the following procedure was employed. First, the silver single crystals (10 mm diameter) were cleaned by repeated cycles of 1 keV Ar^+ sputtering and annealing at 820 K and checked for cleanness by means of low energy electron diffraction (LEED). The TPP thin film was prepared by vapor deposition. A ceramic crucible containing TPP powder was resistively heated up to 550 K for different times (from tens of seconds to few minutes). During the deposition

the silver surfaces were kept perpendicular to the crucible flux at a distance of about 5 cm. The crucible was outgassed for a long time to avoid impurities (e.g. solvent residues adsorbed on the TPP powder) during deposition onto the substrate. After TPP deposition the samples were not annealed.

In order to calibrate the thickness of the TPP grown on silver substrates, we have compared the intensity of the Fermi level collected at different TPP deposition times with the Fermi intensity observed for a single layer of TPP on Ag(100). The latter has been achieved by thermal desorption (at about 520 K) of a TPP multilayer deposited on the clean silver substrate. As shown in Figure 7.3, the data (blue dots) are well fitted by a decreasing exponential curve and its intersection with the Fermi intensity for the TPP monolayer (green line) defines that, in our experimental conditions, the deposition time for growing a single TPP layer is 10 seconds. Assuming a linear growth of the TPP layers as a function of the deposition time, we were able to estimate the TPP overlayer thickness. An identical calibration curve has been obtained for TPP deposition on the Ag(111) substrate.

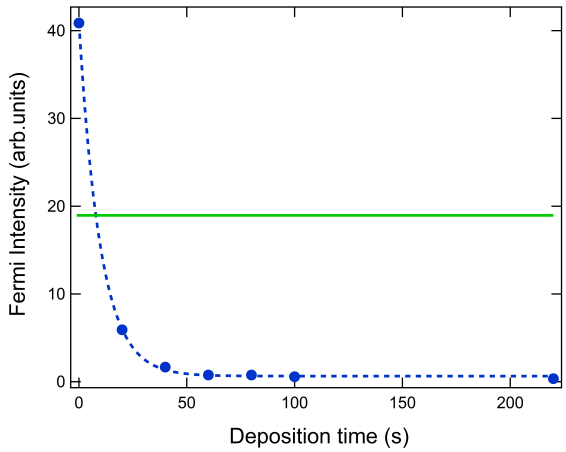

Figure 7.3: Fermi level intensity at TPP/Ag(100) interface for different TPP deposition times (blue dots); the data have been fitted with a decreasing exponential curve. The green line outlines the Fermi intensity for a single-layer of TPP on Ag(100) achieved by thermal desorption of TPP multilayers.

7.4 TPP/Ag(100) and TPP/Ag(111) interfaces

In order to investigate the nature of the TPP molecular states, we have collected non-linear photoemission spectra at different values of the TPP film thickness, from bilayer to 20 layers, deposited on Ag(100) (Figure 7.4a) and Ag(111) (Figure 7.4b). We have chosen two layers of TPP in order to clearly identify all the features ascribed to the TPP film (for a single-layer of TPP, indeed, the molecular features are not detectable) and at the same time to reveal the substrate E_F. The observed spectral features for TPP/Ag(100) and TPP/Ag(111) are fully comparable. On the contrary, significant differences are observed between the thin (2-4 monolayers (ML)) and the thick film (up to 20 ML) of deposited TPP. For all TPP film thicknesses, the occupied state, HOMO-1, and the second unoccupied state, EXC2, are observed at ≈ 2.3 eV below the Ag Fermi level (E_F) and at ≈ 2.1 eV above E_F, respectively. By contrast, a new excited state, labeled EXC1, located at ≈ 1.4 eV below EXC2, appears only for few (2-4 ML) TPP layers.
In a first view, one might assume that upon increasing the TPP thickness, such a feature is energetically shifted to lower kinetic energies, thereby preventing photoemission with a photon energy of about 3.5 eV. Energy shifts at molecule/metal interface can be understood in terms of charge transfer processes [166].

In order to clarify the excitation scheme and to determine the energy level alignment, we have performed linear and two-photon photoemission measurements for the TPP bilayer/Ag interfaces. The linear photoemission spectrum in Figure 7.4c, collected by using a photon energy ($h\nu = 6.2$ eV) larger than the work function, in addition to the Ag Fermi level at $E - E_F = 6.2$ eV shows an occupied state at $E - E_F = 5$ eV (1.3 ± 0.05 eV below E_F), which is absent in the linear spectrum of the clean Ag(100). Because this state is occupied, we have ascribed it to the HOMO state of the TPP film, in agreement with the literature [167].
The HOMO feature is present also in the linear photoemission spectrum of the TPP/Ag(111) interface (Figure 7.4d). In this case, the structure appears more intense and broader than on TPP/Ag(100) due to the contribution of the Ag(111) substrate, i.e. the direct optical transitions from the lower to the upper *sp*-bands (gray dashed line).

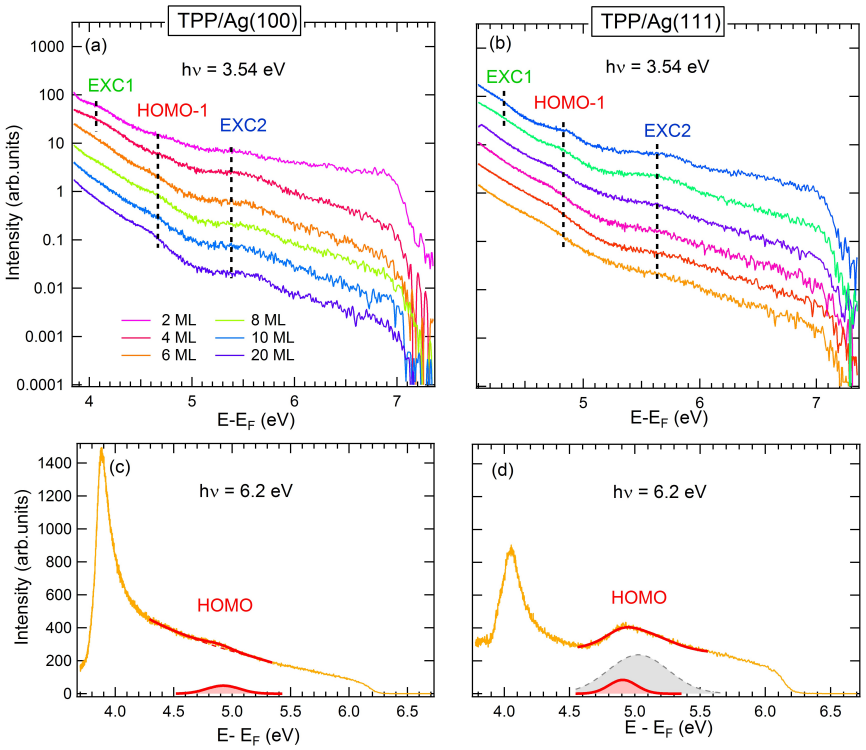

Figure 7.4: Non-linear photoemission spectra collected at h$\nu = 3.54$ eV at $k_{\parallel} = 0$ as a function of the TPP film thickness, ranging from bilayer to 20 layers, deposited on (a) Ag(100) and (b) Ag(111) substrate. (c-d) Linear photoemission spectra collected with h$\nu = 6.2$ eV at $k_{\parallel} = 0$ for the TPP bilayer grown on Ag(100) and Ag(111), respectively. The red Gaussian curves represent the contribution of TPP HOMO orbitals, whereas the gray dashed curve represents the contribution of the silver substrate.

To discriminate the occupied state from the unoccupied one in Figure 7.4a and b, we have collected two-photon photoemission spectra at different pump photon energies (Figure 7.5) and evaluated how the energies of these features shift with the photon energy. In the case of coherent two-photon photoemission from an occupied state, the energy shifts twice as much as the change in photon energy ($\Delta E = 2\Delta h\nu$). On the other hand, in the case of one-photon photoemis-

sion from an intermediate unoccupied state populated by other photoinduced processes, the energy increases linearly with $\Delta h\nu$, i.e $\Delta E = \Delta h\nu$. We underline that the HOMO-1 state, despite being an occupied state, does not appear in the linear photoemission spectrum collected at $h\nu = 6.2$ eV because the photon energy is not sufficient to photoemit electrons directly from this state.

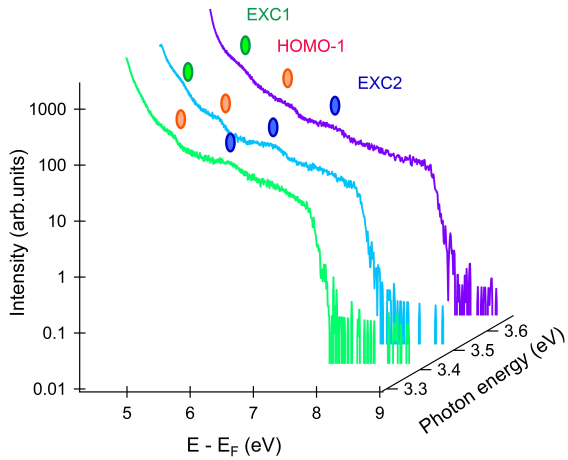

Figure 7.5: Non-linear photoemission spectra collected by tuning the photon energy from 3.35 eV to 3.75 eV, at normal emission ($k_{\parallel}$) and with p-polarized light for the TPP bilayer grown on Ag(111).

The estimated alignment of bilayer-TPP molecular orbitals relative to the Ag Fermi level is sketched in Figure 7.6. As shown in previous works for CoTPP grown on different metal substrates [168], the shift of the vacuum level, E_V, ($\Delta\Phi = 0.55 \pm 0.05$ eV) is the same for both TPP/Ag(100) and TPP/Ag(111) interfaces.
EXC1 and EXC2 states at TPP/Ag(100) are at 0.65 ± 0.05 eV and 2.05 ± 0.05 eV above the Fermi level, respectively; whereas at TPP/Ag(111) they are upshifted of about 100 meV.

To better understand the EXC1 and EXC2 states, we have to compare

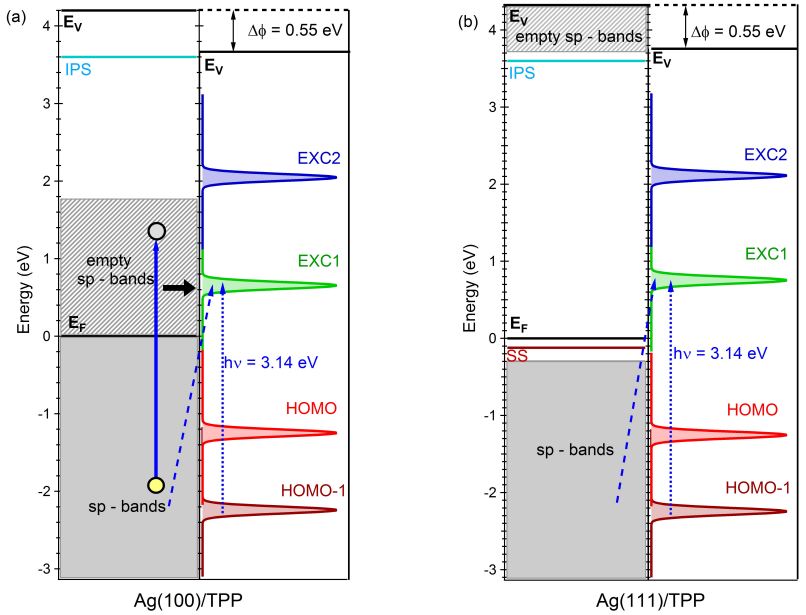

Figure 7.6: Sketch of the energy alignment and of the population processes (blue arrows) of the molecular electronic levels of two layers of TPP with respect to the (a) Ag(100) and (b) Ag(111) electronic structure as obtained from linear and non-linear photoemission measurements. In addition to the occupied (HOMO, HOMO-1) and excited (EXC1, EXC2) molecular orbitals, the characteristic surface states, surface state (SS) and image potential states (IPS) of polished silver surfaces are shown.

the results with the porphyrin UV-vis absorption spectrum, where two well-characterized bands, the Soret or S-band and the Q-band, dominate. Although the S-band is stronger and is generally located between 380 and 450 nm (UV region), the Q-band is typically found between 500 and 650 nm (VIS region) [169,170]. Both of these bands refer to transitions involving the HOMO and LUMO levels. HOMO is a degenerate state with a mixed a_{1u} and a_{2u} symmetry and is delocalized on the porphyrin macrocycle, with little or no weight on the *meso* phenyl rings. Similarly, the unoccupied LUMO is a degenerate state with e_g symmetry and is delocalized on the porphyrin macrocycle. Simple

molecular orbital theory ascribes the Q and S bands to transitions from the ground state to the first and second excited singlet state, respectively: in particular, the Q-band is assigned to ($a_{1u} \rightarrow e_g$) and the S-band to ($a_{2u} \rightarrow e_g$) transitions. The latter, being related to a strongly allowed electronic transition, is more intense than the former in the absorption spectra [171].
Accordingly, the HOMO-EXC2 transition corresponds to the Soret band in the UV energy range, whereas the HOMO- EXC1 transition at about 2 eV corresponds to the Q-band in the VIS region.

As shown in Figure 7.6, EXC2 is localized in the gap of the projected band structure in both TPP/Ag(100) and TPP/Ag(111). EXC1, on the contrary, is localized in the gap in TPP/Ag(111), while it becomes a molecular state/resonance in TPP/Ag(100), where it overlaps the unoccupied *sp*-bands. In order to get insight into the charge transfer processes at the TPP/Ag interface, we have performed time-resolved measurements on the bilayer TPP/Ag system by using a pump-probe setup.

Because EXC1 and EXC2 are detected in the same spectrum using a photon energy of 3.54 eV (Figure 7.4a), we have chosen as probe a photon of 3.54 eV and as pump a photon of 3.14 eV. As highlighted in Figure 7.6, both at TPP/Ag(100) and TPP/Ag(111) interfaces, a photon of 3.14 eV is able to populate EXC1 by the HOMO-EXC1 transition (dotted arrow) and/or by a direct transition from the Ag occupied *sp*-band to EXC1 (dashed arrow). Moreover, only in TPP/Ag(100), a third channel involving an indirect photoinduced electron transfer mediated by the hot electrons excited in the Ag unoccupied *sp*-bands is in principle possible (solid arrow). In fact, in a metal substrate, the absorption of a femtosecond light pulse generates a transient non-equilibrium distribution that thermalizes within the laser pulse duration, due to electron-electron scattering, in a hot electrons distribution with a temperature exceeding the lattice temperature by several thousand kelvin.
The unoccupied *sp*-bands in metallic substrates, as it is known from the literature, represent an optimum cradle to accommodate hot electrons excited by laser pulses in the UV-visible range [148]. The hot electrons can travel to the surface and subsequently be transferred to an unoccupied molecular state. The so-called indirect photoinduced electrons transfer at the metal-molecule interface most often involves the transfer of a hot electron in the metal substrate to the molecular state/resonance [80, 172, 173].

Figure 7.7a shows the spectra collected on TPP/Ag(100) at different delay times between the pump and the probe, along with the spectrum collected by using only the probe pulse. The spectrum collected at 2 ps before the temporal coincidence recalls the spectrum taken using a single laser pulse at 3.54 eV, suggesting that the structures at 4.2 and 5.1 eV are the EXC1 and EXC2 levels, respectively, one-photon-photoemitted from the 3.54 eV laser pulse. Two regions of the spectrum change significantly with the pump-probe delay times: the region immediately below E_F, whose photoemission intensity decreases when the pump and the probe are in temporal coincidence (green line), and the region ascribed to EXC1, whose intensity increases with the decrease of the pump-probe delay time. To better highlight the differences among the spectra taken as a function of the pump-probe delay time, we have first calculated the difference between each spectrum and the one collected out of temporal coincidence ($\tau =$ 2 ps), and we have then divided the result by the out-of-coincidence spectrum ($\tau = 2$ ps) (Figure 7.7b). This method, giving the normalized difference spectra, allows us to estimate the differences on the whole energy range of the spectrum. As previously remarked, the normalized difference spectra differ significantly from zero in the EXC1 region and close to E_F. The small difference perceived at 5.2 eV represents the HOMO photoemitted by absorbing both a 3.54 eV and a 3.14 eV photon.
If one considers that the 3.54 eV photon energy is quasi-resonant with the HOMO-EXC2 transition, this process gives information on the EXC2 relaxation time, that from these measurements appears to be comparable with the laser pulse width (200 fs). The maximum difference is obtained at $\tau = 0$.
The structure at 6.7 eV is E_F photoemitted by absorbing two photons at 3.54 and 3.14 eV. Also, in this case, the dynamics is comparable with the laser pulse width and the maximum difference is at $\tau = 0$ (inset in Figure 7.7b). Because this process is competitive with the photoemission channel from E_F absorbing two photons at 3.54 eV, the result is a decrease of the intensity of the structure at 7 eV, ascribed to this second photoemission channel.

Concerning the photoinduced charge transfer mechanism, the dynamics of the structure at about 4.2 eV, ascribed to the EXC1 level photoemitted by absorbing a photon of 3.54 eV, is of particular relevance. A photon of 3.14 eV is in fact not sufficient to photoemit electrons from the EXC1 level. The difference intensity of this structure is delayed with respect to $\tau = 0$ fs, being

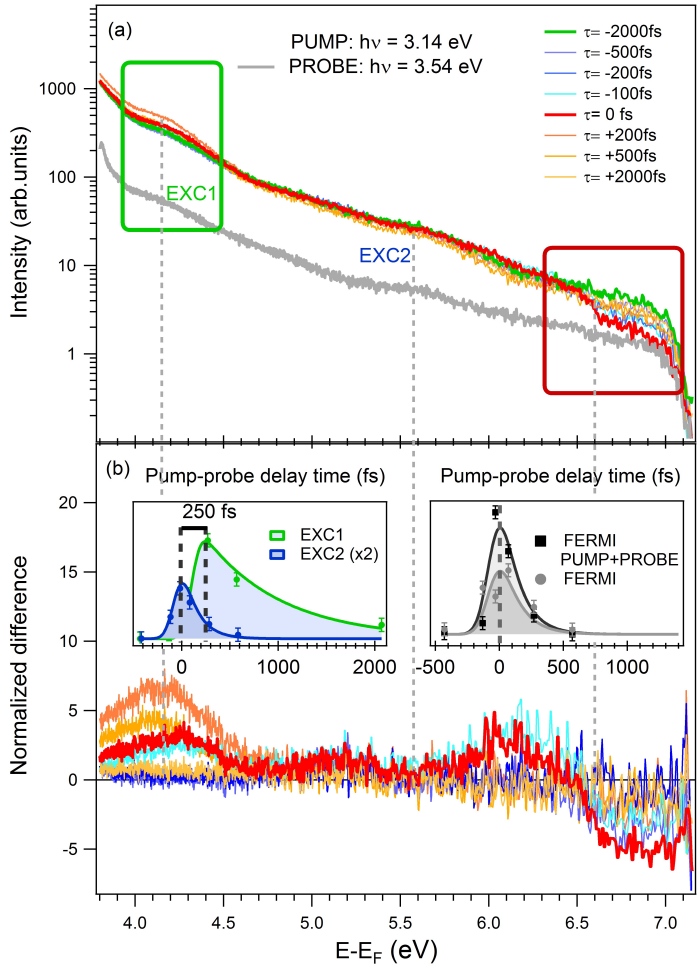

Figure 7.7: (a) Non-linear photoemission spectra collected by using a hν = 3.14 eV photon as the pump and hν = 3.54 eV as the probe at different pump-probe delay times. The spectrum collected with the probe pulse only at 3.54 eV is also reported (gray line). The regions of the spectrum that change with the pump-probe delay are marked with squares. (b) Normalized difference spectra (multiplied by 10) at different pump-probe delay times. Insets show the dynamics of the molecular excited states EXC1 and EXC2 (on the left) and of the Fermi level (on the right) photoemitted by absorbing two photons at 3.54 and 3.14 eV (black line) and by absorbing two photons at 3.54 eV (gray line).

maximum at $\tau = 250$ fs (see inset of Figure 7.7b). Moreover, it has a relaxation time of about 800 fs. The shift of the maximum intensity at 250 fs establishes that electrons are not directly excited from an occupied state of the molecule (HOMO for example) to the EXC1 and then photoemitted by absorbing a 3.54 eV photon, but rather that electrons excited by the pump pulse at 3.14 eV in a state of higher energy relax in EXC1 and are then photoemitted by a photon of 3.54 eV. Being EXC1 a molecular/state resonance with the unoccupied Ag(100) *sp*-bands, it is plausible that the pump excites a hot electrons population in the latter and that a subsequent electron transfer from the Ag *sp*-bands to the TPP EXC1 takes place. The 250 fs delay time for populating EXC1 is the fingerprint that a relaxation process happens before the photoemission process from EXC1 can take place.

In order to confirm this hypothesis, we have performed the same time-resolved measurements at TPP/Ag(111) interface. The spectra collected at different delay times between the pump ($h\nu = 3.14$ eV) and the probe ($h\nu = 3.54$ eV) are shown in Figure 7.8. Only the region of the spectrum ascribed to the EXC1 (in the green square) changes significantly with the pump-probe delay times and reaches the maximum intensity at the temporal coincidence ($\tau = 0$ fs).
The dynamics of the EXC1 level is shown in the inset of Figure 7.8. Similarly to the EXC1 state observed at the TPP/Ag(100) interface, it has a relaxation time of about 800 fs, but differently from the previous case the maximum intensity is not delayed with respect to the pump-probe temporal coincidence. This result confirms that in TPP/Ag(111), where EXC1 is not a molecular/resonance state, it is directly populated by the pump and then photoemitted by the probe, with no indirect charge transfer processes taking place from Ag to TPP at this interface.

As shown in Figure 7.6, the pump photon energy of 3.14 eV is, in fact, able to populate EXC1 directly from the molecular occupied state (HOMO) or from the occupied *sp*-bands of Ag(111). Then, electrons are photoemitted by the probe when it is in temporal coincidence with the pump.
As previously remarked, the EXC1 relaxation time in both cases is about 800 fs, in agreement with the optical measurements reported in the literature and carried out on thick films of TPP or on TPP molecules in solution, where the interaction with the metallic substrate is missing [169, 170]. Here, the excited

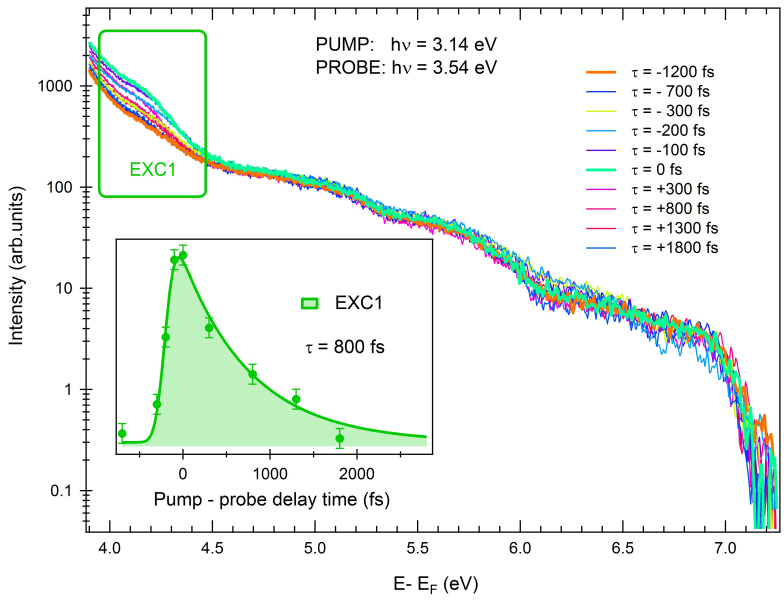

Figure 7.8: Non-linear photoemission spectra collected by using h$\nu = 3.14$ eV photon energy as the pump and h$\nu = 3.54$ eV as the probe at different pump-probe delay times. The region of the spectrum that changes with the pump-probe delay is marked with a green square. In the inset the dynamics of the molecular excited state EXC1 is shown.

TPP first relax from higher to lower vibronic levels (EXC1) and then undergo one of the following processes: (i) the electrons decay from EXC1 to the HOMO in a time of a few picoseconds or less or (ii) an intersystem crossing from the EXC1 to the porphyrin triplet state T1 happens, with a time constant of the order of nanoseconds [170].
With respect to the relaxation scenario obtained by optical measurements, we do not observe any intersystem crossing (ISC) from EXC1 to T1 triplet state. This relaxation channel can in principle be observed with time-resolved photoemission spectroscopy. Recently, ISC has been observed in the photoemission spectra, as a downward shift of the S1 structure along with the comparison to the T1 feature, collected at different delay times at the interface between copper phthalocyanine (CuPc) layers and C_{60} [174–176]. The key point is that in ph-

thalocyanine, the ISC time is of the order of 1 ps, detectable in the femtosecond time scale typical of time-resolved photoemission measurements. In porphyrins, being the ISC $\sim$ 1 ns long, that is, much longer than the laser pulse duration (150 fs), it is possible to assume a vanishing triplet population, thus justifying the absence of any feature ascribed to the T1 level.

7.5 Conclusions

In this chapter, the molecular energy levels alignment at the TPP/Ag interfaces, tracked by non-linear photoemission measurements, have been shown. Moreover, by comparing time-resolved photoemission data carried out on both TPP/Ag(100) and TPP/Ag(111), we can conclude that the presence of unoccupied *sp*-bands in Ag(100), immediately above the Fermi level, provides a new path for the photoinduced charge transfer from the metal to the molecule that takes place within 250 fs. On-surface bond photodissociation reactions triggered by the hot electrons-mediated population of molecular excited states have been postulated both for the O-H and N-H bond breaking in phenol [177] and aniline [152], respectively, in order to explain the substantially lower wavelength able to initiate the reaction if compared to the analogous gas phase experiments [178, 179]. Such photodissociation events are the key step to produce on-surface reactive radicals capable to form intermolecular covalent bonds, thus initiating on-surface 1D and 2D polymerizations. A role of the substrate has been postulated also for on-surface terminal alkyne C-C light-driven coupling (Glaser coupling) [180]. By revealing the important role of the substrate surface orientation in the substrate-mediated photoinduced phenomena, our results provides the means to start verifying quantitatively these assumptions and to study the efficiency of photoinduced indirect, substrate-mediated vs direct intramolecular excitations in determining the outcome of surface reactions in terms of quantum efficiency, reaction rates, structural order and stereochemistry [152].

Chapter 8

Conclusions

The goal of the present thesis is to add important information to the current knowledge about the interaction between carbon-based nanostructures and metal surfaces through the investigation of the electronic properties and dynamics of the electronic states localized in the interfacial region. Such task has been accomplished applying femtosecond, high intensity, laser pulses in the near-UV range to the conventional photoemission techniques. The high intensity coherent pulses induce multi-photons transitions, allowing to investigate, with a high resolution, both the energy region below Fermi level E_F and the energy range between E_F and the vacuum level. Moreover, the electronic relaxation dynamics of the excited electronic states at the interface can be investigated by means of pump-probe experiments.

The interface states of two different carbon-nanostructures/metal systems have been studied in detail: a single-layer of graphene grown on metal and organic-molecules deposited on metallic surfaces. The former interface is classified, on the basis of the interaction strength with the substrate, in weakly and strongly interacting. Among weakly interacting systems graphene/Cu(111) and graphene/Ir(111) interfaces have been studied. The combined experimental and theoretical investigation of the occupied and unoccupied electronic surface states at the first interface suggests that the two observed unoccupied states rise from the hybridization of the $n = 1$ image potential state with a quantum well state. At the second weakly interacting interface, i.e. graphene/Ir(111), instead, in addition to the investigation of the Rashba-type surface state, already reported in literature, experimental evidence of a Rashba effect of the $n = 1$ IPS has been reported. Moreover the relaxation dynamics of the first image potential state have been studied by time-resolved 2PPE.

An interesting case of strongly interacting system and ideal spin filtering is represented by a single-layer graphene grown on Ni(111) surface. By a theoretical and experimental joint effort we have investigated the possibility to optically inject spin-polarized electrons into $n = 1$ IPS. The possibility to populate such state with spin selected electrons is interesting for the comprehension and the control of spin-polarized transport at the interface, making graphene/Ni(111) a very promising system for spintronic devices.
For the latter system, i.e. organic-molecules/metal, we have focused on the relaxation dynamics and photoinduced charge transfer processes at the interface between tetraphenylporphyrin and silver surface in (100) and (111) orientations. By comparing time-resolved photoemission measuraments performed at both the TPP/Ag interfaces, we have proved the possibility of a photoinduced charge transfer between Ag(100) substrate and porphyrins overlayer mediated by the unoccupied *sp*-bands in silver.

8.1 Future Perspectives

The research activity carried out during this thesis work has allow to evaluate the potentialities of time-resolved non-linear photoemission spectroscopy applied to the carbon-based nanostructures on metal surfaces. In the future, harvesting the fruits of this thesis work , we intent to move along two different ways: the graphene/metal interface intercalated with noble metal, on one side, and the molecular donor/acceptor (D/A) complexes on metal surface on the other.

An interesting property of graphene/metal interface is the possibility to control the interaction of graphene overlayer with the metallic substrate by noble metal intercalation. Recently, has been proved [50] that the intercalation of a monolayer of gold between the graphene and the Ni(111) surface, for example, induces the shift of π bands closer to the Fermi level and the electronic decoupling of the graphene from the substrate. On the other side, Ni monolayer intercalated at graphene/Ir(111) interface, leads to a transition from a nearly undisturbed to a strongly hybridized graphene π-band [181]. In this context, we plan to investigate the modifications induced in the electronic properties and dynamics of the interface states when the graphene/metal system is intercalated with different noble metal nanoparticles.

On the other side, molecular donor-acceptor (D-A) interfaces are among the most promising candidates for next generation solar cells based on heterojunction interfaces. An high efficiency organic photovoltaic cell, in fact, require D-A interfaces able to dissociate the excitons, created by optical excitation, and produce free carriers [182]. Specifically, in recent years, fullerene-porphyrin complexes have been extensively studied due to their considerable photoactive and structural properties. Fullerenes, in fact, show extraordinary electron-accepting characteristics, promoting ultrafast charge separation and exhibiting very slow charge recombination characteristics. On the other hand, porphyrins due to their broadband absorption spectrum and ultrafast energy transfer between the macrocycles, are ideal light harvesting units to be combined with electron acceptors as fullerenes [182]. In this framework, we intent to investigate the possible charge transfer processes that occur at Tetraphenylporphyrin / Fullerene (C_{60}) interface deposited on metal surface by means of time resolved two-photon photoelectron spectroscopy.

Bibliography

[1] S. Z. Butler, S. M. Hollen, L. Cao, Y. Cui, J. A. Gupta, H. R. Gutiérrez, T. F. Heinz, S. S. Hong, J. Huang, A. F. Ismach, E. Johnston-Halperin, M. Kuno, V. V. Plashnitsa, R. D. Robinson, R. S. Ruoff, S. Salahuddin, J. Shan, L. Shi, M. G. Spencer, M. Terrones, W. Windl, and J. E. Goldberger. Progress, challenges, and opportunities in two-dimensional materials beyond graphene. *ACS nano*, 7:28982926, 2013.

[2] G. R. Bhimanapati, Z. Lin, V. Meunier, Y. Jung, J. Cha, S. Das, D. Xiao, Y. Son, M. S. Strano, V. R. Cooper, L. Liang, S. G. Louie, E. Ringe, W. Zhou, S. S. Kim, R. R. Naik, B. G. Sumpter, H. Terrones, F. Xia, Y. Wang, J. Zhu, D. Akinwande, N. Alem, J. A. Schuller, R. E. Schaak, M. Terrones, and J. A. Robinson. Recent advances in Two-Dimensional materials beyond graphene. *ACS nano*, 9:1150911539, 2015.

[3] K. S. Novoselov, A. K. Geim, S. V. Morozov, D. Jiang, Y. Zhang, S. V Dubonos, I. V. Grigorieva, and A. A. Firsov. Electric field effect in atomically thin carbon films. *Science*, 306:666–668, 2004.

[4] K. S. Novoselov, D. Jiang, F. Schedin, T. J. Booth, V. V. Khotkevich, S. V. Morozov, and A. K. Geim. Two-dimensional atomic crystals. *Proc. Natl. Acad. Sci. USA*, 102:1045110453, 2005.

[5] A. K. Geim and K. S. Novoselov. The rise of graphene. *Nature Materials*, 6:183–191, 2007.

[6] J. Wintterlin and M. L. Bocquet. Graphene on metal surfaces. *Surf. Sci.*, 603:1841–1852, 2009.

[7] K. S. Novoselov, A. K. Geim, S. V. Morozov, D. Jiang, M. I. Katsnelson, I. V. Grigorieva, S. V. Dubonos, and A. A. Firsov. Two-dimensional gas of massless Dirac fermions in graphene. *Science*, 306:666–668, 2004.

[8] C. Lee, X. D. Wei, J. W. Kysar, and J. Hone. Measurement of the elastic properties and intrinsic strength of monolayer graphene. *Science*, 321:385–388, 2008.

[9] K. S. Novoselov, V. I. Falko, L. Colombo, P. R. Gellert, M. G. Schwab, and K. Kim. A roadmap for graphene. *Nature*, 490:192200, 2012.

[10] S. Hüfner. *Surface Physics: Theoretical models and experimental methods.* Springer, 2003.

[11] M. V. Mamonova, V.V. Prudnikov, and I. A. Prudnikova. *Photoelectron Spectroscopy: Principles and Applications.* CRC press, 2014.

[12] N.V. Ashcroft and N. D. Mermin. *Solid State Physics.* Brooks Cole, 1976.

[13] O. Madelung. *Solid state physics. Localized states,.* Nauka, 1985.

[14] I.E. Tamm. On the possible bound states of electrons on a crystal surface. *Phys. Z. Soviet Union*, 1:733, 1932.

[15] W. Shockley. On the surface states associated with a periodic potential. *Phys.Rev.*, 56:317–323, 1939.

[16] P. M. Echenique and J. B. Pendry. The existence and detection of Rydberg states at surfaces. *J. Phys. C: Solid State Phys.*, 11:2065–2075, 1978.

[17] N. V. Smith. Phase analysis of image states and surface states associated with nearly-free-electron band gaps. *Phys.Rev.B*, 32:3549–3555, 1985.

[18] P. M. Echenique and J. B. Pendry. Theory of image states at metal surfaces. *Progress in Surface Science*, 32:111–173, 1990.

[19] R.M. Osgood and X. Wang. Image states on single-crystal metal surface. *Solid State Physics*, 51:1–80, 1997.

[20] E. G. McRae. Electronic surface resonances of crystals. *Rev. Mod. Phys.*, 51:541–568, 1979.

[21] Th. Fauster and W. Steinmann. *Photonic Probes of Surfaces-Chapter 8.* North-Holland, 1995.

[22] Th. Fauster, C. Reuß, I.L. Shumay, and M. Weinelt. Femtosecond two-photon photoemission studies of image-potential states. *Chem. Phys.*, 251:111–121, 2000.

[23] W. Steinmann. Two-photon photoemission spectroscopy of electronic states at metal surfaces. *Physica Status Solidi (b)*, 192(2):339–356, 1995.

[24] D. Niesner. *Two-photon photoemission studies of graphene and topological insulators.* PhD thesis, Naturwissenschaftlichen Fakultät der Friedrich-Alexander-Universität Erlangen-Nürnberg, 2013.

[25] D. Straub and F. J. Himpsel. Spectroscopy of image-potential states with inverse photoemission. *Phys. Rev. B*, 33:2256–2262, 1986.

[26] S. Yang, K. Garrison, and R. A. Bartynski. Image-potential states on Ni(111) measured by inverse-photoemission spectroscopy. *Phys. Rev. B*, 43:2025–2031, 1991.

[27] V. Dose, W. Altmann, A. Goldmann, U. Kolac, and J. Rogozik. Image-potential states observed by inverse photoemission. *Phys. Rev. Lett.*, 52:1919–1921, 1984.

[28] K. Giesen, F. Hage, F. J. Himpsel, H. J. Riess, and W. Steinmann. Binding energy of image-potential states: Dependence on crystal structure and material. *Phys. Rev. B*, 35:971–974, 1987.

[29] S.S. Jha. Second.-order optical processes and harmonic fields in solids. *Phys.Rev.*, 145:500–506, 1966.

[30] M. Wolf, A. Hotzel, E. Knoesel, and D. Velic. Direct and indirect excitation mechanisms in two-photon photoemission spectroscopy of Cu(111) and CO/Cu(111). *Phys. Rev. B*, 59:5926, 1999.

[31] K. Giesen, F. Hage, F. J. Himpsel, H. J. Riess, and W. Steinmann. Hydrogenic image-potential states: A critical examination. *Phys. Rev. B*, 33:5241–5244, 1986.

[32] H. Ueba and B. Gumhalter. Theory of two-photon photoemission spectroscopy of surfaces. *Progress in Surface Science*, 82:193–223, 2007.

[33] W. Steinmann. Spectroscopy of image-potential states by two-photon photoemission. *Applied Physics*, 49:365–377, 1989.

[34] M. Weinelt, Ch. Reuß, M. Kutschera, U. Thomann, I. L. Shumay, Th. Fauster, U. Höfer, F. Theilmann, and A. Goldmann. Decay and dephasing of image-potential states due to surface defects and disorder. *Appl. Phys. B*, 68:377–381, 1999.

[35] Th. Fauster, M. Weinelt, and U. Höfer. Quasi-elastic scattering of electrons in image-potential states. *Progress in Surface Science*, 82:224–243, 2007.

[36] H.L. Dai. *Laser spectroscopy and photochemistry on metal surfaces*. World Scientific, 1995.

[37] M. Bonn, S. Funk, Ch. Hess, D.N. Denzler, C. Stampfl, M. Scheffler, M. Wolf, and G. Ertl. Phonon- versus electron-mediated desorption and oxidation of CO on Ru(0001). *Science*, 285:1042–1045, 1999.

[38] N.-H. Ge, C.M. Wong, R.L. Lingle Jr, J. D. McNeill, K. J. Gaffney, and C. B. Harris. Femtosecond dynamics of electron localization at interfaces. *Science*, 279:202–205, 1998.

[39] E. V. Chulkov, A. G. Borisov, J. P. Gauyacq, D. Sánchez-Portal, V. M. Silkin, V. P. Zhukov, and P. M. Echenique. Electronic excitations in metals and at metal surfaces. *Chem. Rev.*, 106:4160–4206, 2006.

[40] N. Gonzalez-Lakunza, I. Fernández-Torrente, K. J. Franke, N. Lorente, A. Arnau, and J. I. Pascual. Formation of dispersive hybrid bands at an organic-metal interface. *Phys. Rev. Lett.*, 100:156805–156808, 2008.

[41] J. Ziroff, F. Forster, A. Schöll, P. Puschnig, and F. Reinert. Hybridization of organic molecular orbitals with substrate states at interfaces: PTCDA on silver. *Phys. Rev. Lett.*, 104:233004–233008, 2010.

[42] C. H. Schwalb, S. Sachs, M. Marks, A. Schöll, F. Reinert, E. Umbach, and U. Höfer. Electron lifetime in a Shockley-type Metal-Organic interface state. *Phys. Rev. Lett.*, 101:146801–146804, 2008.

[43] M. C. E. Galbraith, M. Marks, R. Tonner, and U. Höfer. Formation of an organic/metal interface state from a Shockley resonance. *J. Phys. Chem. Lett.*, 5:5055, 2014.

[44] M. Batzill. The surface science of graphene: Metal interfaces, cvd synthesis, nanoribbons, chemical modifications, and defects. *Surf. Sci. Rep.*, 67:83–115, 2012.

[45] A. Dahal and M. Batzill. Graphene-nickel interfaces: a review. *Nanoscale*, 6:2548–2562, 2014.

[46] J. Coraux, A. T. N' Diaye, M. Engler, C. Busse, D. Wall, N. Buckanie, F.-J. M. zu Heringdorf, R. van Gastel, B. Poelsema, and T. Michely. Growth of graphene on Ir(111). *New J. Phys*, 11:023006–023027, 2009.

[47] P. L. Sutter, J. I. Flege, and E. A. Sutter. Epitaxial graphene on Ruthenium. *Nat. Mater.*, 7:406–411, 2008.

[48] N. Armbrust, J. Güdde, P. Jakob, and U. Höfer. Time-resolved two-photon photoemission of unoccupied electronic states of periodically rippled graphene on Ru(0001). *Phys. Rev. Lett.*, 108:056801–056805, 2012.

[49] A. Nagashima, N. Tejima, and C. Oshima. Electronic states of the pristine and alkali-metal-intercalated monolayer graphite/Ni(111) systems. *Phys. Rev. B*, 50:17487–17495, 1994.

[50] A. Varykhalov, J. Sánchez-Barriga, A. M. Shikin, E. Biswas, C.and Vescovo, A. Rybkin, D. Marchenko, and O. Rader. Electronic and magnetic properties of quasi-freestanding graphene on Ni. *Phys. Rev. Lett.*, 101:157601, 2008.

[51] Y. S. Dedkov and M. Fonin. Electronic and magnetic properties of the graphene-ferromagnet interface. *New J. Phys.*, 12:125004, 2010.

[52] A. Varykhalov and O. Rader. Graphene grown on Co(0001) films and islands: Electronic structure and its precise magnetization dependence. *Phys. Rev. B*, 80:035437–035442, 2009.

[53] I. Pletikosić, M. Kralj, P. Pervan, R. Brako, J. Coraux, A. T. N'Diaye, C. Busse, and T. Michely. Dirac cones and minigaps for graphene on Ir(111). *Phys. Rev. Lett.*, 102:056808, 2009.

[54] M. Kralj, I. Pletikosić, M. Petrović, P. Pervan, M. Milun, A. T. N'Diaye, C. Busse, T. Michely, J. Fujii, and I. Vobornik. Graphene on Ir(111) characterized by angle-resolved photoemission. *Phys. Rev. B*, 84:075427–075434, 2011.

[55] C. Jeon, H.-N. Hwang, W.-G. Lee, Y. G. Jung, K. S. Kim, C.-Y. Park, and C.-C. Hwang. Rotated domains in chemical vapor deposition-grown monolayer graphene on Cu(111): an angle-resolved photoemission study. *Nanoscale*, 5:8210–8213, 2013.

[56] A. T. N' Diaye, S. Bleikamp, P. J. Feibelman, and T. Michely. Two-dimensional Ir cluster lattice on a graphene moiré on Ir(111). *Phys. Rev. Lett.*, pages 215501–215504.

[57] D. Nobis, M. Potenz, D. Niesner, and Th. Fauster. Image-potential states of graphene on noble-metal surfaces. *Phys. Rev. B*, 88:195435, 2013.

[58] L. Ma, X. C. Zeng, and J. Wang. Oxygen intercalation of graphene on transition metal substrate: An edge-limited mechanism. *The Journal of Physical Chemistry Letters*, 6(20):4099–4105, 2015.

[59] D. Niesner and Th. Fauster. Image-potential states and work function of graphene. *J. Phys.: Condens. Matter*, 26:393001–393013, 2014.

[60] M. Vanin, J. J Mortensen, A. K. Kelkkanen, J. M. Garcia-Lastra, K. S. Thygesen, and K. W. Jacobsen. Graphene on metals: A van der Waals density functional study. *Phys. Rev. B*, 81:081408–081411, 2010.

[61] M. Hasegawa and K. Nishidate. Transfer doping of a metallic carbon nanotube and graphene on metal surfaces. *Phys. Rev. B*, 83:155435–155445, 2011.

[62] G. G. Giovannetti, P. A. Khomyakov, G. Brocks, V. M. Karpan, J. van den Brink, and P. J. Kelly. Doping graphene with metal contacts. *Phys. Rev. Lett.*, 101:026803–026806, 2008.

[63] P. A. Khomyakov, G. Giovannetti, P. C. Rusu, G. Brocks, J. van den Brink, and P. J. Kelly. First-principles study of the interaction and charge transfer between graphene and metals. *Phys. Rev. B*, 79:195425–195436, 2009.

[64] B. B. Borca, S. Barja, M. Garnica, D. Sánchez-Portal, V. M. Silkin, E. V. Chulkov, C. F. Hermanns, J. J. Hinarejos, A. L. Vázquez de Parga, A. Arnau, P. M. Echenique, and R. Miranda. Potential energy landscape for hot electrons in periodically nanostructured graphene. *Phys. Rev. Lett.*, 105:036804–036807, 2010.

[65] N. Armbrust, J. Güdde, and U. Höfer. Formation of image-potential states at the graphene/metal interface. *New J. Phys*, 17:103043–103052, 2015.

[66] D. Niesner, Th Fauster, J. I. Dadap, N. Zaki, K. R. Knox, P.-C. Yeh, R. Bhandari, R. M. Osgood, and M. Petrović. Trapping surface electrons on graphene layers and islands. *Phys. Rev. B*, 85:081402, 2012.

[67] V. M. Silkin, J. Zhao, F. Guinea, E. V. Chulkov, P. M. Echenique, and H. Petek. Image potential states in graphene. *Phys. Rev. B*, 80:121408–121411, 2009.

[68] E. V. Chulkov, V. M. Silkin, and P. M. Echenique. Image potential states on metal surfaces: binding energies and wave functions. *Surf. Sci.*, 437:330–352, 1999.

[69] H. G. Zhang, H. Hu, Y. Pan, J. H. Mao, M. Gao, H. M. Guo, S. X. Du, T. Greber, and H.-J. Gao. Graphene based quantum dots. *J. Phys.: Condens. Matter*, 22:302001–302004, 2010.

[70] A. T N'Diaye, J. Coraux, T. N Plasa, C. Busse, and T. Michely. Structure of epitaxial graphene on Ir(111). *New J. Phys.*, 10:043033, 2008.

[71] F. Jean, T. Zhou, N. Blanc, R. Felici, J. Coraux, and G. Renaud. Topography of the graphene/Ir(111) moiré studied by surface x-ray diffraction. *Phys. Rev. B*, 91:245424–245430, 2015.

[72] A. L. A. L. Vàzquez de Parga, F. Calleja, B. Borca, M. C. G. Passeggi Jr., J. J. Hinarejos, F. Guinea, and R. Miranda. Periodically rippled graphene: Growth and spatially resolved electronic structure. *Phys. Rev. Lett.*, 100:056807–056810, 2008.

[73] W. Moritz, B. Wang, M.-L. Bocquet, T. Brugger, T. Greber, J. Wintterlin, and S. Günther. Structure determination of the coincidence phase of graphene on Ru(0001). *Phys. Rev. Lett.*, 104:136102–136105, 2010.

[74] P. V. Kamat. Photochemistry on nonreactive and reactive (semiconductor) surfaces. *Chem. Rev.*, 93:267–300, 1993.

[75] X.-L. Zhou, X.-Y. Zhu, and J. M. White. Photochemistry at adsorbate/metal interfaces. *Surface science reports*, 13:73–220, 1991.

[76] S. Günes, H. Neugebauer, and N. S. Sariciftci. Conjugated polymer-based organic solar cells. *Chem. Rev.*, 107:1324–1338, 2007.

[77] M. Galperin and A. Nitzan. Current-induced light emission and light-induced current in molecular-tunneling junctions. *Phys. Rev. Lett.*, 95(20):206802–206805, 2005.

[78] G. P. Brivio and M.I. Trioni. The adiabatic moleculemetal surface interaction: Theoretical approaches. *Reviews of Modern Physics*, 71:1231, 1991.

[79] D. M. Newns. Self-consistent model of hydrogen chemisorption. *Phys. Rev.*, 178:1123–1135, 1969.

[80] C. D. Lindstrom and X.-Y. Zhu. Photoinduced electron transfer at molecule-metal interfaces. *Chem. Rev.*, 106:4281–4300, 2006.

[81] B.W. Caplins, D. E. Suich, A. J. Shearer, and C. B. Harris. Metal/phthalocyanine hybrid interface states on Ag(111). *J. Phys. Chem. Lett.*, 5:16791684, 2014.

[82] S. Sachs, C. H. Schwalb, M. Marks, A. Schöll, F. Reinert, E. Umbach, and U. Höfer. Electronic structure at the perylenetetracarboxylic Acid Dianhydride/Ag(111) interface studied with two-photon photoelectron spectroscopy. *J. Chem. Phys.*, 131:144701, 2009.

[83] A. Yang, S. Shipman, S. Garrett-Roe, J. Johns, M. Strader, P. Szymanski, E. Muller, and C. Harris. Two-photon photoemission of ultrathin film PTCDA morphologies on Ag(111). *J. Phys. Chem. C*, 112:2506–2513, 2008.

[84] P. S. Kirchmann, P. A. Loukakos, U. Bovensiepen, and M. Wolf. Ultrafast electron dynamics studied with time-resolved two-photon photoemission: intra- and interband scattering in C_6F_6/Cu(111). *New Journal of Physics*, 7:113, 2005.

[85] P. J. Rous. Negative ion formation in adsorbed molecules: The role of surface states. *Phys. Rev. Lett.*, 74:1835–1838, 1995.

[86] Y. Gogotsi, J. A. Libera, N. Kalashnikov, and M. Yoshimura. Graphite polyhedral crystals. *Science*, 290:317–320, 2000.

[87] A. C. Ferrari. Raman spectroscopy of graphene and graphite: Disorder, electron-phonon coupling, doping and non-adiabatic effects. *Solid State Communications*, 143:47–57, 2007.

[88] J. D. Wood, S. W. Schmucker, A.S. Lyons, E. Pop, and J. W. Lyding. Effects of polycrystalline Cu substrate on graphene growth by chemical vapor deposition. *Nano Lett.*, 11:4547–4554, 2011.

[89] A. Das, S. Pisana, B. Chakraborty, S. Pisacane, S. K. Saha, U. V. Waghmare, K. S. Novoselov, H. R. Krishnamurthy, A. K. Geim, A. C. Ferrari, and A. K. Sood. Monitoring dopants by Raman scattering in an electrochemically top-gated graphene transistor. *Nature Nanotechnology*, 3:210–215, 2008.

[90] S. Pagliara, M. Montagnese, S. Dal Conte, G. Galimberti, G. Ferrini, and F. Parmigiani. Insight on the interaction between image potential state and π bands in graphite. *Phys. Rev. B*, 87:045427, 2013.

[91] S. Caravati, G. Butti, G. P. Brivio, M. I. Trioni, S. Pagliara, G. Ferrini, G. Galimberti, E. Pedersoli, C. Giannetti, and F. Parmigiani. Cu(111) and Cu(001) surface electronic states. comparison between theory and experiment. *Surf. Sci.*, 600:3901–3905, 2006.

[92] S. Pagliara, G. Ferrini, G. Galimberti, E. Pedersoli, C. Giannetti, and F. Parmigiani. Angle resolved photoemission study of image potential states and surface states on Cu(111). *Surf. Sci.*, 600:4290–4293, 2006.

[93] S. Pagliara, G. Ferrini, G. Galimberti, E. Pedersoli, C. Giannetti, C. A. Rozzi, and F. Parmigiani. Light tuning of the image potential state electron-electron interactions. *Surf. Sci.*, 602:2983–2988, 2008.

[94] P. P. Süle, M. Szendro, C. Hwang, and L. Tapaszt. Rotation misorientated graphene moiré superlattices on Cu(111): Classical molecular dynamics simulations and scanning tunneling microscopy studies. *Carbon*, 77:1082–1089, 2014.

[95] E. Starodub, A. Bostwick, L. Moreschini, S. Nie, F. El Gabaly, K. F. McCarty, and E. Rotenberg. In-plane orientation effects on the electronic structure, stability, and Raman scattering of monolayer graphene on Ir(111). *Phys. Rev. B*, 83:125428–125436, 2011.

[96] G. Grosso and G. Pastori Parravicini. *Solid State Physics, 2nd ed.* Academic Press, 2014.

[97] U. Fano. Effects of configuration interaction on intensities and phase shifts. *Phys. Rev.*, 124:1866–1878, 1961.

[98] A. E. Miroshnichenko, S. Flach, and Y. S. Kivshar. Fano resonances in nanoscale structures. *Rev. Mod. Phys.*, 82:2257–2298, 2010.

[99] C. Ott, A. Kaldun, P. Raith, K. Meyer, M. Laux, J. Evers, C.H. Keitel, C.H. Greene, and T. Pfeifer. Lorentz meets Fano in spectral line shapes: A universal phase and its laser control. *Science*, 340:716–720, 2013.

[100] S. Gottardi, K. Muller, L. Bignardi, J. C. Moreno-López, T. A. Pham, O. Ivashenko, M. Yablonskikh, A. Barinov, J. Bjork, P. Rudolf, , and M. Stohr. Comparing graphene growth on Cu(111) versus oxidized Cu(111). *Nano Lett.*, 15:917–922, 2015.

[101] S. Achilli, M.I. Trioni, E. V. Chulkov, P. M. Echenique, V. Sametoglu, N. Pontius, A. Winkelmann, A. Kubo, J. Zhao, and H. Petek. Spectral properties of Cs and Ba on Cu(111) at very low coverage: Two-photon

photoemission spectroscopy and electronic structure theory. *Phys. Rev. B*, 80:245419–245426, 2009.

[102] S. Achilli, M.I. Trioni, and G. P. Brivio. Detailed features of the surface electronic states of K/Cu(111) by density functional theory. *Phys. Rev. B*, 81:165444–165449, 2010.

[103] E. I. Rashba. Properties of semiconductors with an extremum loop I. cyclotron and combinational resonance in a magnetic field perpendicular to the plane of the loop. *Sov. Phys. Solid State*, 2:1109, 1960.

[104] G. Dresselhaus. Spin-orbit coupling effects in zinc blende structures. *Phys. Rev.*, 100:580, 1955.

[105] M. Heide, G. Bihlmayer, Ph. Mavropoulos, A. Bringer, and S. Blügel. Spin-orbit driven physics at surfaces. Ψ_k *Newsletter*, 78:1, 2006.

[106] R. Winkler. *Spin-Orbit Coupling Effects in Two-Dimensional Electron and Hole Systems*, volume 191 of *Springer Tracts in Modern Physics*. Springer, Berlin, 2003.

[107] S. LaShell, B. A. McDougall, and E. Jensen. Spin splitting of an Au(111) surface state band observed with angle resolved photoelectron spectroscopy. *Phys. Rev. Lett.*, 77:3419, 1996.

[108] M. Hoesch, M. Muntwiler, V. N. Petrov, M. Hengsberger, L. Patthey, M. Shi, M. Falub, T. Greber, and J. Osterwalder. Spin structure of the Shockley surface state on Au(111). *Phys. Rev. B*, 69:241401(R), 2004.

[109] A. Varykhalov, D. Marchenko, M. R. Scholz, E. D. L. Rienks, T. K. Kim, G. Bihlmayer, J. Sánchez-Barriga, and O. Rader. Ir(111) surface state with Giant Rashba splitting persists under graphene in air. *Phys. Rev. Lett.*, 108:066804–5, 2012.

[110] J. R. McLaughlan, E. M. Llewellyn-Samuel, and S. Crampin. Spinorbit splitting of image states. *J. Phys.: Condens. Matter*, 16:6841, 2004.

[111] J.-Y. Bigot, M. Vomir, and E. Beaurepaire. Coherent ultrafast magnetism induced by femtosecond laser pulses. *Nat. Phys.*, 5:515, 2009.

[112] T. Li, A. Patz, L. Mouchliadis, J. Yan, T. A. Lograsso, I. E. Perakis, and J. Wang. Femtosecond switching of magnetism via strongly correlated spincharge quantum excitations. *Nature*, 496:69, 2013.

[113] Taisuke Ohta, Aaron Bostwick, J. L. McChesney, Thomas Seyller, Karsten Horn, and Eli Rotenberg. Interlayer interaction and electronic screening in multilayer graphene investigated with angle-resolved photoemission spectroscopy. *Phys. Rev. Lett.*, 98:206802, 2007.

[114] J. Sánchez-Barriga, G. Bihlmayer, D. Wortmann, D. Marchenko, O. Rader, and A. Varykhalov. Effect of structural modulation and thickness of a graphene overlayer on the binding energy of the Rashba-type surface state of Ir(111). *New J. Phys.*, 15:115009, 2013.

[115] M. R. Scholz, J. Sánchez-Barriga, J. Braun, D. Marchenko, A. Varykhalov, M. Lindroos, Yung Jui Wang, Hsin Lin, A. Bansil, J. Minár, H. Ebert, A. Volykhov, L. V. Yashina, and O. Rader. Reversal of the circular dichroism in angle-resolved photoemission from Bi_2Te_3. *Phys. Rev. Lett.*, 110:216801, May 2013.

[116] C. Cacho, A. Crepaldi, M. Battiato, J. Braun, F. Cilento, M. Zacchigna, M. C. Richter, O. Heckmann, E. Springate, Y. Liu, S. S. Dhesi, H. Berger, Ph. Bugnon, K. Held, M. Grioni, H. Ebert, K. Hricovini, J. Minár, and F. Parmigiani. Momentum-resolved spin dynamics of bulk and surface excited states in the topological insulator Bi_2Se_3. *Phys. Rev. Lett.*, 114:097401, Mar 2015.

[117] G. Bihlmayer, Y. M. Koroteev, P. M. Echenique, E. V. Chulkov, and S. Blügel. The Rashba-effect at metallic surfaces. *Surf. Sci.*, 600:3888, 2006.

[118] H. Bentmann and F. Reinert. Enhancing and reducing the Rashba-splitting at surfaces by adsorbates: Na and Xe on Bi/Cu(111). *New J. Phys.*, 15:115011, 2013.

[119] P. Hohenberg and W. Kohn. Inhomogeneous electron gas. *Phys. Rev.*, 136:B864–B871, Nov 1964.

[120] J. M. Soler, E. Artacho, J. D. Gale, A. García, J. Junquera, P. Ordejón, and D. Snchez-Portal. The Siesta method for ab initio order-n materials simulation. *J. Phys.: Condens. Matter*, 14:2745–2779, 2002.

[121] J. P. Perdew, K. Burke, and M. Ernzerhof. Generalized gradient approximation made simple. *Phys. Rev. Lett.*, 77:3865–3868, Oct 1996.

[122] M. Nagano, A. Kodama, T. Shishidou, and T. Oguchi. A first-principles study on the Rashba effect in surface systems. *J. Phys. Condens. Matter*, 21:064239, 2009.

[123] S. Achilli, S. Caravati, and M. I. Trioni. Ultrathin Fe film on Cu(001): Exchange splitting of image states from first principles. *Surface Science*, 601:4048–4052, 2007.

[124] Ch. Reuß, I. L. Shumay, U. Thomann, M. Kutschera, M. Weinelt, Th. Fauster, and U. Höfer. Control of the dephasing of image-potential states by CO adsorption on Cu(100). *Phys. Rev. Lett.*, 82:153–156, 1999.

[125] K. Boger, M. Roth, M. Weinelt, Th. Fauster, and P.-G. Reinhard. Linewidths in energy-resolved two-photon photoemission spectroscopy. *Phys. Rev. B*, 65:075104, 2002.

[126] T. Hertel, E. Knoesel, M. Wolf, and G. Ertl. Ultrafast electron dynamics at Cu(111): Response of an electron gas to optical excitation. *Phys. Rev. Lett.*, 76:535–538, 1996.

[127] R. Loudon. *The Quantum Theory of Light*. Oxford University Press, 1983.

[128] J. Maassen, W. Ji, and H. Guo. Graphene spintronics: The role of ferromagnetic electrodes. *Nano Lett.*, 11:151–155, 2011.

[129] V. M. Karpan, G. Giovannetti, P. A. Khomyakov, M. Talanana, A. A. Starikov, M. Zwierzycki, J. van den Brink, G. Brocks, and P. J. Kelly. Graphite and graphene as perfect spin filters. *Phys. Rev. Lett.*, 99:176602, 2007.

[130] V. M. Karpan, P. A. Khomyakov, A. A. Starikov, G. Giovannetti, M. Zwierzycki, M. Talanana, G. Brocks, J. van den Brink, and P. J.

Kelly. Theoretical prediction of perfect spin filtering at interfaces between close-packed surfaces of Ni or Co and graphite or graphene. *Phys. Rev. B*, 78:195419, 2008.

[131] Dmitry Usachov, Alexander Fedorov, Mikhail M. Otrokov, Alla Chikina, Oleg Vilkov, Anatoly Petukhov, Artem G. Rybkin, Yury M. Koroteev, Evgueni V. Chulkov, Vera K. Adamchuk, Alexander Grüneis, Clemens Laubschat, and Denis V. Vyalikh. Observation of single-spin Dirac fermions at the graphene/ferromagnet interface. *Nano Lett.*, 15:2396–2401, 2015.

[132] A. Varykhalov, D. Marchenko, J. Sánchez-Barriga, M. R. Scholz, B. Verberck, B. Trauzettel, T. O. Wehling, C. Carbone, and O. Rader. Intact Dirac cones at broken sublattice symmetry: Photoemission study of graphene on Ni and Co. *Phys. Rev. X*, 2:041017, 2012.

[133] E. Voloshina and Y. Dedkov. Graphene on metallic surfaces: problems and perspectives. *Phys. Chem. Chem. Phys.*, 14:13502–13514, 2012.

[134] W.-B. Zhang, C. Chen, and P.-Y. Tang. First-principles study for stability and binding mechanism of graphene/Ni(111) interface: Role of vdW interaction. *J. Chem. Phys.*, 141:044708, 2014.

[135] G. Bertoni, L. Calmels, A. Altibelli, and V. Serin. First-principles calculation of the electronic structure and eels spectra at the graphene/Ni(111) interface. *Phys. Rev. B*, 71:075402, 2005.

[136] W. Han, R. K. Kawakami, M. Gmitra, and J. Fabian. Graphene spintronics. *Nature Nanotech.*, 9:794–807, 2014.

[137] J. Rioux and G. Burkard. Photoinduced pure spin-current injection in graphene with Rashba spin-orbit interaction. *Phys. Rev. B*, 90:035210, 2014.

[138] T. Taniyama, E. Wada, M. Itoh, and M. Yamaguchi. Electrical and optical spin injection in ferromagnet/semiconductor heterostructures. *NPG Asia Mater.*, 3:65–73, 2011.

[139] A. Winkelmann, F. Bisio, R. Ocanã, W.-C. Lin, M. N'yvlt, H. Petek, and J. Kirschner. Ultrafast optical spin injection into image-potential states of Cu(001). *Phys. Rev. Lett.*, 98:226601, 2007.

[140] W.-C. Lin, A. Winkelmann, C. T. Chiang, F. Bisio, and J. Kirschner. Spin-polarized multi-photon photoemission and surface electronic structure of Cu(001). *New J. Phys.*, 12:083022, 2010.

[141] L.L. Patera, C. Africh, R.S. Weatherup, R. Blume, S. Bhardwaj, C. Castellarin-Cudia, A. Knop-Gericke, R. Schloegl, G. Comelli, S. Hofmann, and C. Cepek. In situ observations of the atomistic mechanisms of ni catalyzed low temperature graphene growth. *ACS Nano*, 7:7901, 2013.

[142] A. Grüneis, K Kummer, and D. V. Vyalikh. Dynamics of graphene growth on a metal surface: a time-dependent photoemission study. *New J. Phys.*, 11(7):073050, 2009.

[143] S. Schuppler, N. Fischer, W. Steinmann, R. Schneider, and E. Bertel. Image-potential states on Ni(111): A two-photon-photoemission study. *Phys. Rev. B*, 42:9403, 1990.

[144] F. Bianchini, L.L. Patera, M. Peressi, C. Africh, and G. Comelli. Atomic scale identification of coexisting graphene structures on Ni(111). *J. Phys. Chem. Lett.*, 5:467473, 2014.

[145] P. Hohenberg and W. Kohn. *Phys. Rev.*, 136:B864, 1964.

[146] A. Garcia-Lekue, T. Balashov, M. Olle, G. Ceballos, A. Arnau, P. Gambardella, D. Sánchez-Portal, and A. Mugarza. Spin-dependent electron scattering at graphene edges on Ni(111). *Phys. Rev. Lett.*, 112:066802, 2014.

[147] S. Y. Zhou, G.-H. Gweon, C. D. Spataru, J. Graf, D.-H. Lee, S. G. Louie, and A. Lanzara. Coexistence of sharp quasiparticle dispersions and disorder features in graphite. *Phys. Rev. B*, 71:161403, 2005.

[148] G. Ferrini, C. Giannetti, G. Galimberti, S. Pagliara, D. Fausti, F. Banfi, and F. Parmigiani. Violation of the electric-dipole selection rules in indirect multiphoton excitation of image-potential states on Ag(100). *Phys. Rev. Lett.*, 92:256802, 2004.

[149] Y.-H. Qiao, Q.-D. Zeng, S.-D. Tan, Z.-Y.and Xu, D. Wang, C. Wang, L.-J. Wan, and C.-L. Bai. Photoinduced organic nanowires from self-assembled monolayers. *J. Vac. Sci. Technol., B: Microelectron. Process. Phenom.*, 20:2466–2469, 2002.

[150] D. Heim, D. Écija, K. Seufert, W. Auwärter, C. Aurisicchio, C. Fabbro, D. Bonifazi, and J. V. Barth. Self-assembly of flexible one-dimensional coordination polymers on metal surfaces. *J. Am. Chem. Soc.*, 132:6783–6790, 2010.

[151] Y. Yang and C. Wang. Hierarchical construction of self-assembled low-dimensional molecular architectures observed by using scanning tunneling microscopy. *Chem. Soc. Rev.*, 38:2576–2589, 2009.

[152] A. Basagni, L. Colazzo, F. Sedona, M. DiMarino, T. Carofiglio, E. Lubian, D. Forrer, A. Vittadini, M. Casarin, A. Verdini, and et al. Stereoselective photopolymerization of tetraphenylporphyrin derivatives on Ag(110) at the sub-monolayer level. *Chem. - Eur. J.*, 20:14296–14304, 2014.

[153] X.-Y. Zhu and J. M. White. The role of direct and substrate excitation in ultraviolet photolysis of Phosgene on Pt(111). *J. Chem. Phys.*, 94:1555–1563, 1991.

[154] X. L. Zhou, X.-Y. Zhu, and J. M. White. Photodissociation of intra-adsorbate bonds at adsorbate-metal interfaces. *Acc. Chem. Res.*, 23:327–332, 1990.

[155] D. Ino, K. Watanabe, N. Takagi, and Y. Matsumoto. Electronic structure and femtosecond electron transfer dynamics at noble Metal/tris-(8-hydroxyquinoline) Aluminum interfaces. *Phys. Rev. B: Condens. Matter Mater. Phys.*, 71:1–10, 2005.

[156] S. Braun, W. R. Salaneck, and M. Fahlman. Energy-level alignment at Organic/Metal and Organic/Organic interfaces. *Adv. Mater.*, 21:1450–1472, 2009.

[157] J. C. Scott. Metal/Organic interface and charge injection in organic electronic devices. *J. Vac. Sci. Technol., A*, 21:521–531, 2003.

[158] H. Ishii, K. Sugiyama, E. Ito, and K. Seki. Energy level alignment and interfacial electronic structures at Organic/Metal and Organic/ Organic interfaces. *Adv. Mater.*, 11:605–625, 1999.

[159] A. El-Sayed, P. Borghetti, E. Goiri, C. Rogero, L. Floreano, G. Lovat, D. J. Mowbray, J. L. Cabellos, Y. Wakayama, A. Rubio, and et al. Understanding energy-level alignment in Donor-Acceptor/ metal interfaces from core-level shifts. *ACS Nano*, 7:6914–6920, 2013.

[160] A. Scheybal, K. Müller, R. Bertschinger, M. Wahl, A. Bendounan, P. Aebi, and T. Jung. Modification of the Cu(110) Shockley surface state by an adsorbed pentacene monolayer. *Phys. Rev. B*, 79:115406–115411, 2009.

[161] B. W. Heinrich, L. Limot, M. V. Rastei, C. Iacovita, J.P. Bucher, D. M. Djimbi, C. Massobrio, and M. Boero. Dispersion and localization of electronic states at a ferrocene/Cu(111) interface. *Phys. Rev. Lett.*, 107:216801–216805, 2011.

[162] C. Frischkorn and M. Wolf. Femtochemistry at metal surfaces: Nonadiabatic reaction dynamics. *Chem. Rev.*, 106:42074233, 2006.

[163] M. R. Wasielewski. Energy, charge, and spin transport in molecules and self-assembled nanostructures inspired by photosynthesis. *J. Org. Chem.*, 71:50515066, 2006.

[164] I. Shumay, U. Höfer, C. Reuß, U. Thomann, W. Wallauer, and T. Fauster. Lifetimes of image-potential states on Cu(100) and Ag(100) measured by femtosecond Time-Resolved two-photon photoemission. *Phys. Rev. B*, 58:13974–13981, 1998.

[165] K. Giesen, F. Hage, F. J. Himpsel, H. J. Riess, and W. Steinmann. Two-photon photoemission via image-potential states. *Phys. Rev. Lett.*, 55:300–303, 1985.

[166] F. Petraki, H. Peisert, U. Aygul, F. Latteyer, J. Uihlein, A. Vollmer, and T. Chasse. Electronic structure of FePc and interface properties on Ag(111) and Au(100). *J. Phys. Chem. C*, 116:11110–11116, 2012.

[167] S. Coh. *Electronic Structure and Binding Geometry of Tetraphenylporphyrin-derived Molecules Adsorbed on Metal and Metal Oxide Surfaces. Ph.D. Dissertation.* Rutgers University, 2012.

[168] W. Auwärter, K. Seufert, F. Klappenberger, J. Reichert, A. Weber-Bargioni, A. Verdini, D. Cvetko, M. DellAngela, L. Floreano, A. Cossaro, and et al. Site-specific electronic and geometric interface structure of Co-Tetraphenyl-Porphyrin layers on Ag(111). *Phys. Rev. B*, 81:1–14, 2010.

[169] R. N. Sampaio, W. R. Gomes, D. M. S. Araujo, A. E. H. Machado, R. A. Silva, A. Marletta, I. E. Borissevitch, A. S. Ito, L. R. Dinelli, A. A. Batista, and et al. Investigation of ground- and excited-state photophysical properties of 5,10,15,20-tetra(4-pyridyl)-21h,23h porphyrin with Ruthenium outlying complexes. *J. Phys. Chem. A*, 116:18–26, 2012.

[170] N. M. Barbosa Neto, L. De Boni, C. R. Mendonca, L. Misoguti, S. L. Queiroz, L. R. Dinelli, A. A. Batista, and S. C. Zilio. Nonlinear absorption dynamics in Tetrapyridyl Metalloporphyrins. *J. Phys. Chem. B*, 109:17340–17345, 2005.

[171] M. S. Liao and S. Scheiner. Electronic structure and bonding in metal porphyrins, metal = Fe, Co, Ni, Cu, Zn. *J. Chem. Phys.*, 117:205–219, 2002.

[172] H. Petek and S. Ogawa. Femtosecond time-resolved two-photon photoemission studies of electron dynamics in metals. *Prog. Surf. Sci.*, 56:239–310, 1997.

[173] P. M. Echenique, R. Berndt, E. V. Chulkov, T. Fauster, A. Goldmann, and U. Höfer. Decay of electronic excitations at metal surfaces. *Surf. Sci. Rep.*, 52:219–317, 2004.

[174] G. J. Dutton, W. Jin, J. E. Reutt-Robey, and S. W. Robey. Ultrafast charge-transfer processes at an oriented Phthalocyanine/C_{60} interface. *Phys. Rev. B*, 82:073407–073410, 2010.

[175] G. J. Dutton and S. W. Robey. Exciton dynamics at CuPc/C_{60} interfaces: Energy dependence of exciton dissociation. *J. Phys. Chem. C*, 116:19173–19181, 2012.

[176] G. J. Dutton and S. W. Robey. Distance dependence of exciton dissociation at a Phthalocyanine-C_{60} interface. *J. Phys. Chem. C*, 117:25414–25423, 2013.

[177] J. Lee, S. Ryu, J. S. Ku, and S. K. Kim. Charge transfer photodissociation of Phenol on Ag(111). *J. Chem. Phys.*, 115:10518–10524, 2001.

[178] V. Poterya, L. Šištík, P. Slavíček, and M. Fárník. Hydrogen bond dynamics in the excited states: photodissociation of Phenol in clusters. *Physical chemistry chemical physics : PCCP*, 14:8936–8944, 2012.

[179] Graeme A. King, Thomas A. A. Oliver, and Michael N. R. Ashfold. Dynamical insights into $\pi 1\sigma^*$ state mediated photodissociation of aniline. *The Journal of Chemical Physics*, 132(21):214307, 2010.

[180] H. Y. Gao, D. Zhong, H. Mönig, H. Wagner, P. A. Held, A. Timmer, A. Studer, and H. Fuchs. Photochemical glaser coupling at metal surfaces. *J. Phys. Chem. C*, 118:6272–6277, 2014.

[181] D. Pacilé, P. Leicht, M. Papagno, M. P. Sheverdyaeva, P. Moras, C. Carbone, K. Krausert, L. Zielke, M. Fonin, Y. S. Dedkov, F. Mittendorfer, J. Doppler, A. Garhofer, and J. Redinger. Electronic and magnetic properties of quasi-freestanding graphene on Ni. *Phys. Rev. B*, 87:035420, 2013.

[182] S. Vijayaraghavan, W. Écija, D. Auwärter, S. Joshi, K. Seufert, A. P. Seitsonen, K. Tashiro, and J. V. Barth. Selective supramolecular Fullerene - Porphyrin interactions and switching in surface-confined $C_{60}Ce(TPP)_2$ dyads. *Nano Lett.*, 12:40774083, 2012.

Acknowledgements

In queste pagine colgo l'occasione per ringraziare tutte le persone che mi sono state professionalmente e moralmente vicine nel raggiungimento di questo traguardo.
Desidero ringraziare la dott.ssa Stefania Pagliara per avermi dato l'opportunità di portare avanti un progetto estremamente stimolante e per avermi affiancata nel raggiungimento di importanti obiettivi durante questi 3 anni.

Vorrei ringraziare, inoltre, tutti i gruppi di ricerca con i quali ho avuto la fortuna di collaborare e da ciascuno dei quali ho ricevuto un significativo contributo nello sviluppo del mio progetto di dottorato; un profondo riconoscimento al dott. Mario Italo Trioni e al suo gruppo di ricerca, in particolare alla dott.ssa Simona Achilli, per il fondamentale supporto teorico al progetto e per la costante disponibilità al confronto.
Un sentito riconoscimento al prof. Carlo Mariani e al suo gruppo di ricerca, in particolar modo al dott. Luca Longetti con il quale é stato un piacere lavorare fianco a fianco per qualche mese.
Un ringraziamento alla prof.ssa Petra Rudolf e al dott. Luca Bignardi per la preziosa collaborazione: Luca, grazie per il "Bignardissimo" lo conservo gelosamente.
Ringrazio inoltre la dott.ssa Cinzia Cepek e il suo gruppo per averci fornito il campione di grafene cresciuto su nichel e il prof. Fulvio Parmigiani per l'attento contributo nella realizzazione del lavoro riguardante l'interfaccia grafene/rame.
Grazie, inoltre, al prof. Mauro Sambi e al dott. Francesco Sedona per la grande disponibilità e per l'indispensabile supporto chimico fornitoci.
Un sentito riconoscimento a tutti i membri della commissione di esame e in particolare al dott. Silvano Lizzit per l'attenta lettura del manoscritto e per i suggerimenti che mi ha fornito.

Un affettuoso ringraziamento a tutti coloro che ho avuto la fortuna di incontrare durante questo percorso e con i quali ho condiviso la quotidianità di questi 3 anni. Fede, Chiara, Stefano sarebbe limitante descrivere in poche pa-

role quanto affrontato e condiviso in questi anni. Vi sono realmente grata per il vostro appoggio incondizionato, per la vostra presenza costante, per aver reso indimenticabili anche le giornate più nere. Stefano, grazie per essere stato il mio maestro di "scartinate", grazie per il tuo repertorio musicale, grazie per condividere i miei atteggiamenti schizofrenici...solo tu puoi capire cosa significhi rimanere inchiodati a fissare il semaforo verde!! Grazie piccola-Accademia della Crusca-Rucolina...é stato un piacere iniziare questo cammino insieme a te! Grazie per averci sempre incoraggiato e per essere riuscita ad aprirti con noi mettendo un po' da parte la tua natura forastica... Grazie Chiara per le tante risate insieme. La tua ironia ed esuberanza tante volte sovrastano la persona sensibile che sei e che ho avuto la fortuna di scoprire in tantissime occasioni. Grazie di cuore, siete il mio trittico (...) preferito.
Grazie a tutti i ragazzi dei laboratori. Grazie Giovanni. Se inizialmente la tua sagacia quasi mi intimoriva, ben presto ti sei rivelato una persona estremamente generosa e affabile. Grazie Emanuele per la tua disponibilità e pazienza e grazie Alessio, il mio primo "bang" é sempre per te.
Grazie ai miei compagni di studio e soprattutto grazie Nicola per aver sopportato le mie paturnie negli ultimi 10 anni e per la tua proverbiale saggezza: "Patí e mai mörer!"

Un ringraziamento a tutti gli amici e conoscenti che in qualche modo hanno condiviso con me questi anni. Grazie di cuore alle mie amiche Anna, Alessandra e Mariella per avere sempre voglia di consigliarmi e consolarmi. Grazie della vostra amicizia sincera e incondizionata.
Grazie Mery e Marco per l'aiuto grafico.
Grazie Alty per essere stata una presenza costante. Sei una preziosa confidente ed amica.
Grazie Debbie per essere mia strenua sostenitrice e per incoraggiarmi sempre.
Grazie ad Angoscia&Disperazione: Sarah grazie per essere da sempre l'AMICA che sei, Alessandra grazie per tentare di contenere le mie ansie.

Grazie a Massy e Ilaria per essere motivo di ispirazione come ricercatori cosí come nella vita.
Un ringraziamento speciale a Milly, mamma, nonna, maestra e donna dall'incredi-

bile forza d'animo. Grazie per aver sopportato malumori e ansie di ogni genere, per incoraggiarmi a superare le mie insicurezze e per non nascondere mai quanto tu sia orgogliosa di me.
Grazie a chi non c'é più, grazie dei preziosissimi doni che mi hai lasciato: forza di volontà, coerenza, impegno e dedizione al lavoro.

Infine grazie Ale. Avrei pagine da riempire con i motivi per i quali ti sono grata, ma si sa che noi non siamo tipi da troppe parole. Sono grata alla vita per averti messo sulla mia strada al momento giusto e sono grata a noi perché, non senza sforzo, abbiamo deciso di continuare a camminare insieme. Grazie per esserci. Sempre.

Physics isn't the most important thing. Love is.
Richard Feynman

List of publications

- S. Tognolini, S. Pagliara, L. Bignardi, S. Ponzoni, P. Rudolf, F. Parmigiani. **Surface states resonances at the single-layer graphene/Cu (111) interface**.
  Surface Science **643**, 210-213 (2016).

- S. Pagliara, S. Tognolini, L. Bignardi, G. Galimberti, S. Achilli, M. I. Trioni, W. F. van Dorp, V. Ocelík, P. Rudolf and F. Parmigiani. **Nature of the surface states at the single-layer graphene/Cu (111) and graphene/polycrystalline-Cu interfaces**.
  Physical Review B **91**, 195440 (2015).

- S. Tognolini, S. Achilli, L. Longetti, E. Fava, C. Mariani, M. I. Trioni, S. Pagliara. **Rashba Spin-Orbit Coupling in Image Potential States**.
  Physical Review Letters **115**, 046801 (2015).

- S. Tognolini, S. Ponzoni, F. Sedona, M. Sambi, S. Pagliara. **Role of the Substrate Orientation in the Photoinduced Electron Dynamics at the Porphyrin/Ag Interface**.
  The journal of Physical Chemistry Letters **6**, 3632-3638 (2015).

- F. Rigoni, S. Tognolini, P. Borghetti, G. Drera, S. Pagliara, A. Goldoni, L. Sangaletti. **Environmental Monitoring of Low-ppb Ammonia Concentrations Based on Single-wall Carbon Nanotube Chemiresistor Gas Sensors: Detection Limits, Response Dynamics, and Moisture Effects**.
  Procedia Engineering **87**, 716-719 (2014).

- F. Rigoni, S. Tognolini, P. Borghetti, G. Drera, S. Pagliara, A. Goldoni, L. Sangaletti. **Enhancing the sensitivity of chemiresistor gas sensors based on pristine carbon nanotubes to detect low-ppb ammonia concentrations in the environment**.
  Analyst **138**, 7392-7399 (2013).